การแพร่ของแกลเลียมในฟิล์มบางชั้นคู่คอปเปอร์อินเดียมไดซีลีไนด์/คอปเปอร์แกลเลียมไดซีลีไนด์

นางสาวบุญลักษณ์ นามนวน

วิทยานิพนธ์นี้เป็นส่วนหนึ่งของการศึกษาตามหลักสูตรปริญญาวิทยาศาสตรมหาบัณฑิต
สาขาวิชาฟิสิกส์ ภาควิชาฟิสิกส์
คณะวิทยาศาสตร์ จุฬาลงกรณ์มหาวิทยาลัย
ปีการศึกษา 2555

DIFFUSION OF GALLIUM IN $CuInSe_2$/$CuGaSe_2$ BILAYER THIN FILMS

Miss Boonyaluk Namnuan

A Thesis Submitted in Partial Fulfillment of the Requirements
for the Degree of Master of Science Program in Physics
Department of Physics
Faculty of Science
Chulalongkorn University
Academic Year 2012

Thesis Title	DIFFUSION OF GALLIUM IN $CuInSe_2/CuGaSe_2$ BILAYER THIN FILMS
By	Miss Boonyaluk Namnuan
Field of Study	Physics
Thesis Advisor	Assistant Professor Sojiphong Chatraphorn, Ph.D.

Accepted by the Faculty of Science, Chulalongkorn University in Partial Fulfillment of the Requirements for the Master's Degree

.....Dean of the Faculty of Science
(Professor Supot Hannongbua, Dr. rer. nat.)

THESIS COMMITTEE

.....Chairman
(Assistant Professor Somchai Kiatgamolchai, Ph.D.)

.....Thesis Advisor
(Assistant Professor Sojiphong Chatraphorn, Ph.D.)

.....Examiner
(Assistant Professor Tonphong Kaewkongka, Ph.D.)

.....External Examiner
(Sirapat Pratontep, Ph.D.)

บุญลักษณ์ นามนวน : การแพร่ของแกลเลียมในฟิล์มบางชั้นคู่คอปเปอร์อินเดียมไดซีลีไนด์/คอปเปอร์แกลเลียมไดซีลีไนด์. **(DIFFUSION OF GALLIUM IN $CuInSe_2$/$CuGaSe_2$ BILAYER THIN FILMS)** อ.ที่ปรึกษาวิทยานิพนธ์หลัก : ผศ.ดร.โสจิพงศ์ ฉัตราภรณ์, 104 หน้า.

ปัจจุบันฟิล์มบางคอปเปอร์อินเดียมแกลเลียมไดซีลีไนด์ (CIGS) ได้รับความสนใจในฐานะเป็นชั้นดูดกลืนแสงสำหรับอุปกรณ์โฟโตโวลตาอิก ช่องว่างแถบพลังงานของ CIGS จะมีค่าอยู่ในช่วงระหว่าง 1.02 ถึง 1.66 อิเล็กตรอนโวลต์ ซึ่งสามารถปรับค่าได้โดยการปรับปริมาณธาตุแกลเลียม (Ga) และค่าประสิทธิภาพของเซลล์สุริยะชนิดฟิล์มบาง CIGS ที่ได้ 20% นั้นก็มาจากการปรับสัดส่วนของธาตุ Ga ให้เหมาะสมตามความลึกของฟิล์ม ความเข้าใจต่อการแพร่ของธาตุแกลเลียมจึงเป็นสิ่งสำคัญสำหรับการพัฒนาและเพิ่มค่าประสิทธิภาพของเซลล์สุริยะชนิดฟิล์มบาง CIGS โครงสร้างฟิล์มบางชั้นคู่ของคอปเปอร์อินเดียมไดซีลีไนด์/คอปเปอร์แกลเลียมไดซีลีไนด์ (CIS/CGS) ถูกผลิตบนแผ่นรองรับกระจกโซดาไลม์ (SLG) ที่มีชั้นของโมลิบดีนัมเคลือบอยู่ (Mo/SLG) โดยเทคนิคการเตรียมฟิล์มแบบลำโมเลกุล สัดส่วนของการปลูกฟิล์มบางชั้นคู่จะมีทั้งแบบสัดส่วนคอปเปอร์มากและคอปเปอร์น้อยในแต่ละชั้นของฟิล์มบางชั้นคู่ที่อุณหภูมิการปลูกของแผ่นรองรับ 600 องศาเซลเซียส ผลการวัดจากการเลี้ยวเบนรังสีเอกซ์แสดงให้เห็นว่าปริมาณการแพร่ของธาตุ Gaในระดับที่สูงจะพบได้จากฟิล์มบางชั้นคู่ CIS/CGS ที่เป็นคอปเปอร์ส่วนมากมากกว่าที่จะเป็นฟิล์มบางชั้นคู่แบบอื่น การแพร่ของธาตุ Ga ดูเหมือนว่าจะถูกสนับสนุนโดยเฟสของคอปเปอร์ซีลีไนด์ส่วนเกินที่ขึ้นอยู่กับอุณหภูมิของแผ่นรองรับ ธาตุโซเดียม (Na) จากกระจก SLG คืออีกหนึ่งปัจจัยสำคัญที่ส่งผลต่อการแพร่ของธาตุ Ga จากผลการทดลองของการใช้ชั้นอะลูมินา (Al_2O_3) เคลือบลงบน SLG เพื่อขัดขวางการแพร่ของธาตุ Na จากกระจก SLG แสดงให้เห็นว่ารูปแบบอัลลอยของสารประกอบ CIGSได้ก่อตัวมากกว่าฟิล์มบางชั้นคู่ที่มีธาตุโซเดียมประกอบอยู่ ธาตุแกลเลียมสามารถแพร่ผ่านได้ทั้งที่ที่เป็นตำแหน่งของธาตุคอปเปอร์ และตำแหน่งกลุ่มของธาตุหมู่สาม ซึ่งธาตุ Na สามารถที่จะครอบครองตำแหน่งเหล่านี้ จึงทำให้ขัดขวางการแพร่ของธาตุ Ga นอกจากการใช้แผ่นรองรับ SLG แล้ว ยังมีการปลูกฟิล์มบางชั้นคู่ลงบนแผ่นรองรับ GaAs(001) เพื่อสังเกตการแพร่ของธาตุ Ga ภายใต้การจำกัดทิศทางของโครงสร้างผลึก การแพร่ของธาตุ Ga จะเกิดได้ยากสำหรับฟิล์มบางชั้นคู่ที่เป็นคอปเปอร์ส่วนมาก ที่ซึ่งความบกพร่องทางผลึกเพื่อการแพร่ของ Ga จะเกิดขึ้นได้ยากในโครงสร้างผลึกที่มีคุณภาพสูงของโครงสร้างฟิล์มบางชั้นคู่ผลึกเดี่ยวที่เป็นคอปเปอร์มาก

ภาควิชา ฟิสิกส์ ลายมือชื่อนิสิต .....

สาขาวิชา ฟิสิกส์ ลายมือชื่อ อ.ที่ปรึกษาวิทยานิพนธ์หลัก .....

ปีการศึกษา 2555

5372274123 : MAJOR PHYSICS
KEYWORDS : DIFFUSION/ $CuInSe_2$/ $CuGaSe_2$/ BILAYER/ SOLAR CELLS

BOONYALUK NAMNUAN : DIFFUSION OF GALLIUM IN $CuInSe_2$/$CuGaSe_2$ BILAYER THIN FILMS. ADVISOR : ASST. PROF. SOJIPHONG CHATRAPHORN, Ph.D., 104 pp.

At present, $CuIn_{1-x}Ga_xSe_2$ (CIGS) thin films are one of key materials for an absorber layer for photovoltaic devices. The energy gap of CIGS is in the range between 1.02 to 1.66 eV which can be adjusted by the Ga composition. The conversion efficiency of 20% for the CIGS thin film solar cells has been achieved which is due to the appropriate Ga content and the profile of Ga distribution in the film. An understanding of the diffusion of Ga is necessary to develop and increase the performance of the CIGS thin film solar cells. The investigation of Ga diffusion is proposed through the studies of bilayer structures, CIS/CGS and CGS/CIS, fabricated on molybdenum-coated soda-lime glass (Mo/SLG) by Molecular Beam Deposition (MBD) technique. The compositions of the bilayers are varied for both Cu-rich and Cu-poor in each layer with the substrate temperature at 600°C. The XRD results show that higher Ga diffusion is observed in the Cu-rich CIS/CGS bilayer rather than other bilayers. The diffusion of Ga seems to be enhanced by the excess Cu-Se phase that is dependent upon the substrate temperature. The Na from the SLG is one of the important factors affecting the Ga diffusion. The aluminum oxide (Al_2O_3) thin film is used to block Na from the SLG. The results show the alloying CIGS patterns rather than separated CIS and CGS patterns as for the bilayers with Na. Ga can diffuse through either Cu or group-III sites where Na may seize these sites and obstruct the diffusion of Ga. Apart from the SLG substrate, GaAs(001) is used for the growth of bilayers to observe the diffusion of Ga under the constrains of crystal orientation. The diffusion of Ga is more difficult in Cu-rich bilayers. The defects for enhancing Ga diffusion hardly occur in the high crystallinity of Cu-rich epitaxial bilayers.

Department : Physics Student's Signature .....
Field of Study : Physics Advisor's Signature .....
Academic Year : 2012

Acknowledgments

I would greatly appreciate my thesis adviser, Assistant Professor Dr. Sojiphong Chatraphorn for his superintendence, kindness suggestion, scientific skills and invaluable discussion. This thesis would not have been possible unless he gave me an opportunity to work on this research and helped me got through all steps to complete this thesis. I am also grateful to Assistant Professor Dr. Kajornyod Yoodee for any valuable suggestions and unforeseen opinions.

I would be thankful for the chairman and the committee members, Assistant Professor Dr. Somchai Kiatgamolchai, Assistant Professor Dr. Tonphong Kaewkongka and Dr. Sirapat Pratontep for their valuable times to read and comment on this thesis.

I am indebted to Dr. Bancha Arthibenyakul who trains me for operating the Molecular Beam Epitaxy system, gave valuable suggestions and shared his experiences on this research even if he had not been involved throughout my thesis. I am also indebted to Dr. Rachasak Sakdanupab who gave many advices and suggestions in my work.

I would like to thank my colleagues in the SPRL group whose names are not mentioned here for their friendliness, encouragement, generosities and their moral supports would give me a good grown-up.

I would like to acknowledge Mrs. Jiraprapa Neampan, the staff of the Department of Geology, Chulalongkorn University for helping with the X-Ray diffractometer. This work is successful with her kindness. In addition, I would also like to thank Mr. Pornsak Panchawirat for his helps with the SEM and EDS.

I would like to acknowledge the financial support from Science Achievement Scholarship of Thailand and also Thailand Center of Excellence in Physics (ThEP Center) for the financial support during my master degree.

I would like to thank to my family for their loves and understanding that have given me an optimistic and a stronger person.

Contents

Page

Page

Page

List of Tables

Page

List of Figures

Page

Page

Page

Page

Chapter I

Introduction

1.1 Overview

The incessant demand for energy and depleting oil resource, alternate energy sources are actively sought from suitable resources and it should be clean as well. At present, the use of the fossil fuels results in air pollutants, namely CO, NO_x, and SO_x, and related health risks including global warming due to the increased green-house gas concentration. These issues raise serious concerns on the sustenance of life on earth. Just the rise of 1°C in global temperature would melt a significant portion of the polar ice thereby removing large area from lower lying lands by the seas and oceans, not except for Bangkok area in Thailand when the global temperature increases to 2°C [1]. Therefore, a step forward in the pursuit of alternative energy resources in the harmless energy from carbon-free sources, such as wind, thermal, hydroelectricity, tidal, and solar energy is necessary. Especially, the solar energy is quite appropriate for Thailand because it is located around Equatorial Meridian, so that it receives the sunlight throughout the year. Nowadays, silicon (Si) wafers are the most popular for the production of integrated chips and in the solar cell industries because of theirs high performance of energy conversion. However, Si that used in solar cells must be highly purified about 99.9999%, therefore, its cost has increased. How can we reduce the fabrication cost of Si solar cells? It is probably impossible and the chip industries have high demands on Si. Hence, the developments of solar cells in other types such as polycrystalline Si, III-V group single crystal with multi-junction, thin films, and dye-sensitized solar cells are promising candidates and alternative to single-crystalline Si. The evolution of world record of energy conversion efficiencies and types of solar cells is illustrated in Fig. 1.1. For thin film devices, it seems that chalcogenide based thin film solar cells are the most interesting, especially copper indium gallium diselenides ($CuIn_{1-x}Ga_xSe_2$) or CIGS thin film solar cells, because it has been developed to 20.3% by ZSW when compared with others in the same group [3]. The performances of different chalcogenide solar cells are shown in Table 1.1.

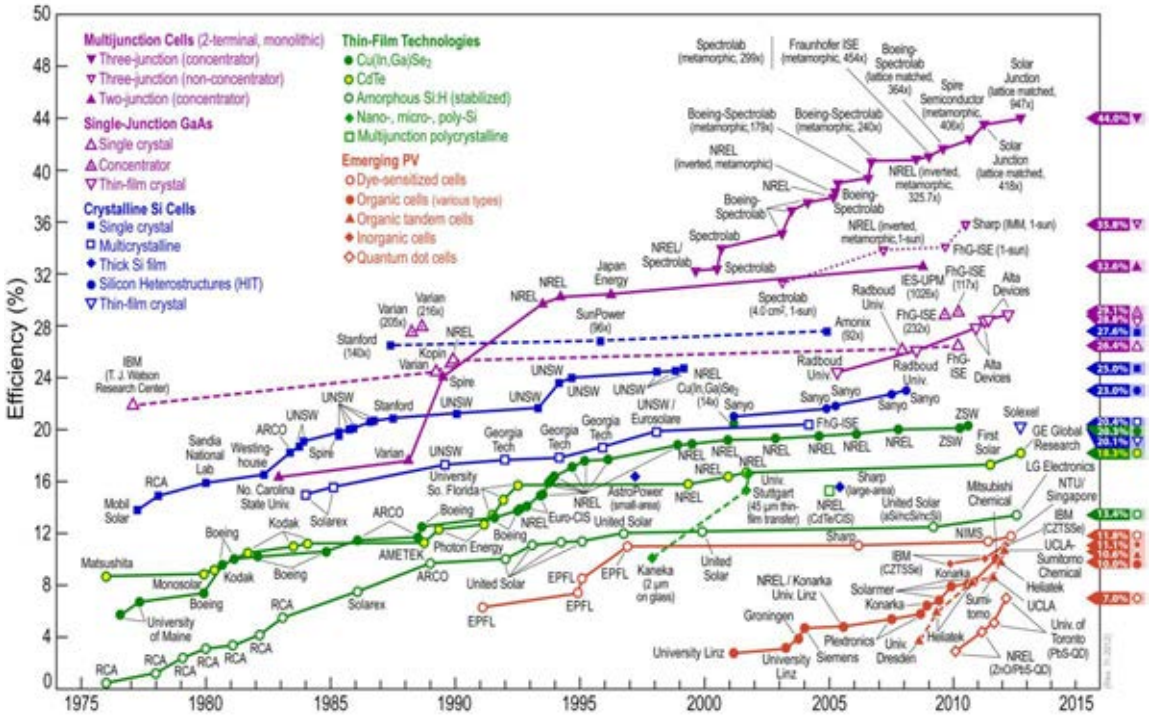

Figure 1.1: The evolution world records of conversion efficiencies for various types of solar cells 1975-2012 [2].

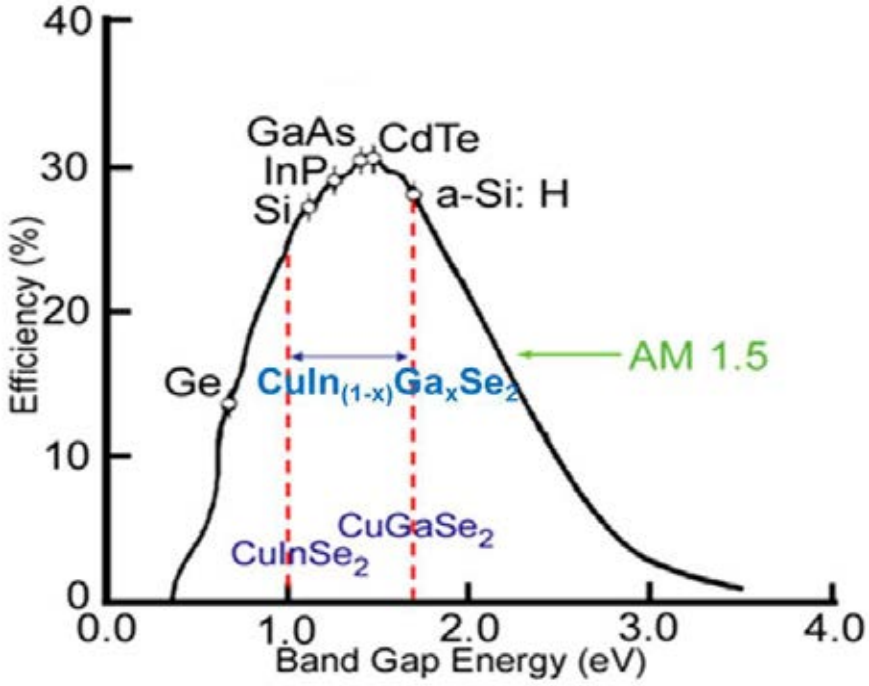

Figure 1.2: Theoretical efficiency for various types of solar cells as a function of band gap energy at AM 1.5 [7].

Table 1.1: State of the art performance of chalcogenide solar cells [4].

Element compounds	Description	Efficiency (%)
II-VI_2	*CdTe*	17.2
I-III-VI_2	*$CuInSe_2$*	16.0
	$CuGaSe_2$	10.2
	$Cu(In,Ga)Se_2$	20.3
	$Cu(In,Ga)(S,Se)_2$	17.2*
	$CuInS_2$	11.1
	$Cu(In,Ga)S_2$	12.0
	$Cu(In,Al)Se_2$	16.9
	$Ag(In,Ga)Se_2$	9.3
I-II-IV-VI_2	*$Cu_2(Zn,Sn)(S,Se)_2$*	9.6

** 30cm×30cm submodule*

$Cu(In_{1-x}Ga_x)Se_2$ is used as a photon absorber layer for thin film solar cell applications. Its band gap energy can be adjusted between 1.02 to 1.66 eV by varying the ratio of group-III elements or x = [Ga]/([Ga]+[In]) ratio. In fact, $CuInSe_2$ (CIS) and $CuGaSe_2$ (CGS), including its alloys have high absorption coefficient among other semiconductors used in photovoltaic devices. However, CIS without Ga (x = 0) has a band gap energy of only 1.02 eV which results in a lower open-circuit voltage (V_{oc}). On the contrary, an excessive Ga content can cause the lower performance as well, typically a low short-circuit current density (J_{sc}) due to the lack of absorption in the long wavelength of the solar spectrum [5, 6]. So, the amount of Ga as well as In are one of the important factors to increase the band gap energy and achieve higher performance of the devices. Fig. 1.2 illustrates the efficiencies of the solar materials as a function of band gap energy and shows the range of band gap energy of CIGS by adjusting the Ga content [7].

At present, the performance of CIGS thin film solar cells can also be enhanced by Ga-grading technique. To improve and understand this technique, the studying of the diffusion of Ga are therefore carried out in this work by focusing on the causes of Ga diffusion mechanisms via the factors for diffusion such as growth substrate temperature, Cu atomic composition or y = [Cu]/([Ga]+[In]), etc.

1.2 Literature Review of Models for Ga Diffusion

Dating back to around 1970, the CIS single crystalline thin film solar cells were fabricated by Bell laboratory scientists; they achieved 12% conversion efficiency [8]. By this result, the development of CIS thin film has started. In the early 1980, the addition of Ga to CIS could increase the solar cell performance. The addition of Ga resulted in an improvement of an open-circuit voltage (V_{oc}) and a fill factor (FF) corresponding to higher band gap energy. Afterwards, the development of alloying CIGS has never been stopped. Today, an optimum Ga content in CIGS appears at x ~ 0.3 [9, 10]. However, the homogeneous Ga depth profiles cannot achieve higher performance. Therefore, the variation of the x = [Ga]/([Ga]+[In]) or band gap depth profiles causing the Ga-gradient improves the efficiency, including the thickness of CIGS could be reduced, e.g. the thickness of CIGS 1.8 μm results in the performance of 16.1%, 1.0 μm for 15% and 0.6 μm for 12.1% [11]. Band gap profiling is classified in two categories, (i) normal grading and (ii) double grading. The first one is an increase of the band gap towards the back contact, while the latter is an increase band gap both towards the back and front contacts [12]. Ga-gradient towards the back contact acts as a back surface field which the carrier recombination probability can be reduced in the regions with higher band gap energy, so the short-circuit current density (J_{sc}) is increased. For the double grading, it improves both V_{oc} and J_{sc} owing to the varying of band gap profiles and decreasing of recombination at the buffer/CIGS interface, respectively. By this advantage of Ga-gradient, it continues to be a major focus of activity in CIGS thin films solar cells, the studying of diffusion of group-III elements is thus necessary.

There are many studies about the investigation of the diffusion of Ga and In elements. The inter-diffusion of these atoms was observed via the bilayer structure of $CuGaSe_2$ (CGS) and $CuInSe_2$ (CIS) for considering the alloying formation of CIGS structure. For the group-III elements diffusion from bilayer, the work begun by Walter and Schock in 1993 that inter-diffusion of Ga and In were arising out of the presence of the copper selenide secondary phase ($Cu_{2-x}Se$) that usually took place in Cu-rich composition (y > 1). It is believed that $Cu_{2-x}Se$ acts as a quasi-liquid phase and enhances the diffusion of elements in the crystal structure [13]. Afterwards, the role of $Cu_{2-x}Se$ secondary phase in Cu-rich CIS epitaxial films has been investigated in the

manner of the film quality and strain relaxation between CIS films and GaAs substrate from the lattice mismatch resulting in the surface undulation [14, 15, 16]. In 2000, by annealing the post-growth of Cu-rich CIS epitaxial film on GaAs(001) substrate with annealing temperature greater than 500°C, Uchino and his colleagues did not find the $Cu_{2-x}Se$ secondary phase, but they found the inter-diffusion between the CIS and single crystalline substrate. It did not occur in the as-grown film. From their observation, the inter-diffusion of Cu, In and Ga atoms can be activated by the $Cu_{2-x}Se$ phase [17]. However, the experimental evidence about the $Cu_{2-x}Se$ secondary phase to date is not sufficient to explain its actual role. Other models for inter-diffusion of Ga and In, back in 1996, Schroeder and Rockett proposed that it did not depend on the existence of $Cu_{2-x}Se$ phase. In theirs studies of the diffusion of Ga in CIS epitaxial layer, the Ga diffusion was closely related with Cu-atomic composition in such a way that Ga diffusion is less in near stoichiometric CIS films (y = 1), but higher in both Cu-rich and Cu-poor films. It was suggested that the diffusion of Ga could proceed via vacant lattice sites. The difference of Cu-atomic composition between Cu-rich and Cu-poor films leads to the different types of vacancy point defects such as Cu vacancies and group-III vacancies in Cu-poor and Cu-rich composition, respectively. Hence, Ga atoms are able to diffuse by a vacancy mechanism through either Cu or In vacancies. Moreover, they also discovered that the higher concentration of Ga diffusion was found in Cu-rich composition, they proposed that In vacancies were more favorable for Ga than Cu vacancies in Cu-poor films [18]. In 2003, Lundberg *et al.* substantiated that the diffusion of Ga and In in polycrystalline CIS and CGS bilayer structure proceeded via vacant lattice sites that Ga and In could diffuse through either Cu sites and group-III sites. Moreover, copper selenide phase has a little role for group-III elements diffusion, but the higher diffusion was found in Na free films [19, 20].

Normally, the highest performance of CIGS solar cells can be obtained from a soda-lime glass (SLG) substrate, because it is a natural Na reservoir that Na can out-diffuse into the CIGS absorber layer and hinder the donor type defects of In_{Cu} so that it enhances the quality of CIGS film, including the acceptor type defects of Cu vacancies. The effect of Na on the elemental diffusion in CIS films was studied by Wei *et al.* around 1998 via the theoretical defect calculation. From their results, they

found that the major effect of Na was the obstruction of the stability of "ordered defect compounds" (ODC) or $2V_{Cu}+ In_{Cu}$. Na atoms always reside in Cu sites (Na_{Cu}) and In sites (Na_{In}) [21]. In that manner, Na could be considered that it seized the vacant lattice site which was more difficult for Ga and In for the inter-diffusion.

1.3 Motivation and Scope of This Thesis

The motivation of this thesis was originated from the previous studying of the crystalline growth of CIS epitaxial thin films on GaAs(001) substrate using the two-stage process. The X-ray diffraction (XRD) result shown in Fig. 1.3 in a blue curve is the Cu-rich CIS film that is converted from y ~ 1.6 to 1.3 showing that Ga can diffuse from the GaAs substrate and form the CGS interface layer with the excess $Cu_{2-x}Se$ secondary phase. The second one shown in a red curve is the Cu-poor CIS film also grown by the two-stage method that the Cu-rich composition (y ~ 1.6) was formed in the first stage and then converted to the Cu-poor composition (y ~ 0.9). From this result, they did not find CGS peak left and proposed that Ga diffused into the CIS film and might form the alloying CIGS film. Thus the work of thesis then involves the factors that affect the Ga diffusion in bilayer structures CIS/CGS and vice versa. The result should be useful for applying to Ga-grading in CIGS absorber layer in thin film solar cells that requires the basic knowledge of group-III diffusion mechanisms for improving the performance of the solar cells.

This thesis concentrates on the key factors of Ga diffusion from the bilayer structure of CIS/CGS and vice versa fabricated by Molecular Beam Deposition (MBD) technique with the total thickness of approximately 1 μm. In order to investigate the effect of Na on Ga diffusion, aluminum oxide (Al_2O_3) thin film is used as a Na blocking to prohibit the out-diffusion of Na from the SLG. With the different types of substrate between non Na blocking and also Na blocking, they are compared with each other. Apart from the SLG substrates, epitaxial bilayer thin films of CIS/CGS and CGS/CIS on GaAs(001) substrate are compared with the polycrystalline counterparts obtained from the SLG substrates. The diffusion of Ga are mainly investigated from the XRD patterns to observe the shift of CIS and CGS peaks obtained from the bilayer films compared with the peak positions of CIS and CGS films. Cross-sectional images and compositional depth profiles are investigated by the

scanning electron microscope (SEM) with energy dispersive X-ray spectroscopy (EDS).

1.4 Objective of The Research

The objectives of this research are:

- To fabricate the bilayer structures CIS/CGS and CGS/CIS thin films on soda-lime glass (SLG) and GaAs(001) substrates using Molecular Beam techniques.
- To study the mechanisms and key factors affecting the diffusion of Ga and In under various growth conditions.

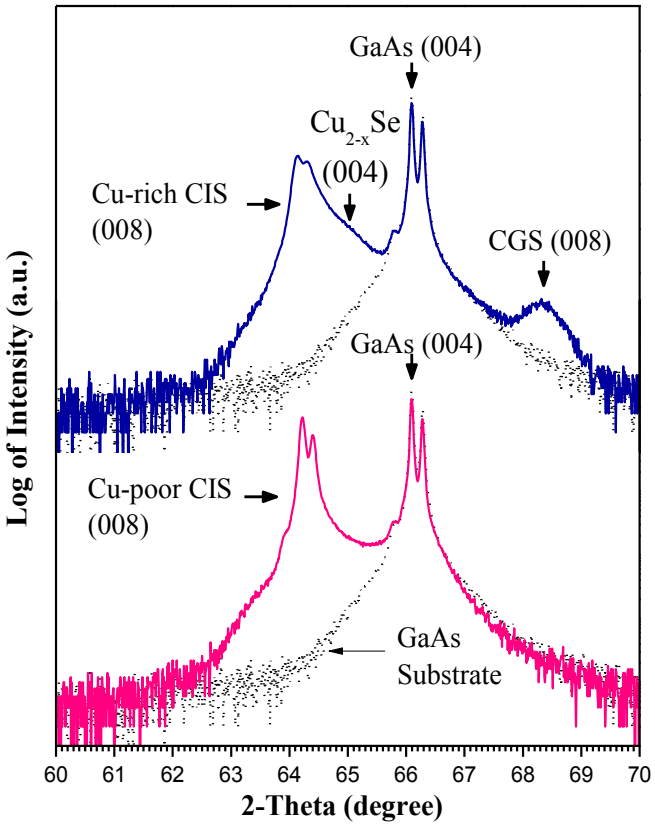

Figure 1.3: XRD patterns of (a) Cu-rich CIS epitaxial films (y ~ 1.6 → 1.3) and (b) Cu-poor CIS epitaxial films (y ~ 1.6 → 0.9) [22].

1.5 Thesis Organization

This thesis is divided into six chapters. Chapter I covers the introduction of this research such as literature reviews on Ga diffusion models, motivation and scope of this thesis. Then chapter II describes the basic of CIGS materials, crystalline defects, diffusion mechanisms, the structural properties of CIGS, including the molecular beam deposition techniques. In chapter III, the experimental details of the fabrication of polycrystalline and single crystalline CIS, CGS and CIGS are presented. The calibration of molecular constituents for the depositions of bilayer thin films is mentioned in details, and also the characterizations of the samples are briefly presented in their basic principles. In chapter IV, the experimental results of varying substrate temperatures with different Cu-atomic compositions on Ga diffusion in the polycrystalline bilayers are described and discussed for their crystallographic structure and morphology, respectively. At last the results on the bilayers without Na from SLG are presented. Moreover, in chapter V, the effect of constraint on the crystalline orientation from GaAs(001) substrate is discussed and compared to the polycrystalline films. Finally, in chapter VI, all of the important results are summarized and the guidelines for the future research are given.

Chapter II

The Basic Principle of Elements Diffusion and CIGS Materials

This chapter describes the background knowledge for understanding the diffusion in bilayer CIS/CGS thin films. The crystalline defects in solid are primarily mentioned, and followed by the mechanism for the elements diffusion. Finally, the CIGS system is described, and also the details of molecular beam deposition technique used in this research are given.

2.1 Crystalline Defects in Thin Films

The different types of imperfections or defects in the ideal arrangement of atoms in crystal are briefly describes in this section. In reality, crystals are never be perfect and contain various types of imperfections that affect many of their physical properties which in turn affect the diffusion mechanism of the elements in materials. Crystal lattice imperfections are classified according to their geometry and shape. The three mains types are (1) zero-dimensional or point defects, (2) one-dimensional or line defects (dislocation), and (3) two-dimensional defects or area defects (grain boundaries) [23].

2.1.1 Point Defects

The simplest point defect is the vacancy, an atom site from which an atom is missing. Vacancies can occur during the growth of crystals, or they may be created by atomic rearrangements in an existing crystal due to atomic mobility. Vacancies can move by exchanging positions with their neighbors. This process is important in the migration or diffusion of atoms in solid, particularly at elevated temperatures where atomic mobility is greater, and also the number of vacancies which are related to their higher formation energy.

Moreover, an atom in a crystal can squeeze in an interstitial site between surrounding atoms in regular lattice site. If the interstitial atom is the same types as the lattice atoms, it is called *self-interstitial*, or *interstitialcy*. These do not generally occur naturally because the creation of a self-interstitial causes the structural distortion, and then it costs more energy to form as compared to the energy for creation of a vacancy. Unusually, smaller atoms such as carbon, nitrogen, oxygen, etc. can occupy interstitial sites which they are called *interstitial impurities*; they introduce less distortion to the lattice. If the atomic impurity replaces or substitutes in the lattice site, it is called *substitutional impurity*. All the point defects are schematically shown in Fig. 2.1.

In ionic crystals point defects are more complex due to the necessity to maintain electrical neutrality. When two oppositely charged ions are missing from an ionic crystal, a cation-anion divacancy is created that is known as a *Schottky imperfection*. If a positive cation moves into an interstitial site in an ionic crystal, a cation vacancy is created in the normal ion site. This vacancy-interstitialcy pair is called a *Frenkel imperfection*, both types of imperfection are illustrated in Fig. 2.2. The presence of these defects in ionic crystals increases their electrical conductivity.

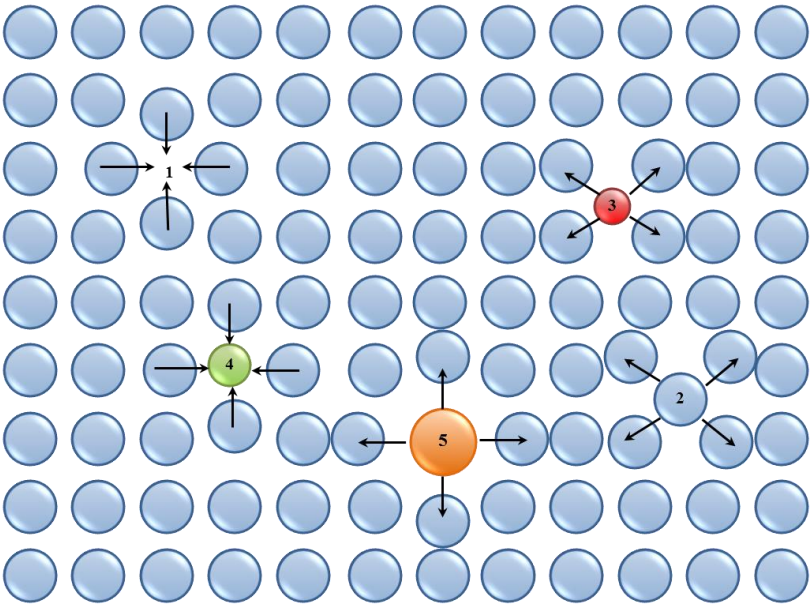

Figure 2.1: Schematic of different point defects in a crystal. (1) vacancy; (2) self-interstitial; (3) interstitial-impurity; (4) and (5) substitutional impurities. The arrows show the local stresses induced by the point defects.

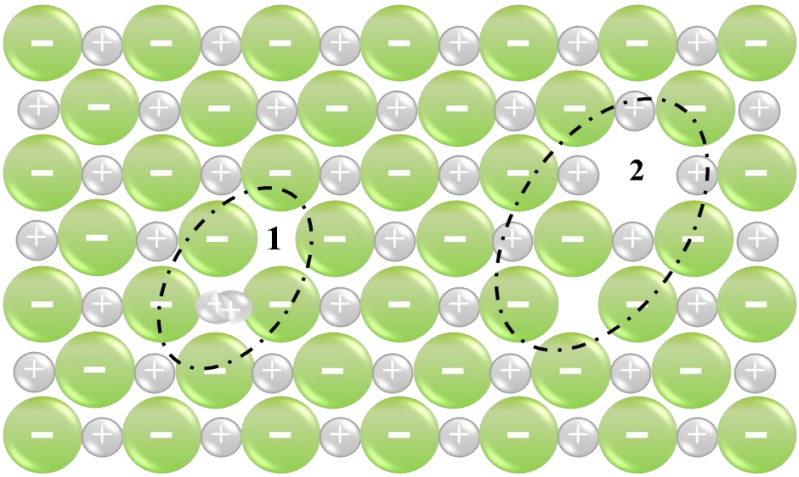

Figure 2.2: Schematic of (1) Frenkel defect (vacancy-interstitial pair) and (2) Schottky defect (cation and anion vacancies pair) in an ionic crystal.

2.1.2 Line Defects (Dislocation)

Dislocations in crystalline solids are defects that cause lattice distortion centered around a line. They are formed by the permanent deformation of crystal, vacancy condensation, including lattice mismatch between film formation and substrate that induced the misfit dislocation beyond the critical thickness in epitaxial thin films [24]. The two main types of dislocations are the *edge* and *screw types*. A combination of the two leads to mixed dislocation. An edge dislocation is created in a crystal by the insertion of an extra half plane of atoms, as shown in Fig. 2.3(a) and the symbol ⊥ that indicates a positive dislocation. The displacement distance of the atoms around the dislocation is called the *slip* or *Burgers vector* **b** and is *perpendicular* to the edge-dislocation line, as shown in Fig. 2.3(b). The edge dislocation has a region of compressive strain and a region of tensile strain around the half plane of atoms. The screw dislocation can be formed by applying upward and downward shear stresses to regions of crystal separated by a cutting plane, as shown in Fig. 2.4(a). These shear stresses induce a region of distorted crystal lattice. The slip or Burgers vector of the screw dislocation is *parallel* to the dislocation line, as shown in Fig. 2.4(b).

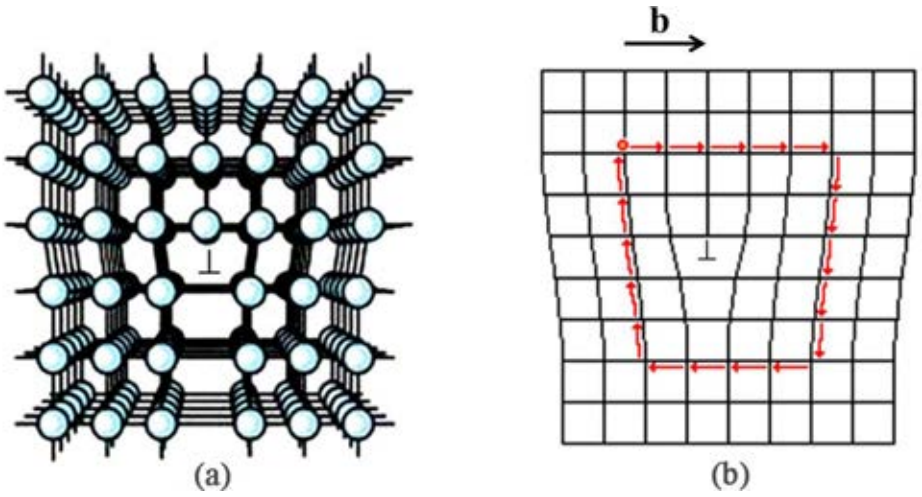

Figure 2.3: (a) Positive edge dislocation, a linear defect occurs in the region just above the inverted "tee" and (b) Edge dislocation that indicates the orientation of its Burgers or slip vector ***b*** *perpendicular to the dislocation line [23].*

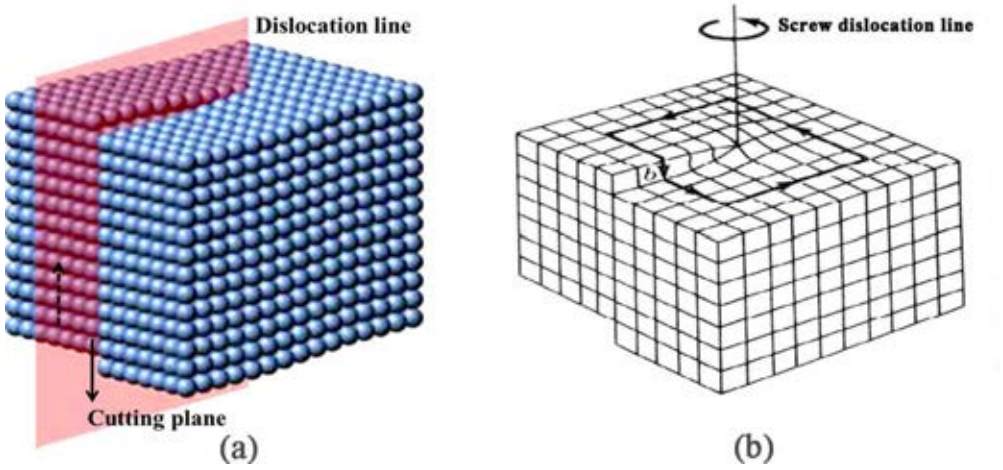

Figure 2.4: (a) A perfect crystal is sliced by a cutting plane, and up and down shear stresses are applied parallel to the cutting plane and (b) A screw dislocation with its slip or Burgers vector ***b*** *parallel to the dislocation line [23].*

2.1.3 Planar Defects

Generally, solids consist of a number of small crystallites or grains, except for the single crystalline solid. The grains can be from nanometers to millimeters in size and orientations of atomic planes are different with respect to the neighboring grains. These solids are *polycrystalline* materials that the individual grains are separated by *grain boundaries* (surface imperfections). Grain boundaries have some atoms in

strained positions that raise the energy of the grain-boundary region, so the higher energy can be introduced in more open crystalline structure that facilitates the nucleation growth. The lower atomic packing of the grain boundaries also allows for a more rapid diffusion of atoms in the grain boundaries region.

2.2 Fundamental Concept of Elements Diffusion

2.2.1 The Probability of Vacancy Defect

In solid states, many reactions can occur involving the spontaneous rearrangement of atoms into new and more stable atomic arrangements. In order for this reaction to proceed from the unreacted to the reacted state, the reacting atoms must have sufficient energy to overcome an activation energy barrier. The additional energy required above the average energy of the atoms is called the *activation energy* (E^*) or *formation energy*. At any temperature, only a fraction of atoms in a system will have sufficient energy to reach the activation energy level of E^*. As the temperature of the system is increased, more and more atoms will attain the activation energy level. The probability (P) of finding an atom at an energy E^* greater than the average energy E of all atoms in a system at a particular temperature T (in Kelvin) is $P \propto e^{-E^*/kT}$, where k is Boltzmann's constant. The fraction of atoms in a system having energies greater than E^* can be written as:

$$\frac{n}{N_{total}} \cong e^{-E^*/kT}, \qquad (2.1)$$

where n is the number of atoms with an energy greater than E^*, N_{total} is total number of atoms present in system.

The number of vacancies at equilibrium at a particular temperature in a crystal lattice can be expressed by the following relationship, which is similar to Eq. 2.1:

$$\frac{n_v}{N_{total}} \cong e^{-E_v/kT}, \qquad (2.2)$$

where n_v is the number of vacancies, N is total number of atomic sites and E_v is activation energy to form a vacancy.

At the equilibrium concentration of vacancies present in a pure metal at 1000°C and the energy of formation of a vacancy is 1 eV, according to Eq. 2.2., there is approximately one vacancy for every 10^5 atoms.

2.2.2 Diffusion Mechanisms

In solids, diffusion can be defined as the mechanism by which an atom is transported from one place to another. Atomic movements are restricted due to bonding to equilibrium position. However, thermal vibrations occurring in solids do allow some atoms to move. Diffusion of elements in solids is particularly important since most solid-state reaction such as the precipitation of a secondary phase from solid solution and nucleation and growth of new grains in the recrystallization involve atomic movements.

There are three main mechanisms of diffusion of atoms in a crystalline lattice: (a) interchange by rotation about a midpoint (b) the interstitial and (c) the vacancy or substitutional, as shown in Fig. 2.5.

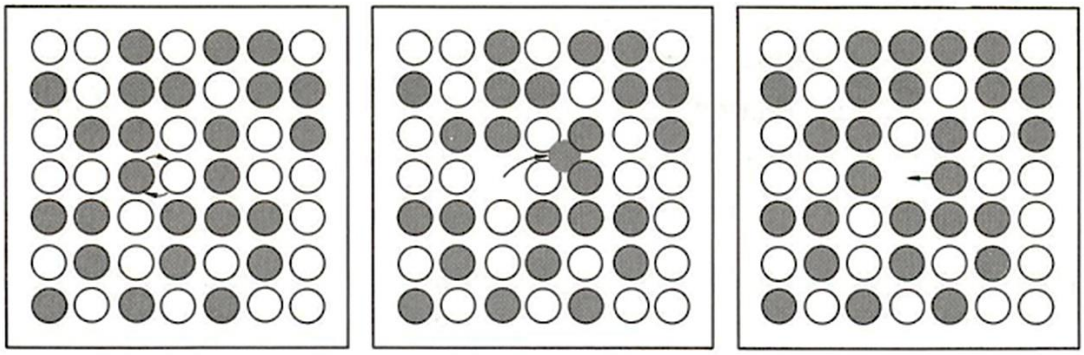

Figure 2.5: Three mechanisms of elements diffusion (a) interchange by rotation about a midpoint (b) migration though interstitial sites (c) atoms exchange position with vacant lattice sites [25].

2.2.2.1 Interstitial Diffusion

Atoms in crystal lattices can take place when atoms move from one interstitial site to another neighboring interstitial site without permanently displacing any of the atoms in the crystal lattice. The size of the diffusion atoms must be relatively small when compared to the surrounding atoms.

2.2.2.2 Vacancy or Substitutional Diffusion

Atoms can move in crystal lattices from one atomic site to another if there is enough activation energy provided by the thermal vibration of the atoms and if there are vacancies or other crystal defects in the lattice for atoms to move into. Some vacancies are always present to enable substitutional diffusion of atoms to take place. As the temperature of the system increases, more vacancies are present and more thermal energy is available, and so the diffusion rate is higher at higher temperatures. In order to perceive the vacancy diffusion mechanism, it can be illustrated at in Fig. 2.6. If an atom next to the vacancy has sufficient activation energy, atom can break the original bonds among atoms, so it can move to or replace the vacant site to create the new bond and thereby contribute to the self-diffusion of atoms in the lattice assisted by having vacancies.

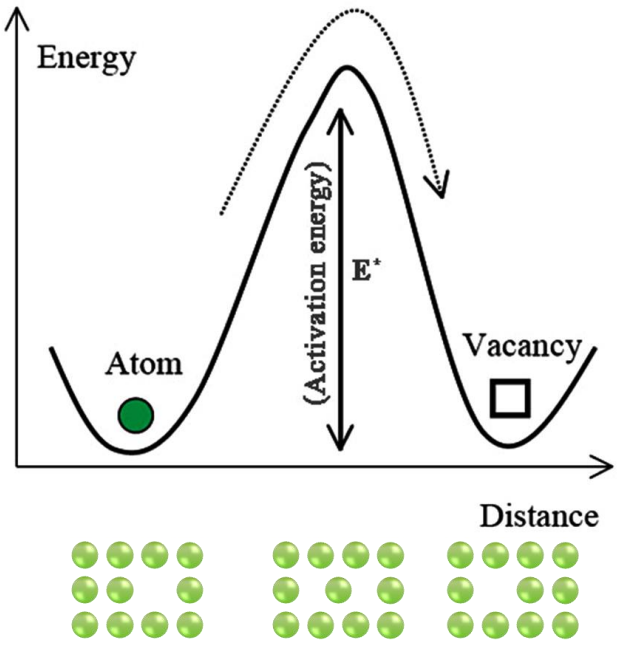

Figure 2.6: Schematic of the diffusion of an atom from its original position into vacant lattice site with assisted from activation energy (E^*).

The activation energy for self-diffusion is the total of activation energy to form a vacancy and to move atom. Generally, as the melting point of the solid increases, so does the activation energy. This relationship exists because solids with higher melting temperature tend to have stronger bonding energies between their atoms. Moreover, atomic size and bonding energy between the atoms are also the factors affecting the diffusion rate in solid.

2.2.3 Fick's First Law

Fick's first law relates the net flow of atoms from the higher concentration to the lower concentration under the assumption of steady-state diffusion condition (no change of concentration with time). The flux or flow of atoms in this is given by

$$\vec{J} = -D\vec{\nabla} C, \qquad (2.3)$$

where $\vec{J}$ = flux or net flow of atoms (atom/m^2·s),

D = proportionality constant called the *diffusivity* (atomic conductivity) or *diffusion coefficient* (m^2/s),

$\vec{\nabla} C$ = concentration gradient (atoms/m^3·m).

A negative sign indicates the diffusion occurs in the direction of decreasing concentration.

2.3 Fundamental Concept of CIGS Materials

2.3.1 Crystal Structure of $CuIn_{1-x}Ga_xSe_2$

The crystal structure of $CuInSe_2$ materials is the I-III-VI_2 (ABC_2) ternary compounds. It virtually exhibits either tetragonal with space group of $I\bar{4}2d$, that is a *chalcopyrite structure* or the doubling cubic unit cell of zinc blend structure with space group $F\bar{4}3m$, that is a *sphalerite structure*. Each A and B-metallic atom is tetrahedrally coordinated to four C non-metallic-atoms while each C-atom is tetrahedrally coordinated to two A-atoms and two B-atoms as depicted in Fig. 2.7. The *c-axis (z direction)* of the tetragonal chalcopyrite structure is not exactly twice of *a-axis* (*x* and *y direction*). It is generally somewhat less than twice the dimension along *a-axis*, i.e., $c \leq 2a$. The primitive unit cell has eight atoms and is four times as large as the primitive unit cell for the sphalerite structure.

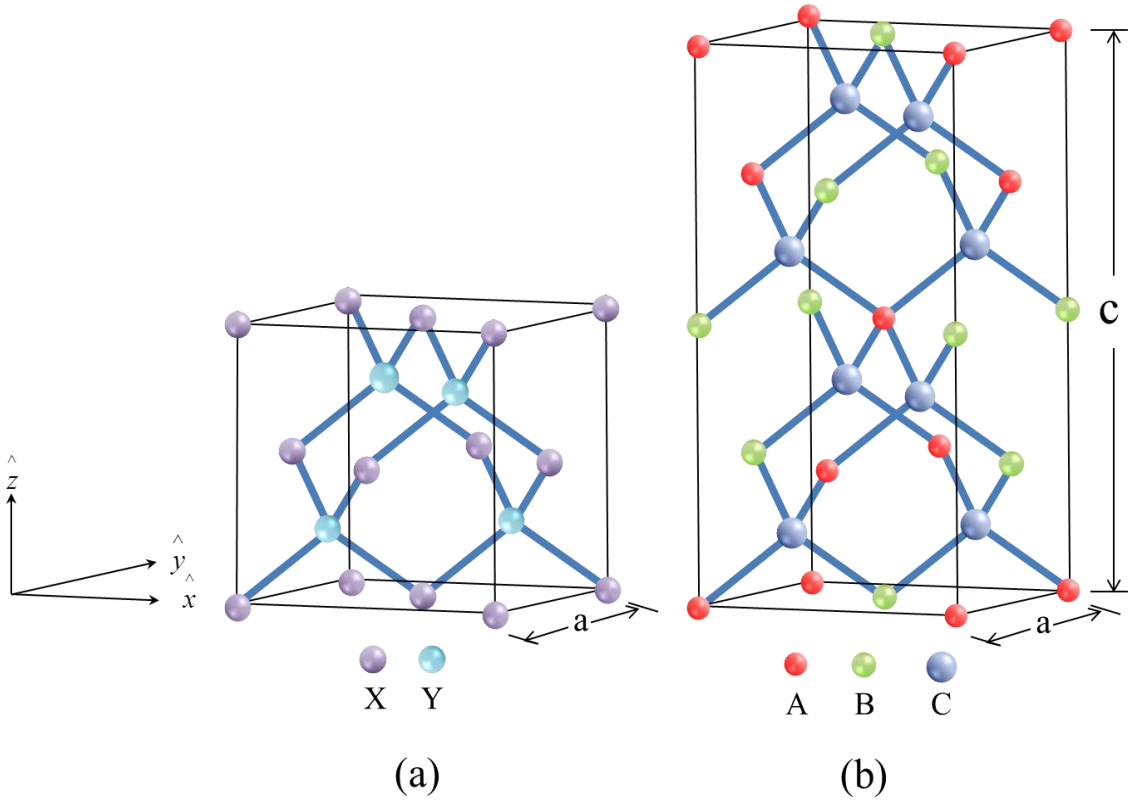

Figure 2.7: (a) sphalerite or zinc blend (X= Zn atom (Cu or In) and Y= Se atom) and (b) Chalcopyrite (A= Cu, B= In and C= Se atom).

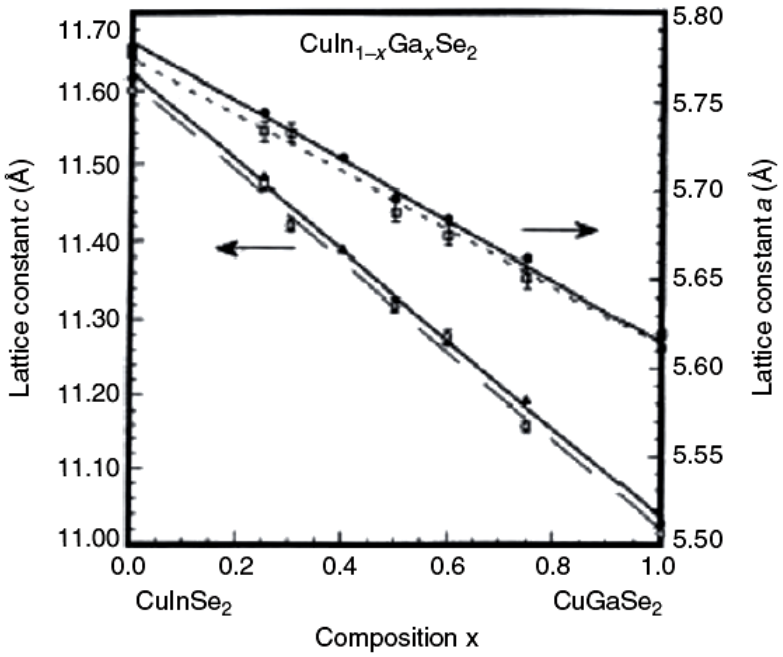

Figure 2.8: Lattice constant of a- and c-axis as a function of the composition parameter of x in the $CuIn_{1-x}Ga_xSe_2$ alloys ([26] and references therein).

By substitution of Ga atoms into In lattice sites in the CIS structure to form the alloying $CuIn_{1-x}Ga_xSe_2$ where x can vary from 0 to 1, results in the reducing of lattice constants (*a* and *c*). Because of the smaller atomic size of Ga than In, so the size of CIS unit cell is decreased. $CuIn_{1-x}Ga_xSe_2$ (CIGS) polycrystalline have been grown by a normal freezing method. The calculated lattice constants of *a-axis* and *c-axis* follow Vegard's law and they are proportional to x composition or group-III atomic ratio ([Ga]/([Ga]+[In]), as shown in Fig. 2.8. These results agree with researcher's reference by the errors of the lattice constants are less than 0.001 Å [26].

2.3.2 Phase Chemistry of Cu-In-Ga-Se Material System

2.3.2.1 The Cu-In-Se Material System

The fundamental of Cu-In-Ga-Se system is similar to that of the Cu-In-Se system. The Cu-In-Se phase is closely related with the *pseudobinary* section between the Cu_2Se and In_2Se_3 compounds, and centered on the equimolar composition corresponding to $CuInSe_2$, as illustrated in Fig. 2.9.

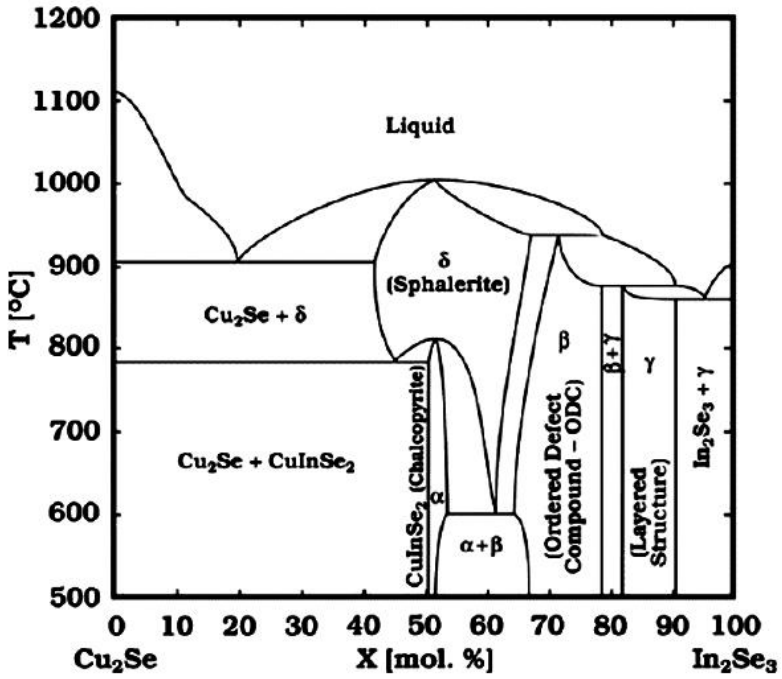

Figure 2.9: Phase diagram along the Cu_2Se-In_2Se_3 pseudobinary section of the Cu-In-Se material system ([27] and references therein).

The crystal structure of α-CIS phase is a chalcopyrite, δ-CIS phase is a sphalerite which is unstable at room temperature, β-CIS phase such as $Cu_2In_4Se_5$ and $CuIn_3Se_5$ are also sometimes referred to "Ordered Defect Compounds" (ODCs) and γ-CIS is the persistence of a close packed lattice of Se atoms, $CuIn_5Se_8$. However, the occurrence of indium binary compound In_2Se_3 mix with γ-CIS phase can be appeared along the Cu_2Se-In_2Se_3 pseudobinary section. The single phase chalcopyrite CIS exists around 50.8-53 mol.% of In_2Se_3 (Cu at.% from 25.4 to 26.5), correspondingly, the Cu atomic ratio (y = [Cu]/[In]) lies approximately between 0.97 and 0.88 as well as in the temperature range from room temperature to 780°C. The $CuInSe_2$ phase along Cu_2Se exists for [Cu]/[In] ≥ 1, including the stoichiometric composition that has two-phase mixture of Cu-deficient α-CIS and $Cu_{2-x}Se$ [27].

2.3.2.2 Defects in Cu-In-Se Material System

The defects that happened in the film formation are induced by the composition of the atomic concentration. In the CIS material, it could be made either n- or p-type; p-CIS materials with low resistivity ($\rho \sim 0.5\ \Omega\cdot$cm) and high mobility of minority carriers ($\mu_e > 500\ cm^2V^{-1}s^{-1}$). By transforming p- to n-type, it is easily achieved by annealing CIS in vacuum or In-atmosphere because of *antisite defects*, e.g. In in Cu lattice sites (In_{Cu}) that is the *donor type defects* [5]. Based on the defect chemistry model of the nearly stoichiometric compound CIS; Rincon *et al.*[28] proposed the deviation of composition from the ideal formula CIS that could be described by two parameters, the *molecularity deviation* (Δm) and the *stoichiometry deviation* (ΔS). The first parameter explains the deviation of Cu and In compositions from the nominal CIS, as define in Eq. 2.4.

$$\Delta m = \frac{[Cu]}{[In]} - 1, \tag{2.4}$$

where [Cu] and [In] are the total atomic concentrations of Cu and In atoms, respectively. In the case of regularity CIS, an excess of Cu compositions, Cu-rich film gives $\Delta m > 0$, meanwhile an excess of In compositions, Cu-poor film gives $\Delta m < 0$. Another parameter describes the film composition whether there are more supplied ($\Delta S > 0$) or deficient ($\Delta S < 0$) of selenium atoms, as define in Eq. 2.5.

$$\Delta S = \frac{2[Se]}{[Cu] + 3[In]} - 1, \tag{2.5}$$

where [Se] is the total atomic concentrations of Se atoms, according to these parameters, the possible majority defect pairs which can be present under $\Delta m < 0$ are summarized in Table 2.1 and satisfied the defect activation energy (formation energy) in CIS given in Table 2.2, where the last two possibilities Se interstitials and In on Se lattice sites are less probable to form due to unfavorable high activation energy.

Table 2.1: Majority defect pairs in $CuInSe_2$ under the excess In compositions with an excess or deficiency of selenium (ΔS) ([28] and reference therein).

Majority defect pair		***Stoichiometry deviation***
Acceptor	***Donor***	***(ΔS)***
V_{Cu}	In_{Cu}	<0
V_{Cu}	V_{Se}	<0
V_{Cu}	In_i	>0
Se_i	In_{Se}	>0
Se_i	In_i	>0

Table 2.2: Formation energies of intrinsic defects in $CuInSe_2$ ([28] and reference therein).

Types of defects		***Formation energy (eV)***
Vacancies	V_{Se}	2.4
	V_{Cu}	2.6
	V_{In}	2.8
Interstitials	Cu_i	4.4
	In_i	9.1
	Se_i	22.4
Antisites	In_{Cu}	1.4
	Cu_{In}	1.5
	In_{Se}	5.0
	Se_{In}	5.5
	Se_{Cu}	7.5
	Cu_{Se}	7.5

2.3.2.3 The Cu-Ga-Se Material System

The phase diagram of the Cu-Ga-Se material system has not been investigated in detail and has more controversial than the Cu-In-Se material system. However, in the earliest study, the Cu-Ga-Se phase was restricted to the pseudobinary Cu_2Se-Ga_2Se_3 section within the ternary phase field. The chalcopyrite phase of CGS is extended further towards Cu-poor composition (20.7% of Cu atomic content) that is lower than that in Cu-In-Se system, as illustrated in Fig. 2.10. The appearance phases on the Cu-poor side are not less complicated than that of the Cu-In-Se system. The additional phases that exist in the phase diagram are $CuGa_3Se_5$, $CuGa_5Se_8$ and Ga_2Se_3 phases, which is a disordered zinc blend (sphalerite) crystal structure.

Interestingly, from the phase diagrams, the melting point of $CuGaSe_2$ ($T_m \approx$ 1050 – 1030°C) is higher than the melting point of $CuInSe_2$ ($T_m \approx$ 986°C). Investigating at the same temperature for the growing film, the lower T_{sub}/T_m ratio appears for the CGS structure. It is not wondering that growth of high-quality CGS films seems to be more "difficult" than growth of CIS films and thus leading to smaller CGS grain sizes.

2.3.2.4 The Cu-Se Material System

Cu-Se phase is frequently found in the Cu-rich ternary compound composition. It can be exhibited in two types; $Cu_{2-x}Se$ and Cu_xSe phases. By the investigation of the microstructure of CIGS grown with the 3-stage process, $Cu_{2-x}Se$ has the cubic phase and resides on the surface of the CIGS structure when Cu atoms exceed the stoichiometry. Whereas, Cu_xSe has the tetragonal structure and resides along the CIGS grain boundary which is formed during the second stage [29]. The liquid Cu-Se phase appears at temperature exceeding 523°C (796K), which enhances CIGS grain growth by a vapor-liquid-solid growth mechanism by improving mobility of the constituent atoms in the liquid phase. At temperatures lower than the melting point, many Cu_xSe phases co-exist depending on the temperature and weight percent of Cu and Se, as illustrated in Fig. 2.11. Nowadays, the role of Cu-Se phase on grain growth and atomic inter-diffusion (In and Ga) remains unclear, however, it is believed as a "quasi-liquid" phase that enhances high diffusivity of elements.

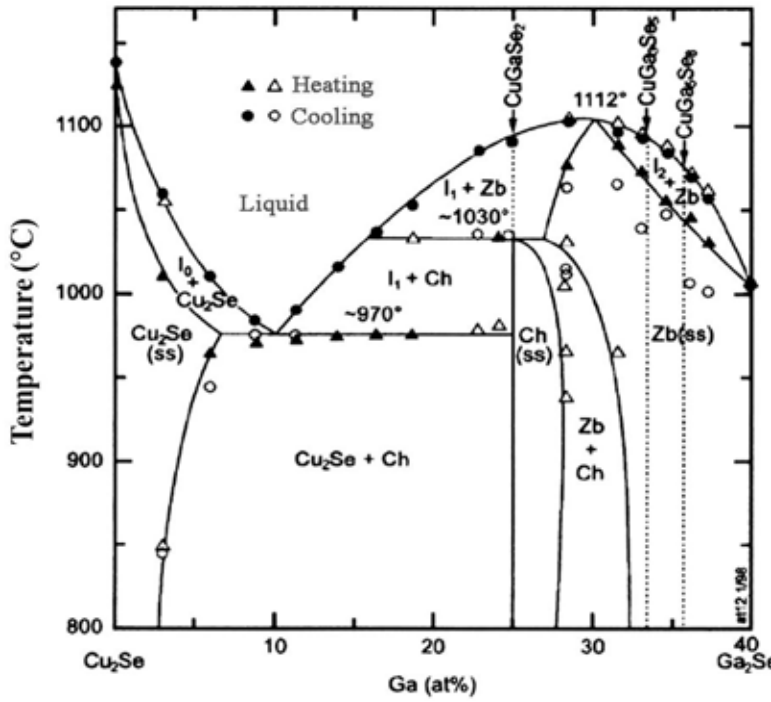

Figure 2.10: Phase diagram of Cu_2Se and Ga_2Se_3 for a formation of CGS compounds

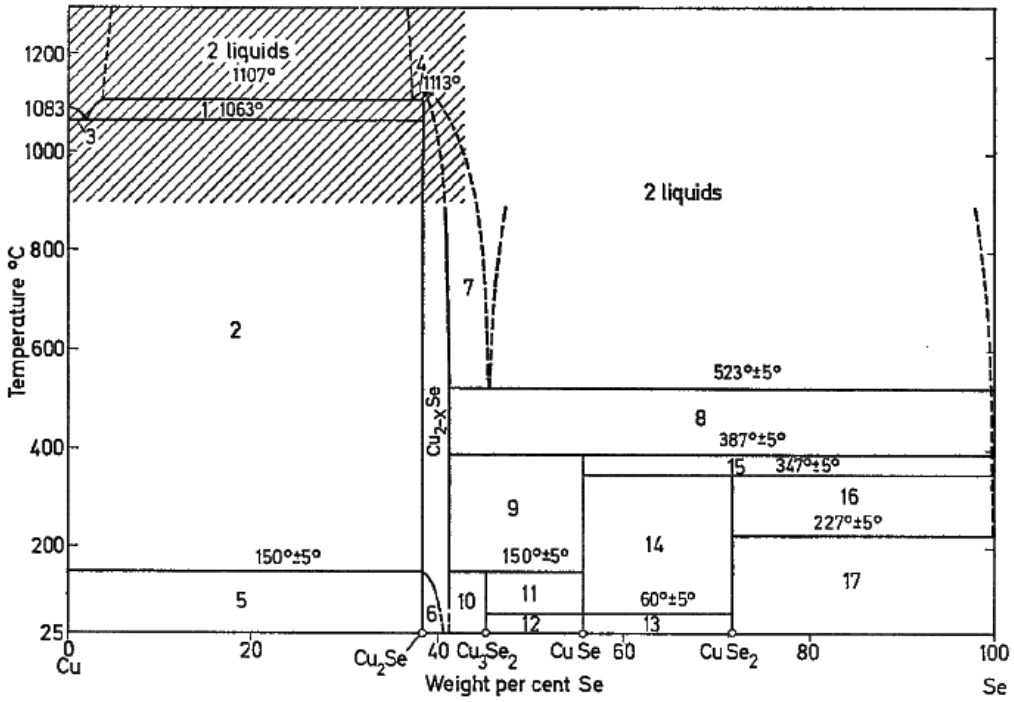

Figure 2.11: Phase diagram of the Cu-Se system above 25 ℃: (1) liquid+β Cu_2Se; (2) Cu+β Cu_2Se; (3) Cu+liquid; (4) liquid+$Cu_{2-x}Se$; (5) Cu+α Cu_2Se; (6) α Cu_2Se+$Cu_{2-x}Se$; (7) $Cu_{2-x}Se$+liquid; (8) $Cu_{2-x}Se$+liquid; (9) $Cu_{2-x}Se$+CuSe h.t.; (10) $Cu_{2-x}Se$+Cu_3Se_2; (11) Cu_3Se_2+CuSe h.t.; (12) Cu_3Se_2+CuSe l.t.; (13) CuSe l.t.+$CuSe_2$; (14) CuSe h.t.+$CuSe_2$; (15) CuSe h.t.+liquid; (16) $CuSe_2$+liquid; (17) $CuSe_2$+Se; h.t.= high temperature; l.t.= low temperature [30].

2.4 Molecular Beam Epitaxy (MBE)

2.4.1 The MBE system

Molecular beam epitaxy (MBE) established itself as a technology of great potential importance for the fabrication of high quality epitaxial semiconductor films with the ability of atomic layer growth. To avoid the contaminations, high purity materials and ultra-high vacuum (UHV) (< 10^{-10} Torr) are required for a long mean free path of the atoms or molecular beam directional flow. The epitaxial film is achieved through the chemical reaction of multiple molecular beams which originate from evaporation or sublimation of elements or sources that are kept in separate effusion cells or Knudsen cell (K-cell), as schematically illustrated in Fig. 2.12. Each K-cell consists of *pyrolitic boron nitride* (*PBN*) crucible housed with tantalum (Ta) heater wire with layers of molybdenum (Mo) radiation shield in order to improve the temperature uniformity. The temperature of the heated source is measured by a tungsten-rhenium (W5%Re-W26%Re) thermocouples and stable source temperature is assured by proportion-integral-deviation (PID) programmable controller.

Molecular beam epitaxial system (EIKO model EW-100) is used for this work either polycrystalline or single crystalline epitaxial bilayer thin films. The system comprises two main parts:

(1) Growth Chamber

- Evaporation sources or K-cells with thermal isolating shutters; Copper (Cu), Indium (In), Gallium (Ga) and Selenium (Se) elements.
- A heated substrate rotation holder.
- In-situ analysis UHV equipment; a residual gas analyzer (RGA), a quartz crystal thickness monitor (QCM), a reflection high energy electron diffraction (RHEED) and a pyrometer.
- Vacuum gauges; pirani gauge (1.3×10^{2} – 1.3×10^{-1} Pa) and nude ionization gauge (10^{-3} – 10^{-11} Torr).
- Titanium sublimation pump (TSP) for ultra-high vacuum.

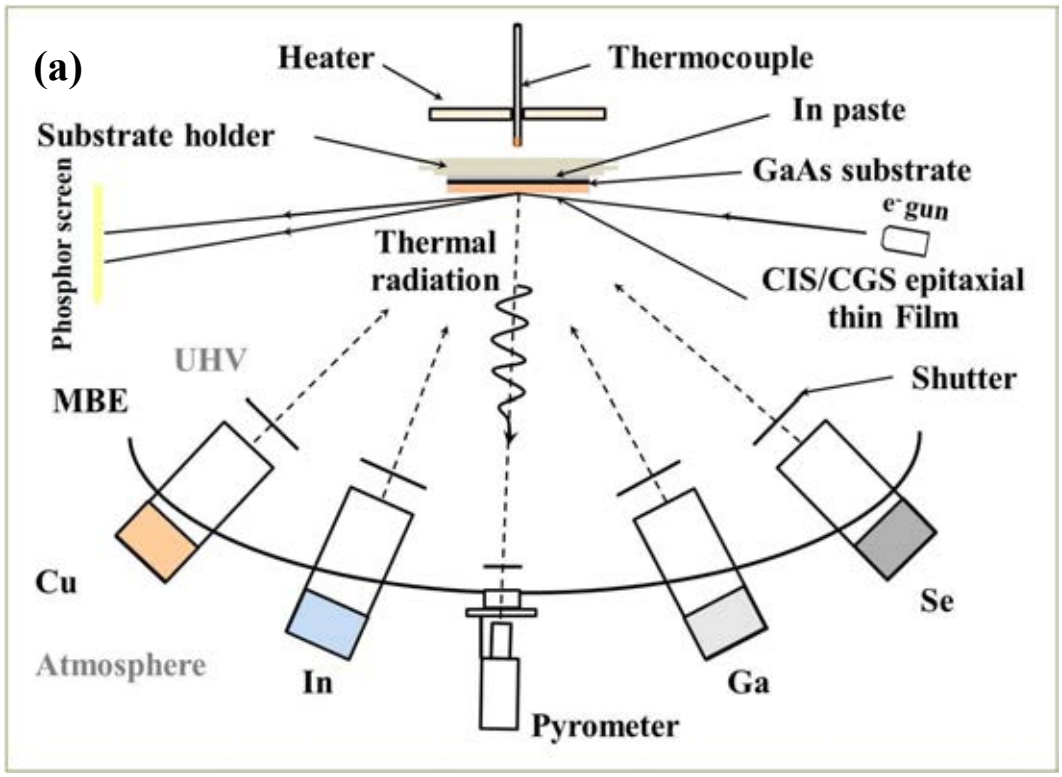

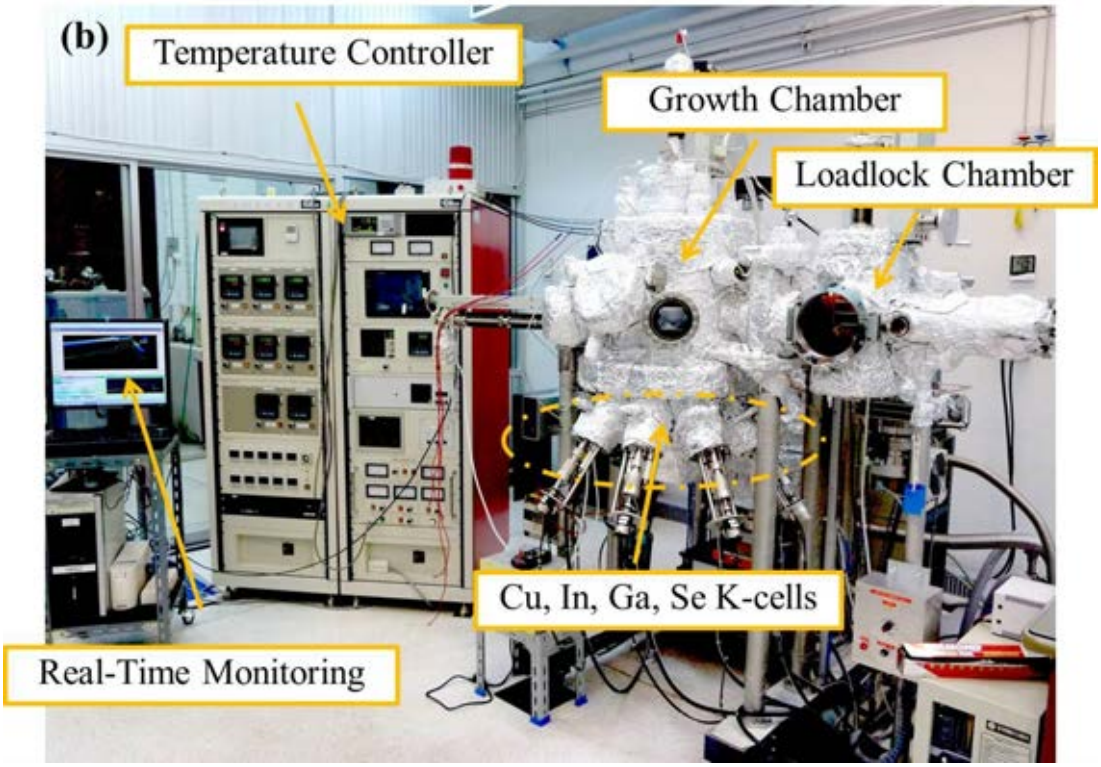

Figure 2.12: (a) The schematic illustration of the MBE system with RHEED and pyrometer setting. (b)The photograph of molecular beam epitaxy system contains all of the components needed for growth and in-situ analysis (SPRL, Chulalongkorn University).

(2) Loadlock chamber

A loadlock chamber is a vacuum chamber that used to exchange a specimen with the growth chamber in order to keep the vacuum and reduce a contamination into the main chamber. In practice, the source temperature at 400°C is maintained for Cu, In and Ga cells. Without an exposure of the main vacuum growth chamber to atmospheric pressure for substrate exchange, it is the also an advantage for improving the crucible life-time as well as the ultimate film purity level.

2.4.2 In situ UHV analysis equipment

2.4.2.1 Residual Gas Analyzer (RGA)

A residual gas analyzer (RGA) is operated based on the *quadrupole mass spectrometer* (*QMS*) for analyzing the contamination and residual gas such as H_2, O_2, H_2O, N_2 and hydrocarbon compounds, etc. in the vacuum systems. The instruments measuring the partial pressure of the residual gases are basically ionization gauges in which the ions formed are resolved by a mass spectrometer. For our system, the RGA has a capacity for determining the composition of gas in the range 1 – 100 AMU, with a resolution of 0.5 AMU and the measurement of partial pressures about 10^{-12} Torr.

2.4.2.2 Quartz Crystal Thickness Monitor (QCM)

To measure a film thickness or a deposition rate for film growth, a quartz crystal thickness monitor is generally used to measure the amount of deposition via its own surface of acoustic resonator. The quartz crystal performs based on a principle of the *piezoelectric effect*. At a constant temperature, the quartz vibrates at its natural frequency, and this frequency is still stable as long as it is not interrupted by the materials deposited on its surface. Depositing of the material on the crystal's surface induces the change of the mass of the crystal. Increasing mass from the deposition results in the change of the resonant frequency of the crystal that is lower and can be detected electronically and converted into the thickness or deposition rate. Due to the fact that quartz crystal is an indirect monitor and stand in the different position from the specimen, the quartz presents an accurate indication only of the film thickness on the crystal itself. Thus, it is not a true representation of the thickness of the film being

deposited on actual substrate position. However, it can give a very close to real values of thickness or deposition rates with appropriate correction factor.

2.4.2.3 Reflection High Energy Electron Diffraction (RHEED)

There are many observations for film formation or growth modes; (1) island (or *Volmer-Weber, VW*) growth (2) layer (or *Frank-Van der Merwe, FV*) growth and (3) layer growth following by island growth (*Stranki-Krastanov, SK*), as shown in Fig. 2.13 [24]. High-quality layer-by-layer growth is essential for the production of epitaxial thin film by MBE system. The *in-situ* RHEED apparatus is reliable to monitor the presence or absence of FV growth during deposition of materials.

The RHEED system consists of an electron gun and a phosphor screen, the acceleration voltage for a commercially available RHEED system is typically between 5 – 50 keV. In our work for bilayer epitaxial thin film, the voltage used for investigating the sample is 15 keV. Electron beam is directed towards the sample at grazing incidence. Electrons scatter through small angles, only the top 1 – 2 atomic layers of the crystal, and a diffraction pattern appears on the phosphor screen.

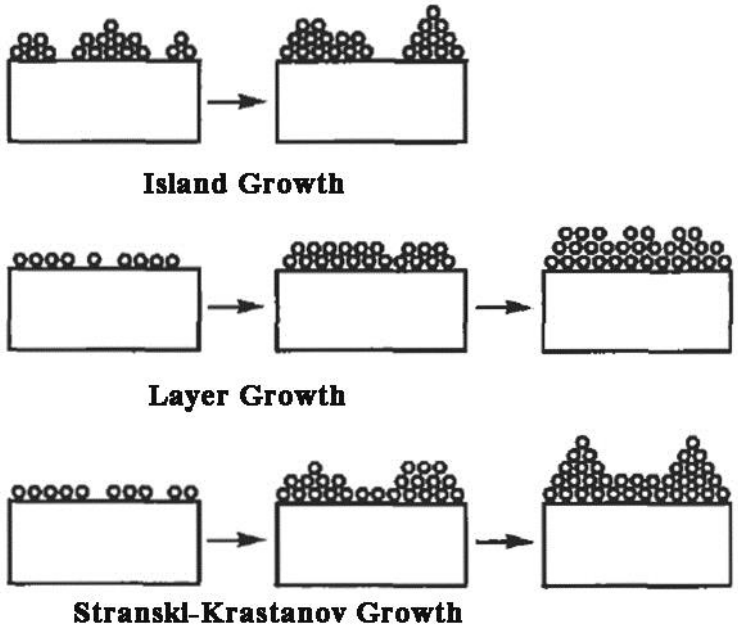

Figure 2.13: The Schematic illustration of three basic growth modes of thin film; island growth, layer by layer and the combination of layer by layer follows with island growth.

The RHEED pattern is originated from the intersection between the finite width of Ewald sphere and the reciprocal lattice rods which occur for some distance along their height, as depicted in Fig. 2.14. The resulting patterns appear in either streaked or spotty diffraction patterns. The spotty patterns happen as a result of island growth or surface asperities, whereas streaks characterize smooth layered film growth, as shown in Fig. 2.15.

2.4.2.4 Pyrometer

The pyrometer is normally used for monitoring the emissivity radiation from the focus center of the front surface of the substrate which converts the radiation signals into the temperature obeying the Stefan-Boltzmann's radiation law. The pyrometer (IR-FA model) contains a high resolution monochromatic (InGaAs, 1.55 μm) fiber optic type that responds to the range of infrared radiation, 250 – 1000°C. For CIGS thin film growth using the 3-stage or 2-stage processes, the thermal radiation signals from the pyrometer can be used to observe the conversion of the composition of CIGS thin films [31]. Additionally, the signals from pyrometer also yield the thickness of the film by observing the period of oscillations due to the interference by the multiple reflections of thermal radiation at the back and the front surface of the growing films.

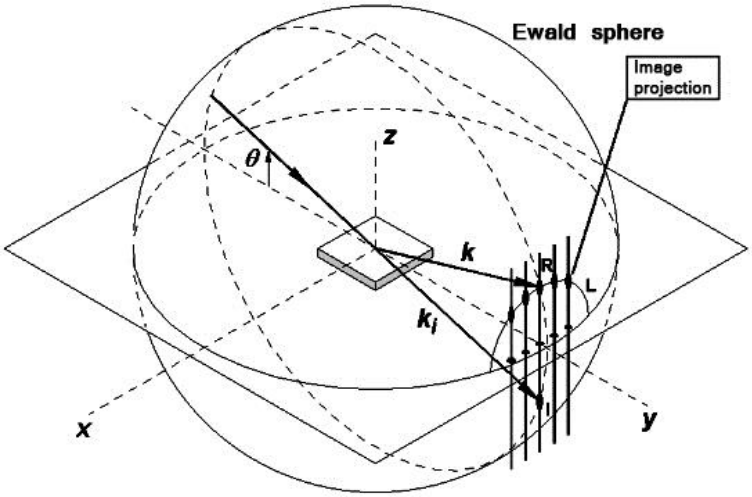

Figure 2.14: The schematic diagram of RHEED analysis. The vertical lines are the reciprocal lattice rods; the pattern appears for distance of the intersection between the Ewald sphere and rods.

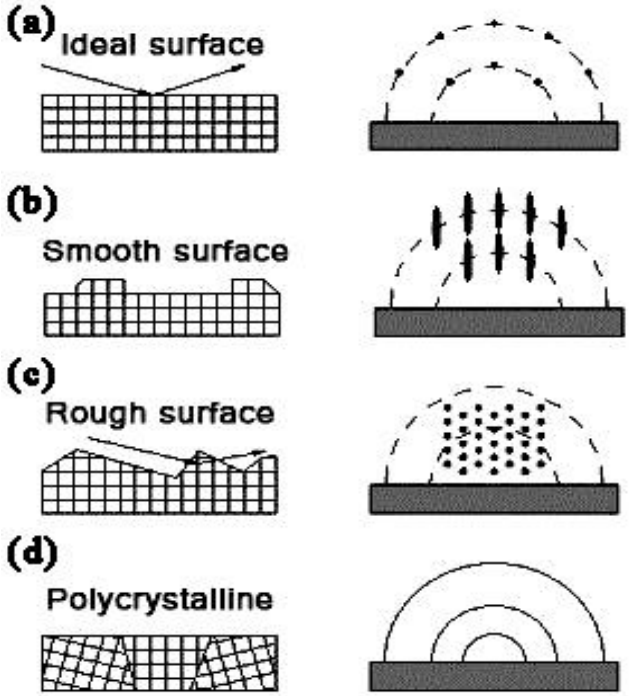

Figure 2.15: RHEED patterns correspond to the different types of film surface (b, c) and types of crystalline structure (a, d).

Chapter III

CIS/CGS Bilayer Growth and Measurement Techniques

In the beginning, the substrate preparations are given, followed by the calibration of molecular constituents in order to obtain the desired film composition and thickness. The growth details of the CIS/CGS bilayer films via molecular beam deposition (MBD) technique for both polycrystalline films on soda-lime glass (SLG) substrates and epitaxial films on GaAs(001) substrates are discussed. Then, the tools for the sample characterization are briefly described in their basic principles.

3.1 Substrate Cleaning Procedures

3.1.1 Soda-Lime Glass (SLG) Preparation Procedures

Soda-lime glass is an appropriate substrate for CIGS thin film solar cells because of its well-matched thermal expansion coefficient. In addition, Na in SLG can diffuse into the CIGS layer through molybdenum (Mo) back-contact layer during CIGS deposition process resulting in the increase of CIGS solar cell performance and also enhance surface morphology. The cleaning steps of the SLG substrates are as followed:

1. Soak the SLG substrates in deionized water (~ 18.3 MΩ·cm, DI water) with dishwashing detergent for 15 minutes in order to remove grease from the surface.
2. Thoroughly scrub the SLG substrates with a cellulose sponge and clean with the DI water.
3. Soak the SLG substrates in an ultrasonic bath with a mixture of the glassware detergent (Micro-90) and DI water at 60°C for an hour, and rinse with DI water.
4. Soak the SLG substrates in chromic acid (H_2CrO_4) for an hour for surface treatment (creating rough surface), and rinse with DI water.

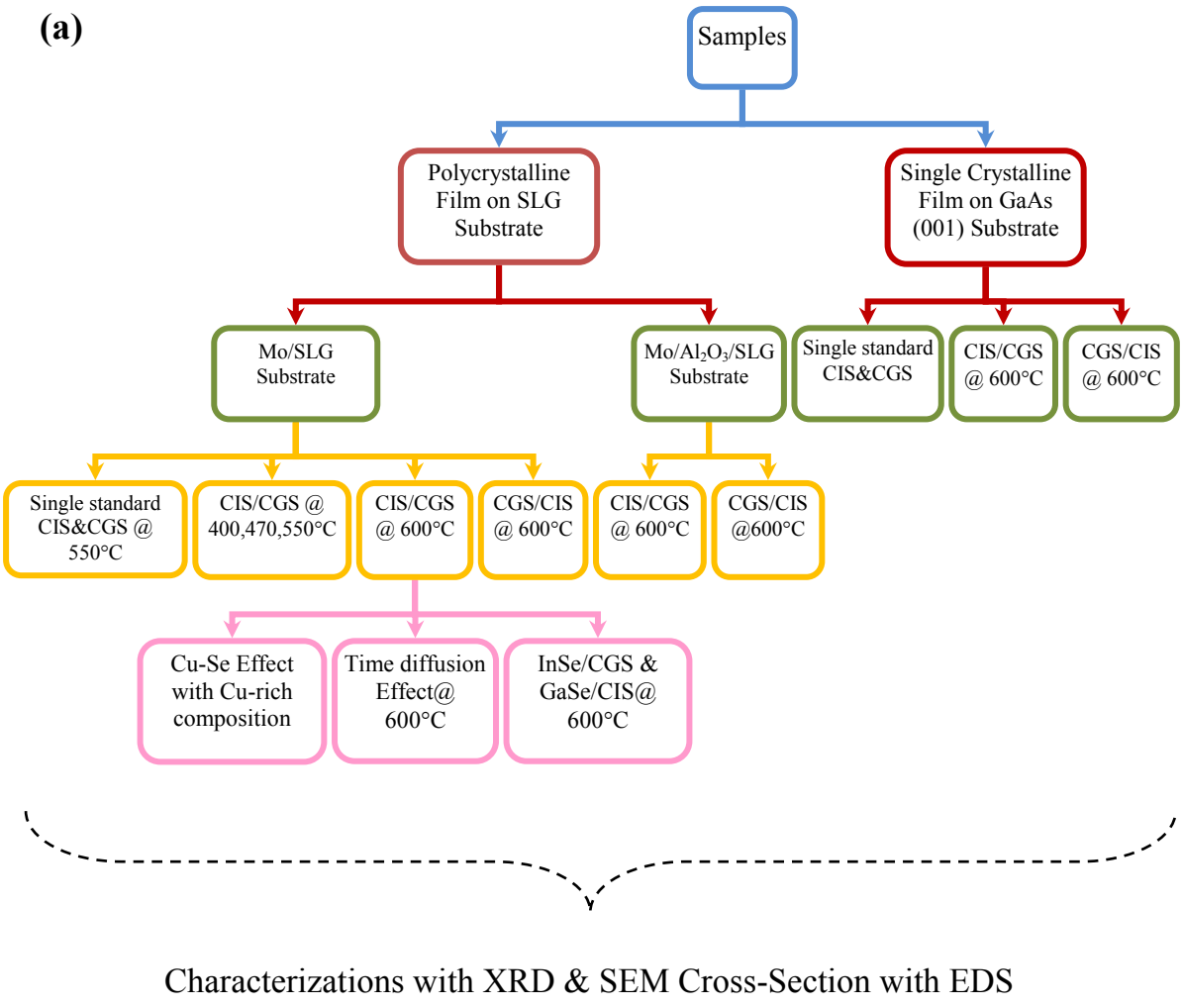

Figure 3.1: (a) Schematic diagram of experimental design in this research. (b) Diagram of varying compositions between Cu-rich (y = 1.2) and Cu-poor (y = 0.85) in CIS/CGS and CGS/CIS bilayers.

5. Soak the SLG substrates in NaOH base solution for an hour in order to remove a residual chromic acid, and provide saturate Na.
6. Thoroughly soak the SLG substrates again in DI water using an ultrasonic bath.
7. Dry the substrates with the compressed nitrogen gas and keep in a dry cabinet before loading into the next process.

Aside from enhancing Na out-diffuse from the SLG substrate, Mo layer is also used for adhesive cohesion between the substrate and the CIS or CGS thin films. Thus, the Mo layer is deposited for the thickness ~ 600 nm by DC magnetron sputtering using a 4-inch diameter Mo target with a sputtering power of 550W for 12 minutes. After accomplishing the Mo back-contact, it is ready for the deposition of the CIS/CGS or CGS/CIS bilayers.

In order to study the influence of Na on Ga diffusion in the bilayers, the blocking of Na out-diffusion from the SLG is achieved by deposition of Al_2O_3 thin film on the SLG. The Al_2O_3 is deposited by RF magnetron sputtering using a 4-inch diameter Al_2O_3 ceramic target with a sputtering power of 280W. The required thickness of Al_2O_3 layer is about ~ 1μm.

3.1.2 GaAs(001) Wafer Preparation Procedures

Cleaning of GaAs wafer was generally to remove undesirable materials lying on the surface such as the visible dirt, all the contaminants physically stuck on the surface (oil, grease) or resulting from a chemical reaction (oxides, sulfides). The degree of GaAs cleanliness must be as high as possible for layer-by-layer epitaxial thin film growth under ultra-high vacuum. The following steps are taken:

1. Blow with the compress nitrogen gas on the surface of GaAs wafer to remove grime particles.
2. Clean the wafer for 10 minutes in a beaker of Trichloroethylene (TCE, C_2HCl_3) solution, wherein an ultrasonic bath is utilized in order to remove organic contamination that might be left on the surface from the production.

3. Clean the wafer for 10 minutes in a beaker of acetone ($(CH_3)_2CO$) solution in an ultrasonic bath to further remove organic contamination and residual TCE.
4. Clean the wafer for 10 minutes in a beaker of methanol (CH_3OH) solution in an ultrasonic bath to further remove organic contamination and remaining acetone.
5. Clean the wafer for 10 minutes in a beaker of DI water in an ultrasonic bath to further remove the remaining of contaminants and residual methanol.
6. Thoroughly rinse the wafer in DI water and blow dry with compressed nitrogen gas. Finally, keep in a dry cabinet for the next process.

Next steps are the chemical etching to prepare the surface of GaAs wafer before loading into the deposition chamber. A solution for etching consists of 98 weight percent of sulfuric acid, 30 weight percent of hydrogen peroxide and DI water. The concentration ratios of the etchants are $5H_2SO_4$: H_2O_2: H_2O by volume. The sulfuric acid converts organic compounds to elemental carbon. The hydrogen peroxide then oxidizes the carbon to carbon dioxide and water. Steps for etching the GaAs wafer are as followed:

1. Mix the proper quantities of H_2SO_4 with H_2O in the fume hood and cool to room temperature (25°C).
2. Slowly add H_2O_2 into the mixture from step 1 in the ice bath in order to avoid temperature increasing since the influence of the temperature and concentration of the particular etchant components affect the etching rate and the shape of the crystal surface [32].
3. Dip the wafer in the etchant for 1 minute and agitate every 15 seconds by tweezers to remove metal ions and oxidize the surface.
4. Dip the wafer in a beaker of DI water and then rinse in running DI water for 2-3 minutes to remove the etchant.
5. Transfer the wafer carefully into a dry place and then blow dry with compressed nitrogen gas.

After the preparation of GaAs surface, the wafer is mounted on the sample holder (made of Mo) using small amount of In solder on the hot plate around 160-180 °C for adhesion between the wafer and substrate holder. Then slide the wafer back and forth along the holder until the substrate is mounted firmly with the surface tension. After the substrate holder cools down, it is ready to be installed in the growth chamber for thin film deposition.

3.2 $CuInSe_2/CuGaSe_2$ Bilayer Thin Films

3.2.1 Calibration of Molecular Constituents

Thin films of CIS/CGS and also CGS/CIS bilayers were grown by MBE system from solid sources of Cu (5N), In (6N), Ga (7N) and Se (5N) by co-evaporation of the elements in each K-cell. Since the vapor pressures of the elements are different (related to the temperature of melting point), so the working ranges of temperature to provide the evaporation rate of the elements are also different. Before the growth of bilayers, it is necessary to check the evaporation rate of each source at different temperatures in the range of working temperature by using the quartz thickness monitor (QCM). These data will be plotted following the relationship between the deposition rate and the effusion cell temperature given by

$$\ln(r) = a\frac{1}{T} + b, \qquad (3.1)$$

where r is the deposition rate (Å/s), T is the effusion cell temperature (°C), a and b are parameters obtained by the least-square fit. The plot of the logarithm of deposition rate versus the inversed effusion-cell-temperature of Cu, In and Ga are shown in Fig. 3.2 and it is noted here that the deposition rate of Se is not included in this process because it is always oversupplied during the film deposition.

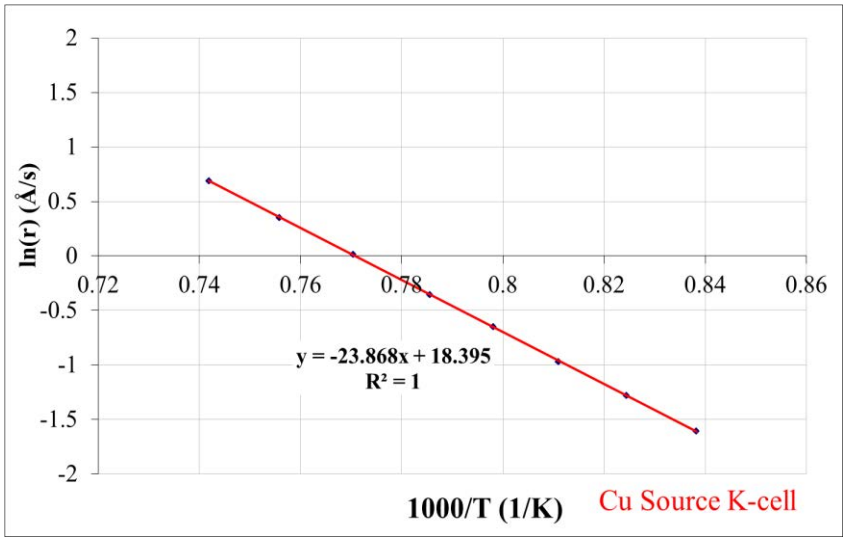

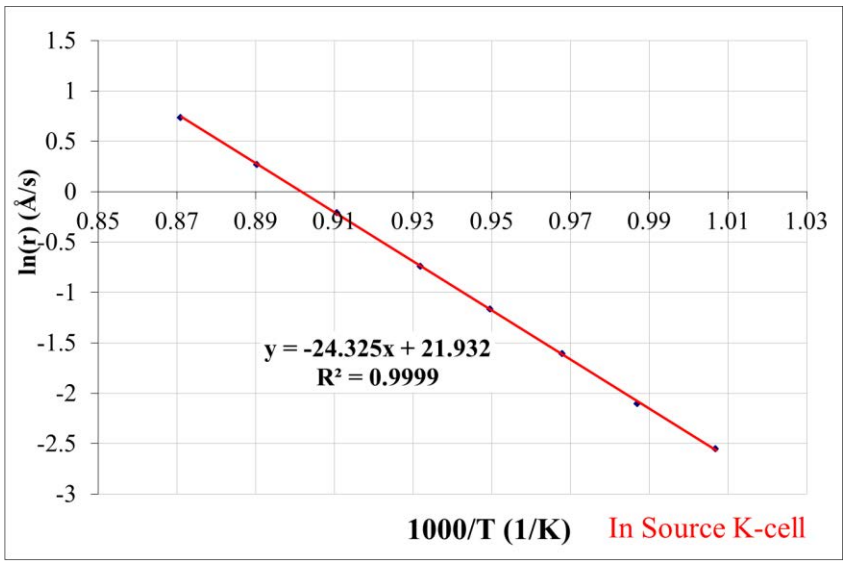

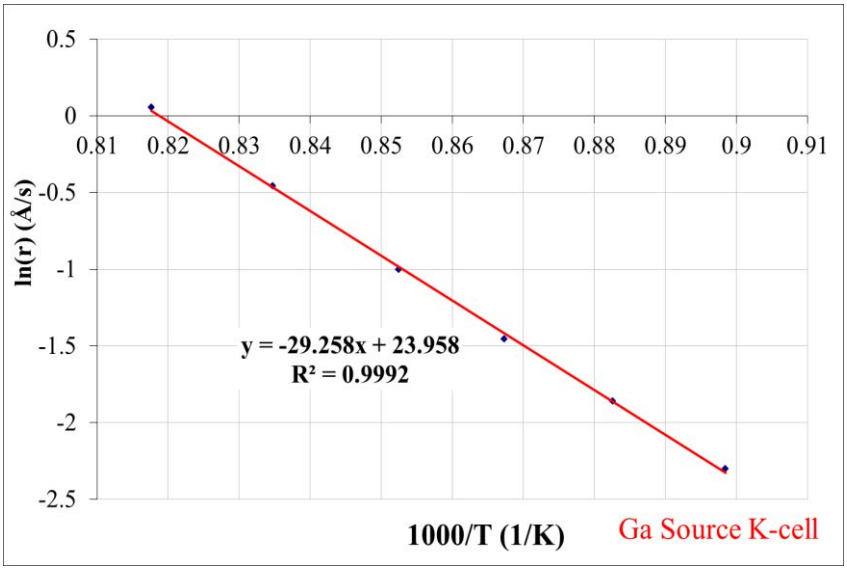

Figure 3.2: Plots of deposition rate and inverse temperature for K-cell calibrations.

3.2.2 Calculation of the CIGS Film Deposition

After obtaining the fitting parameters *a* and *b* from Eq. (3.1) for each source and suppose a certain thickness of film is required, one must know the deposition rate of the elements in order to set the deposition temperature in each K-cell. Firstly, I determine the rate of Cu (r_{Cu}) by using the equation

$$r_{Cu} = \frac{d_{Cu}}{t_{Cu}}, \tag{3.2}$$

and $$d_{Cu} = \frac{N_{Cu} \cdot (M_{Cu}) \cdot (\rho_{CIS} \cdot (1-x) + \rho_{CGS} \cdot x)}{N_{CIGS} \cdot (M_{Cu} + M_{In} \cdot (1-x) + M_{Ga} \cdot x + 2 \cdot M_{Se}) \cdot (\rho_{Cu})} \cdot d_{CIGS}, \tag{3.3}$$

where r_{Cu} is the deposition rate of the Cu element (Å/s),

d_{Cu} is the thickness of the Cu element (Å),

t_{Cu} is the total time for deposition of Cu element,

N_{Cu} and N_{CIGS} are the number of Cu atoms and CIGS molecules that is set N_{Cu}/N_{CIGS} equal unity,

x is the ratio of group-III elements [Ga]/([Ga]+[In]) that corresponds to the alloying combination between $CuInSe_2$ (CIS; x=0) and $CuGaSe_2$ (CGS; x=1) of $Cu(In_{1-x}Ga_x)Se_2$ film,

M_i is the molecular mass of each element,

ρ_i is the density of each element.

The rate of Ga and In (r_{In}, r_{Ga}) can be derived from the ratio of group-III elements and Cu-atomic composition,

$$x = \frac{[Ga]}{[Ga]+[In]} = \frac{N_{Ga}}{N_{Ga}+N_{In}}, \tag{3.4}$$

and $$y = \frac{[Cu]}{[Ga]+[In]} = \frac{N_{Cu}}{N_{Ga}+N_{In}}, \tag{3.5}$$

The number of atoms of each element (N_{Ga}, N_{In} and N_{Cu}) is

$$N_i = \frac{\rho_i \cdot V \cdot N_A}{M_i} = \rho_i \cdot M_i^{-1} \cdot d_i A \cdot N_A \tag{3.6}$$

Then, the ratio of x and y compositions in a unit area of CIGS thin film can be written as;

$$x = \frac{\rho_{Ga} \cdot M_{Ga}^{-1} \cdot d_{Ga} \cdot A \cdot N_A}{(\rho_{Ga} \cdot M_{Ga}^{-1} \cdot d_{Ga} + \rho_{In} \cdot M_{In}^{-1} \cdot d_{In}) \cdot A \cdot N_A}, \tag{3.7}$$

and

$$y = \frac{\rho_{Cu} \cdot M_{Cu}^{-1} \cdot d_{Cu} \cdot A \cdot N_A}{(\rho_{Ga} \cdot M_{Ga}^{-1} \cdot d_{Ga} + \rho_{In} \cdot M_{In}^{-1} \cdot d_{In}) \cdot A \cdot N_A}, \tag{3.8}$$

where A is the unit area of the growing film,

N_A is *Avocadro's constant* = 6.02×10^{23} atoms or molecules.

From the expression of x and y in Eq. (3.7) and (3.8) respectively, I define the parameter α_i as the ratio of density to molecular mass of each element.

$$\alpha_{Cu} = \rho_{Cu} \cdot M_{Cu}^{-1}, \tag{3.9a}$$

$$\alpha_{In} = \rho_{In} \cdot M_{In}^{-1}, \tag{3.9b}$$

and

$$\alpha_{Ga} = \rho_{Ga} \cdot M_{Ga}^{-1}, \tag{3.9c}$$

where the density (ρ_i) and molecular mass values (M_i) of the materials are given in Table 3.1

Table 3.1: Density, mass per mole and α_i parameter of the materials.

Material	ρ **(g/cm^3)**	M **(g/mole)**	$\alpha = \rho/M$ **(mole/cm^3)**
Cu	8.96	63.55	0.1410
In	7.31	114.82	0.0637
Ga	5.91	69.72	0.0848
Se	4.79	78.96	0.0607
CIS	5.89	336.29	-
CGS	5.27	291.19	-

Substituting Eqs. (3.9*a*), (3.9*b*) and (3.9*c*) into Eqs. (3.7) and (3.8), then the relationship of the metal film thicknesses is obtained;

$$d_{Ga} \cdot \alpha_{In} + d_{Ga} \cdot \alpha_{Ga} = d_{Cu} \cdot \alpha_{Cu} \cdot \frac{1}{y} = d_{Ga} \cdot \alpha_{Ga} \cdot \frac{1}{x} \tag{3.11}$$

Rearranging Eq. (3.11) to obtain

$$d_{Ga} = \frac{x}{y} \cdot \frac{\alpha_{Cu}}{\alpha_{Ga}} \cdot d_{Cu} \tag{3.12}$$

$$d_{In} = \frac{(1-x)}{y} \cdot \frac{\alpha_{Cu}}{\alpha_{In}} \cdot d_{Cu} \tag{3.13}$$

Since, the thickness of the element is proportion to the total time for deposition the element, $d_i = r_i \cdot t_i$. Thus, Eq. (3.12) and Eq. (3.13) become

$$r_{Ga} = \frac{x}{y} \cdot \frac{\alpha_{Cu}}{\alpha_{Ga}} \cdot r_{Cu} \tag{3.14}$$

$$r_{In} = \frac{(1-x)}{y} \cdot \frac{\alpha_{Cu}}{\alpha_{In}} \cdot r_{Cu} \tag{3.15}$$

Substituting r_{Cu}, r_{Ga} and r_{In} back into Eq. (3.1), including fitting parameters, *a* and *b*, that obtained from the graphs between logarithm of deposition rate and inverse temperature, I then have the working temperatures for the deposition of CIGS thin films. The details for the deposition of CIS/CGS films are described in the next section.

3.2.3 Deposition of the CIS/CGS Bilayer Thin Films

The deposition method of CIS/CGS bilayers bases on the single-stage growth process of CIGS absorber layer thin film solar cells. This method uses simultaneous deposition of all elements at constant evaporation rates and constant substrate temperature until the end of time for desired film thickness. The composition of the growing film is either Cu-rich or Cu-poor. In bilayer CIS/CGS, the composition of CGS and CIS were varied for both Cu-rich and Cu-poor compositions as described in Fig. 3.1(b). In order to fabricate the CIS/CGS bilayer, firstly, the Cu, Ga and Se constituents are deposited simultaneously, and then following by Cu, In and Se. For example, the parameters for the growth of Cu-rich CIS/Cu-rich CGS are shown in Table 3.2 and the evaporation profile of the process is illustrated in Fig. 3.3.

Table 3.2: Parameters for the growth of CIS/CGS bilayers.

Parameters	**Required data**	
	$CuGaSe_2$	**$CuInSe_2$**
$d_{CGS,\ CIS}$	400 nm	600 nm
t_{Cu}	960 s	1440 s
x	1.0	0.0
y	1.2	1.2
Parameters	**Calculated data**	
	$CuGaSe_2$	**$CuInSe_2$**
d_{Cu}	515.179 Å	515.179 Å
r_{Cu}	0.537 Å/s	0.537 Å/s
r_{Ga}	0.739 Å/s	-
r_{In}	-	0.988 Å/s
T_{Cu}	982°C	982°C
T_{Ga}	933°C	-
T_{Ga}	-	836°C

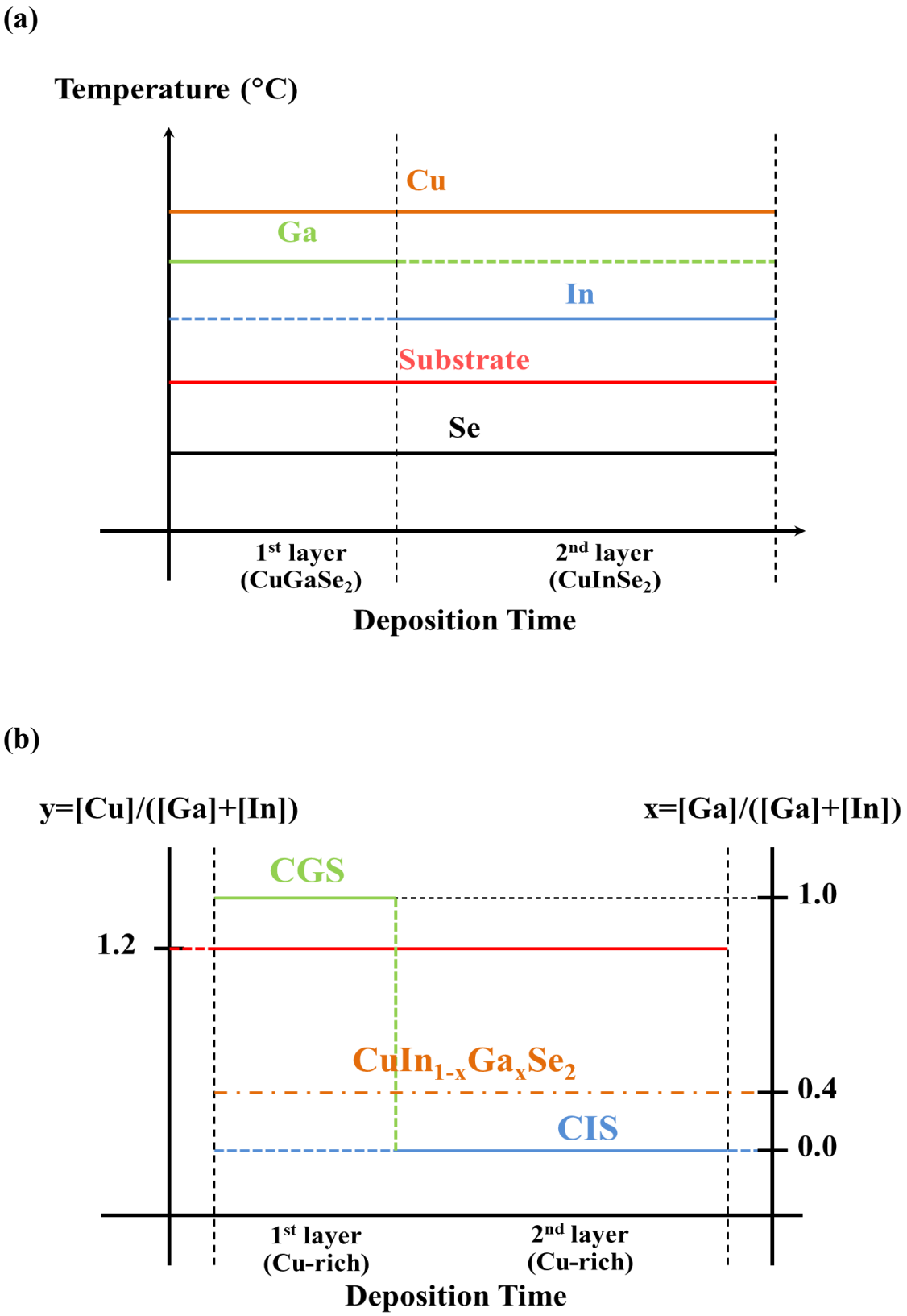

Figure 3.3: (a) Temperature profiles of source elements and substrate for Cu-rich CIS/CGS bilayer. (b) Film compositions; x and y during the deposition process.

3.3 Film Characterization techniques

In order to describe the diffusion of Ga in the bilayers, it is necessary to use the instruments to study and understand the mechanisms forming the alloying of CIGS thin films based on the microstructure, microconstituents, and internal structure of the bilayers. In the following subsections, the details of scanning electron microscopy (SEM), energy dispersive X-ray spectroscopy and X-ray diffraction (XRD) are briefly described for their basic principles.

3.3.1 Scanning Electron Microscopy (SEM)

Scanning electron microscope is an important tool that is used for microscopic feature measurement and microstructure studies. The SEM impinges a beam of electrons in a pinpointed spot on the surface or cross-section of a target specimen, collects and displays the electronic signals given off by the target materials.

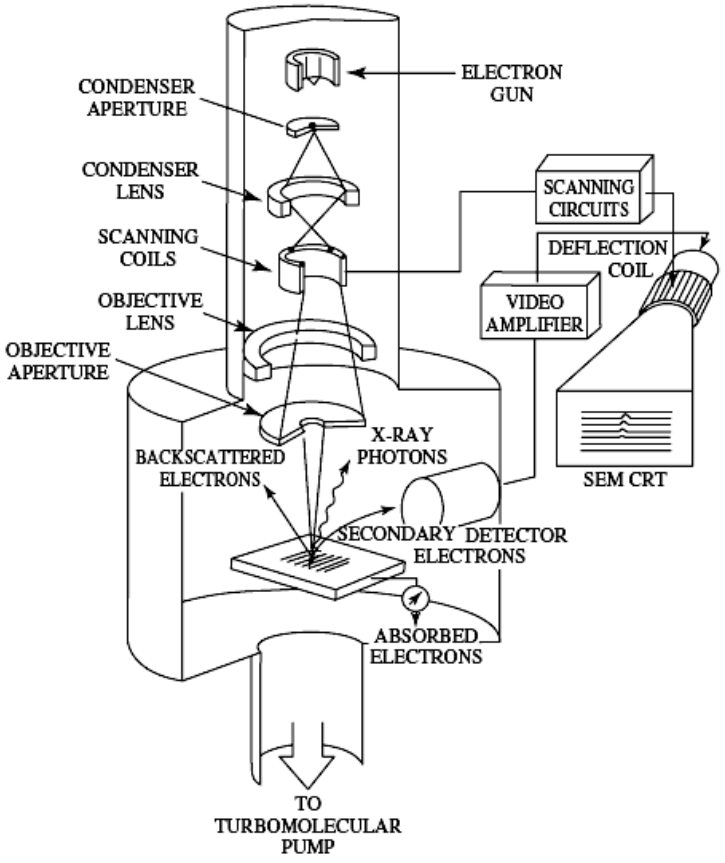

Figure 3.4: Schematic of a scanning electron microscope [33]

The resolution of JEOL JSM-7001F FESEM used in this work is about 1.2 nm at 30 kV, with a wide range of magnification (about 25 to 1,000,000×). The SEM is used to examine the surface and the cross-sectional analysis of stacking of the bilayers. The samples to be analyzed using SEM are often bound with a thin conductive layer such as silver paint to achieve better resolution and signal quality.

3.3.2 Energy Dispersive X-ray Spectroscopy (EDS or EDX)

Energy dispersive x-ray analysis system is generally interfaced with the SEM, where the electron beam serves to excite characteristic X-rays from the area of the specimen being probed. EDS is used for inspection of the elemental composition or chemical characterization of thin films. Ordinarily, EDS has an effective probe depth of ~ 1 μm and is restricted only detect elements with Z > 5 (Boron, B). The detection limits for EDS are ranging from ~ 0.1 to 1 at.% when a Beryllium (Be) window is used as the detector. In this work, the samples were analyzed with an acceleration voltage of 15 kV. The compositions of the elements are roughly probed in depth profiles in order to investigate the trend of group-III elements diffusion in the bilayers.

3.3.3 X-Ray Diffraction Analysis of Crystal Structures

The studying the Ga diffusion in this work are investigated mainly by X-ray diffraction technique to identify the crystallographic phase and analyze the crystalline structure. X-rays used for diffraction are electromagnetic waves with wavelengths ~ 0.5 – 2.5 Å. In this work, the Bruker D8 Advance X-ray powder diffractometer emitted the wavelength of $Cu_{K\alpha1}$ (λ = 1.5406 Å) and $Cu_{K\alpha2}$ (λ = 1.54439 Å) radiations at 40 kV using copper target was used. When an incident beam of X-rays strikes the set of crystal planes that act as mirrors in reflecting the incident X-ray beams, at an angle such that the wave patterns of the beam leaving the various planes are in phase, then the reinforcement of the beam or constructive interference waves occurs as shown in Fig. 3.5. These constructive waves are satisfied by Bragg's condition,

$$2d_{hkl}\sin\theta = n\lambda, \tag{3.16}$$

that gives the relationship among the angular positions of the constructive diffracted beams in terms of the wavelength λ of the incoming X-ray radiation and of the

interplanar spacings d_{hkl} of the crystal plane. In most cases, the first order of diffraction where $n = 1$ is used.

The XRD patterns are collected in a range 20° – 30° of 2θ that correspond to the crystal orientation (112) of $CuIn_{1-x}Ga_xSe_2$ alloying chalcopyrite phase where the lattice parameters a and c can be determined from the tetragonal unit cell system given by

$$\frac{1}{d^2} = \frac{h^2 + k^2}{a^2} + \frac{l^2}{c^2}, \tag{3.17}$$

and h, k and l are the Miller indices of the diffraction planes, a and c are the lattice parameters. For the case of the bilayers, the XRD was used to analyze the shift of the CIS and CGS peaks in the XRD patterns with respect to the standard CIS and CGS films. The peak positions will be treated by the Lorenzian fitting method [34]. To illustrate this approach, it is easy to refer to the diagram showing the (112) peak intensities that result from the inter-diffusion of Ga and In in CIS/CGS bilayer as shown in Fig. 3.6.

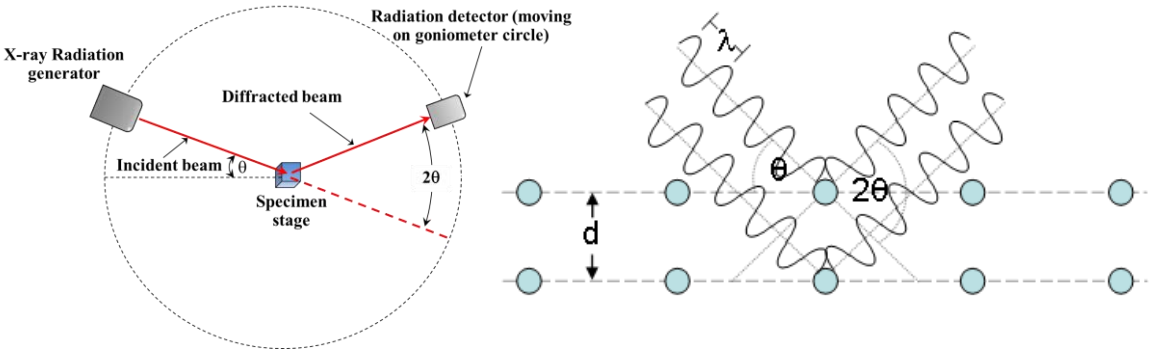

Figure 3.5: Schematic illustration of the diffractometer of crystal analysis and of the conditions necessary for diffraction.

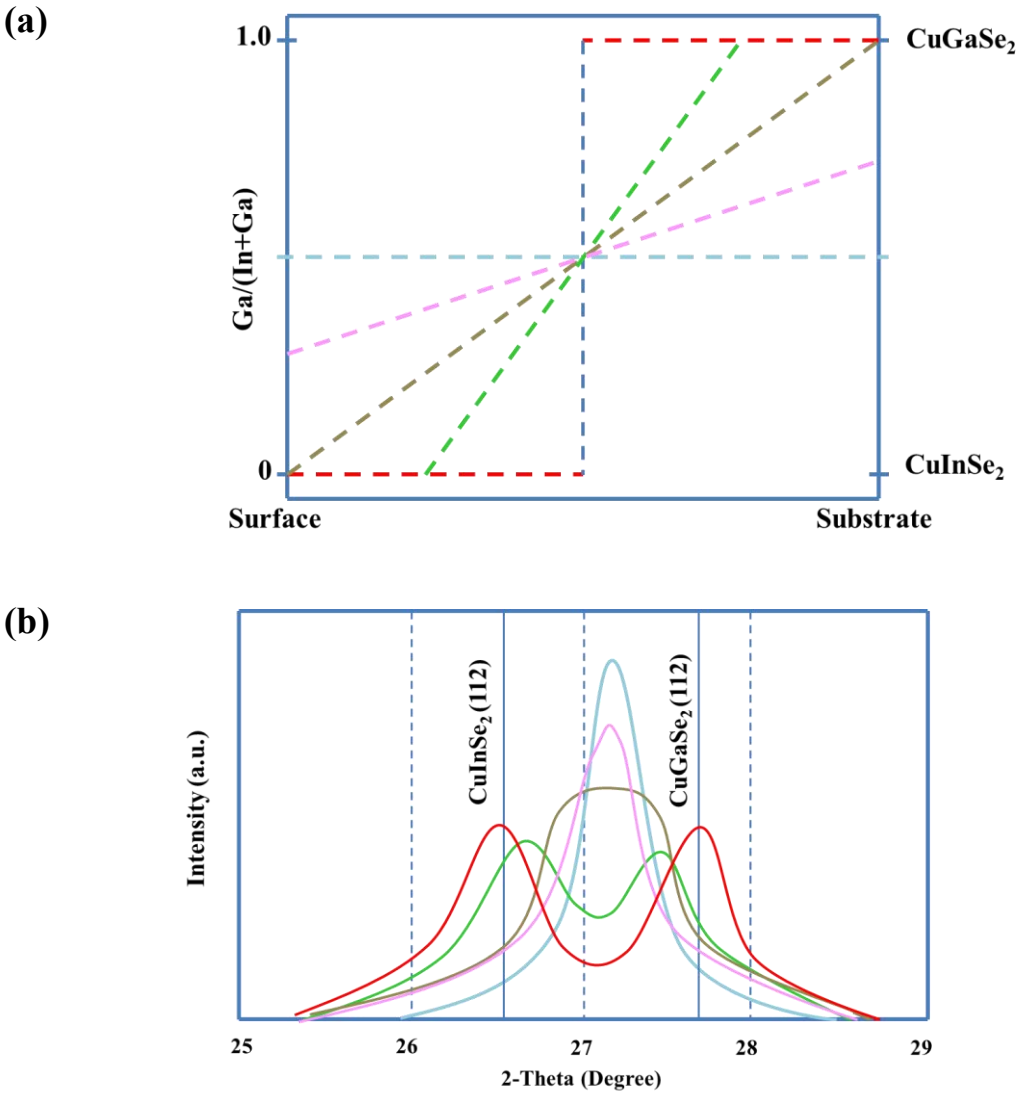

Figure 3.6: (a) The anticipated compositional depth profiles from the inter-diffusion of group-III elements in CIS/CGS bilayers. (b) The expected XRD patterns for (a) [35].

Chapter IV

Diffusion of Ga and In in $CuInSe_2$/$CuGaSe_2$ Bilayer Thin Films on SLG Substrates

The diffusion of Ga and In elements in bilayers of CIS and CGS thin films induces various alloying formation of $CuIn_{1-x}Ga_xSe_2$. The bilayers on the Mo/SLG substrates were analyzed in various aspects to obtain the key factors affecting the diffusion of Ga and In. At first, the standard CIS and CGS thin films were fabricated to indicate the XRD peak positions of CIS and CGS. Then for the bilayers on SLG substrates, the variation of growth substrate temperature as well as Cu-atomic ratios in the CIS and CGS layers by comparing with the alternating order of deposition, the active role of copper selenide (Cu-Se) phase during growth process of the bilayers were studied. Thereafter, the bilayer systems on Na blocking substrate (Mo/Al_2O_3/SLG) are presented and compared with the bilayers on the Mo/SLG.

4.1 $CuInSe_2$/$CuGaSe_2$ Bilayers on Mo/SLG Substrates

4.1.1 Standard CIS and CGS Thin Films

The CIS films were fabricated with both Cu-rich and Cu-poor compositions, whereas the CGS film layer was only stoichiometric composition. The substrate temperature during the deposition process was 550°C which was detected from surface radiation by pyrometer. The CGS and CIS films deposition times were 15 and 30 min, respectively. In the growth process, the thermal radiation detected by pyrometer and the output power of the temperature controller were recorded throughout the process.

Table 4.1: Atomic compositions of CIS and CGS films by EDS measurements.

Single layer	Cu (at.%)	In (at.%)	Ga (at.%)	Se (at.%)	Cu/(In+Ga)
CIS (Cu-rich)	29.43	22.36	-	48.21	1.31
CIS (Cu-poor)	24.34	25.77	-	49.89	0.94
CGS (Stoichiometry)	27.80	-	27.59	44.61	1.01

4.1.1.1 Bulk Compositional Analysis

The bulk composition of CIS and CGS thin films as measured by EDS to substantiate the Cu-atomic ratios of the as-grown films are listed in Table 4.1. The atomic ratios of Cu to group-III elements in the CIS single layer are both Cu-rich (y = 1.31) and Cu-poor (y = 0.94) and in the CGS single layer is stoichiometry (y = 1.01).

4.1.1.2 Surface Morphology

SEM images of the surface of Cu-rich CIS, Cu-poor CIS and stoichiometric CGS films are shown in Fig. 4.1. The CIS and the CGS films have a significant difference in grain size. The grains of CIS are significantly larger compared to those of the CGS. Within the CIS films, the Cu-rich film has a larger grain than its the Cu-poor counterpart. These results indicate that the difference of Cu content between two films could lead to different morphology.

4.1.1.3 Structural Analysis

The XRD patterns of the Cu-rich CIS, Cu-poor CIS and stoichiometric CGS films are shown in Fig. 4.2. Both CIS and CGS films reveal chalcopyrite phase with (112) preferred-orientation. The intensity of CGS is lower and broader than those of the CIS because of the thinner thickness and lower crystalline quality. The peak positions including the calculation of lattice constants and the average grain size by Scherrer formula are listed in Table 4.2. The average grain size calculated from the Scherrer formula is directly related to the FWHM of the peak which is inversely proportional to crystallite size given by

$$G = \frac{0.92\lambda}{FWHM\cos\theta} \qquad (4.1)$$

where λ is the wavelength of $Cu_{K\alpha 1}$ (1.5406 Å) and θ is the Bragg's angle in degree.

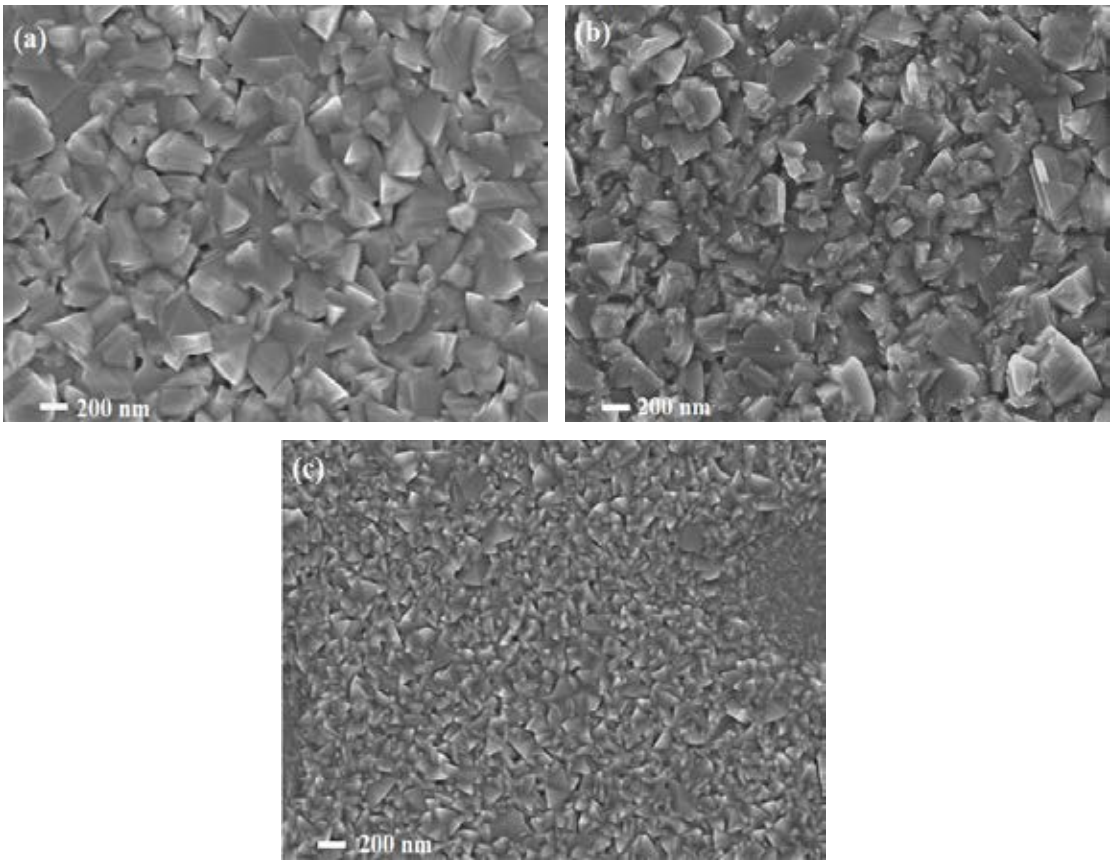

Figure 4.1: SEM images of (a) Cu-rich CIS film, (b) Cu-poor CIS film, and (c) stoichiometric CGS film at substrate temperature of 550 ℃.

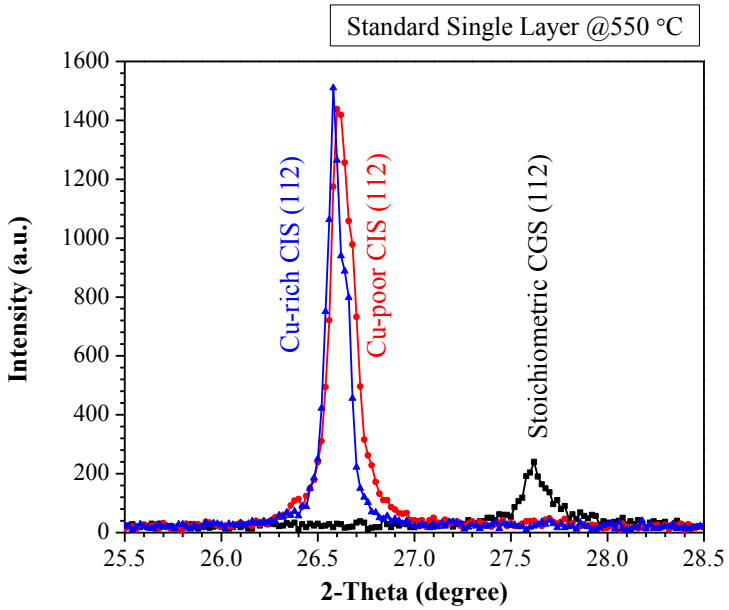

Figure 4.2: XRD patterns of Cu-rich and Cu-poor CIS films, including stoichiometric CGS film of (112) orientation.

Table 4.2: (112) peak position of the Cu-rich and Cu-poor CIS and the stoichiometric CGS films and calculation of lattice constants from XRD data

Single layer	(112) peak position (2θ)	Lattice constants (Å)		Grain size (nm)
		a	c	
Cu-rich CIS	26.58	5.79	11.67	153.51
Cu-poor CIS	26.60	5.78	11.68	98.92
Stoichiometric CGS	27.59	5.63	11.07	40.50

However, the calculations of crystallite size seem to be smaller than those observed from the SEM images since the SEM images show the lateral size over the small area, whereas the XRD averages over a larger volume of the sample. The calculations of grain size only show a trend compared with those seen in the SEM images. The larger grain size and higher crystalline quality is found in the Cu-rich CIS film due to the existence of Cu-Se secondary phase. It was discovered that Cu-Se phase played an important role in the grain growth by enhancing the mobility of adatoms on the substrate surface. On the other hand, the deficiency of Cu-Se in the Cu-poor CIS and the stoichiometric CGS with thin layer (~ 300 nm) results in the smaller grain size [36].

4.1.2 Effect of Substrate Temperature on Elements Diffusion

The CIS/CGS bilayers were fabricated by the sequential deposition of CGS and CIS, respectively. The total thickness for bilayers was about 1 μm and the value x = [Ga]/([Ga]+[In]) was set at ~ 0.4. Initially, the total deposition time was allowed for 45 minutes, the CGS and CIS layers were deposited for 15 and 30 min, respectively. Thus, the thickness ratio was 1:2. The growth substrate temperature was set at 400°C, 470°C and 550°C. The composition of the CIS film was varied for both Cu-rich and Cu-poor while the CGS layer was kept at stoichiometry. All as-grown bilayers were investigated for their crystallographic phase.

During the growth process of the bilayers, the inter-diffusion of Ga and In can occur and induce the formation of alloying $CuIn_{1-x}Ga_xSe_2$, i.e. Ga atoms from CGS can diffuse to the sites of In in CIS structure and vice versa. With the smaller atomic size of Ga than In, the size of CIS unit cell decreases and the size of CGS unit cell increases during the alloying process as indicated by the shift of the XRD peaks. In

order to analyze the inter-diffusion of Ga and In, the shifts from standard patterns of CIS and CGS films are considered qualitatively to observe how much the bilayers have intermixed at different growth conditions. The XRD patterns of all bilayers at different growth substrate temperatures are shown in Fig. 4.3

(a)

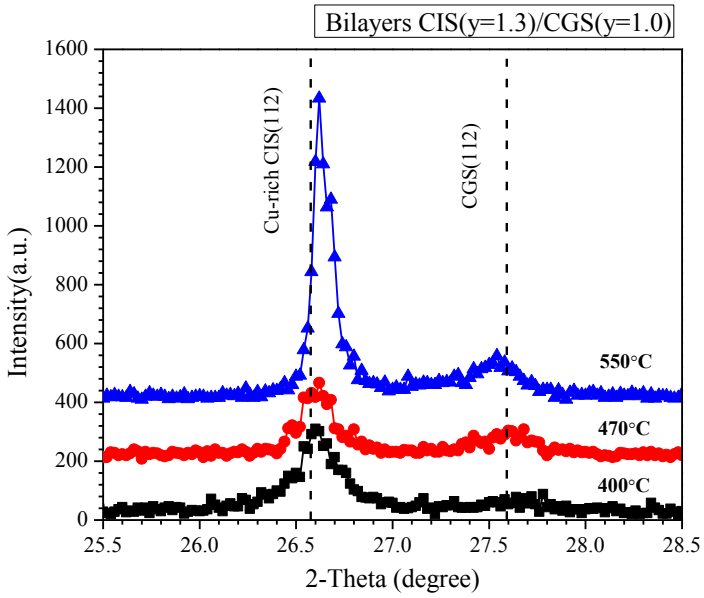

(b)

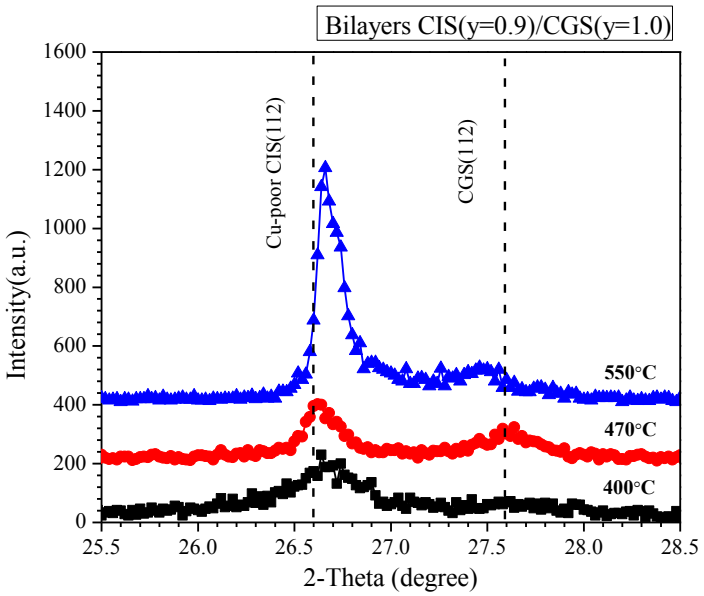

Figure 4.3: XRD patterns of bilayers at substrate temperature 400℃, 470℃ and 550℃; (a) bilayer CIS(y=1.3)/CGS(y=1.0) and (b) bilayer CIS (y=0.9)/CGS(y=1.0).

Table 4.3: XRD (112) peak position of CIS/CGS bilayers and shifting of lattice constants from their corresponding single layer.

Bilayer	(112) position (2θ)	(2θ) Shifting	Lattice constants (Å)			
			a	Δa	c	Δc
CIS(y=1.3)/CGS(y=1.0)						
Cu-rich CIS	26.62	0.04	5.77	-0.02	11.68	+0.01
Stoichiometric CGS	27.54	0.05	5.65	+0.02	11.06	-0.01
CIS(y=0.9)/CGS(y=1.0)						
Cu-poor CIS	26.65	0.05	5.76	-0.02	11.68	+0.00
Stoichiometric CGS	27.41	0.18	5.67	+0.04	11.11	+0.04

The higher intensity of (112) preferred-orientation was observed at higher substrate temperature, since the higher substrate temperature enhances the grain growth by increasing surface diffusion of depositing atoms. Additionally, the intensity of Cu-rich CIS in bilayer is higher than Cu-poor CIS in bilayer at higher substrate temperature corresponding to the film quality and larger grain sizes of the Cu-rich film. By analyzing the peak shift of the bilayers, it is more pronounced that the CIS and CGS are a little bit shifted from the standard CIS and CGS films at the substrate temperature of 550°C. However, the results only show the trend of Ga and In inter-diffusion when the growth substrate temperature is increasing.

4.1.3 $CuInSe_2/CuGaSe_2$ and $CuGaSe_2/CuInSe_2$ Bilayers

From the previous section, it is known that higher substrate temperature results in the peak shift of CIS and CGS. This section, I only consider the behavior of diffusion in the growth at high substrate temperature. The depositions sequences of CIS/CGS and vice versa were controlled for a total thickness of 1 μm in 40 minutes. The CGS and CIS layers were deposited for 16 and 24 minutes, respectively, to achieve the thickness ratio of CGS:CIS approximately 2:3. The substrate temperature was kept at 600°C (not to exceed the softening point of the SLG substrate). In each bilayer, the layer of CIS and CGS were fabricated in both Cu-rich and Cu-poor compositions. During the growth process, the substrate temperature, the substrate heater output power (OP%) and temperature of the film surface (T_{pyro}) were monitored and recorded simultaneously. After the bilayer deposition, the substrate was cooled

down slowly in order to maintain the sample with Se vapor pressure. When finished, the as-grown films were investigated for their crystallographic phase, cross-sectional morphology and EDS trace depth profiles. The experimental details are stated in the next subsection.

4.1.3.1 Cu-rich CIS/ Cu-rich CGS & Cu-rich CGS/Cu-rich CIS

The Cu-rich in both layers of CIS and CGS were grown by setting y ~ 1.2 throughout the deposition process. The growth of CIS/CGS was begun with Cu, Ga and Se co-evaporation for the thickness of 400 nm and then the Cu, In and Se were deposited on top of CGS immediately for thickness of 600 nm and vice versa. The signals from the pyrometer and the OP% of the substrate temperature controller are depicted in Fig. 4.4. The black line is the pyrometer signal of CIS/CGS, while the red line is for CGS/CIS. The signals of T_{pyro} starts from the reading temperature at the front surface of the substrate (Mo/SLG) about 600°C, then the signal shows the oscillations that occur from the interference of reflection of the thermal radiation between back and front surfaces of the growing films. The OP% is increasing because the $Cu_{2-x}Se$ phase of Cu-rich film has a higher emissivity that emits the heat radiation of the substrate, leading to a lowering of the substrate temperature [37].

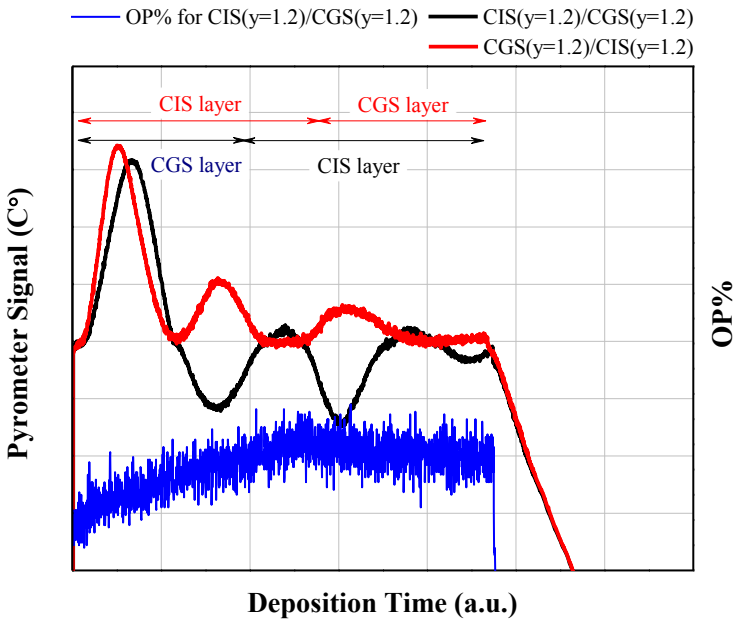

Figure 4.4: The temperature profiles T_{pyro} and substrate heater output power (OP%) of Cu-rich bilayers.

In addition, it can be seen in the first part of deposition that the distance between oscillation loops in the CIS layer (red line) is less than the distance in the CGS oscillation loops (black line) which is the result of the different refractive index of CIS and CGS films. It was shown elsewhere that the refractive index (n) of the $CuIn_{1-x},Ga_xSe_2$ thin film decreases with increasing Ga content, i.e. $n_{CGS} < n_{CIS}$ [38].

The cross-sectional images showing grain size for CIS(y=1.2)/CGS(y=1.2) and CGS(y=1.2)/CIS(y=1.2) are shown in Fig 4.5(a) and 4.6(a), respectively. It is obviously seen in both images that all Cu-rich bilayers have relatively large grain size. The XRD patterns of both CIS/CGS and CGS/CIS bilayers are shown in Fig 4.5(a) and 4.6(a). The inter-diffusion behavior of Ga and In in CIS/CGS and CGS/CIS is significantly different. For the CIS/CGS bilayer, the peaks of CIS and CGS merge together showing a single broadening peak. This result indicates that the inter-diffusion of Ga and In occurs during the deposition of the CIS which results in the formation of alloying CIGS. For the CGS/CIS bilayer, the two separated peaks of CIS and CGS are clearly seen, i.e. less the inter-diffusion of Ga and In. Although, the Cu-Se secondary phase can enhances the elements inter-diffusion, the CIS on a bottom layer seems difficult for In out-diffusion and Ga in-diffusion. The EDS trace depth profiles of atomic percentage in the bilayers are shown in Fig. 4.7(a) and 4.8(a) supporting the XRD results. In the case of CIS/CGS, the distribution of Ga and In atoms are almost uniform. The data shows the overlap of the group-III elements in the region of CGS layer and up into the lower region of CIS. In contrast for CGS/CIS, the distribution of In atoms decreases from the bottom to the surface. In other words, the distribution of Ga atoms decreases from the surface to the bottom layer as shown in Fig. 4.8(a).

There are some discrepancies in the CIS/CGS and CGS/CIS bilayers. Two assumptions that may affect the inter-diffusion of Ga and In are (1) the effect from the thermal gradient in the growing film, (2) the time for Ga diffusion of 16 minutes of the CGS deposition on top of the CIS layer is less than the time for In diffusion into 24 minutes of CIS on CGS layer.

To verify the first assumption, the thickness of CIS as a bottom layer was reduced to 400 nm for CGS/CIS bilayer. In the opposite way, the thickness of CGS as a bottom layer was increased to 600 nm. The resulting XRD patterns are compared, as shown in Fig. 4.9. Even if the thickness of CIS is decreased, the XRD pattern still exhibits the double peaks with almost equal intensity (red line). For the increasing thickness of CGS, the pattern shows the broadening of merging CIS and CGS peaks to form the alloying of CIGS at $x \sim 0.6$ (black line). From these results, the peak shift of CIS and CGS is not influenced by the thickness of the layers, i.e. the thermal gradient is not the major impact for the elements diffusion in these bilayers.

For the second assumption, the time for depositing CGS upper layer on CIS (CGS/CIS) was increased from 16 to 24 minutes, but the thickness was kept at 400 nm. Meanwhile, the deposition time of CIS as the upper layer for CIS/CGS was reduced from 24 to 16 minutes with the thickness of 600 nm. The results are shown in Fig. 4.10. Despite the increased time for Ga and In inter-diffusion in CGS/CIS bilayer, the result still exhibits the double peaks with just higher intensity (red line).

As a result, the inter-diffusion of Ga and In in CGS/CIS is less than that in the CIS/CGS. By considering the phase diagram of CIS and CGS, it is shown that the structure formation for higher quality of CIS film is easier than that of CGS at 600°C (also the grain size of CIS is larger than the CGS). It is harder to alter the stable CIS structure by the inter-diffusion of Ga and In in CGS/CIS structure.

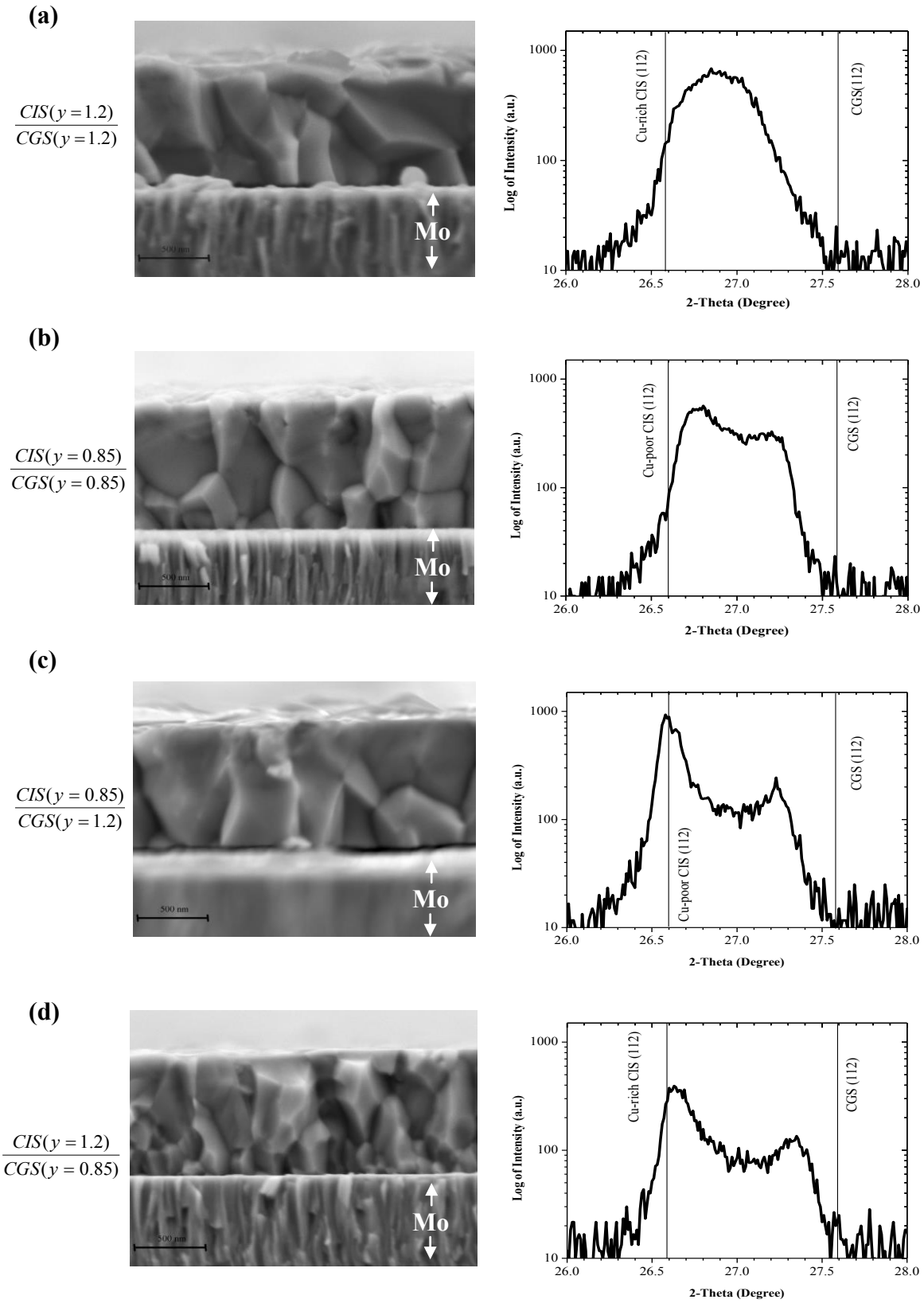

Figure 4.5: SEM cross-section images and XRD patterns of (112) CIS/CGS bilayers.

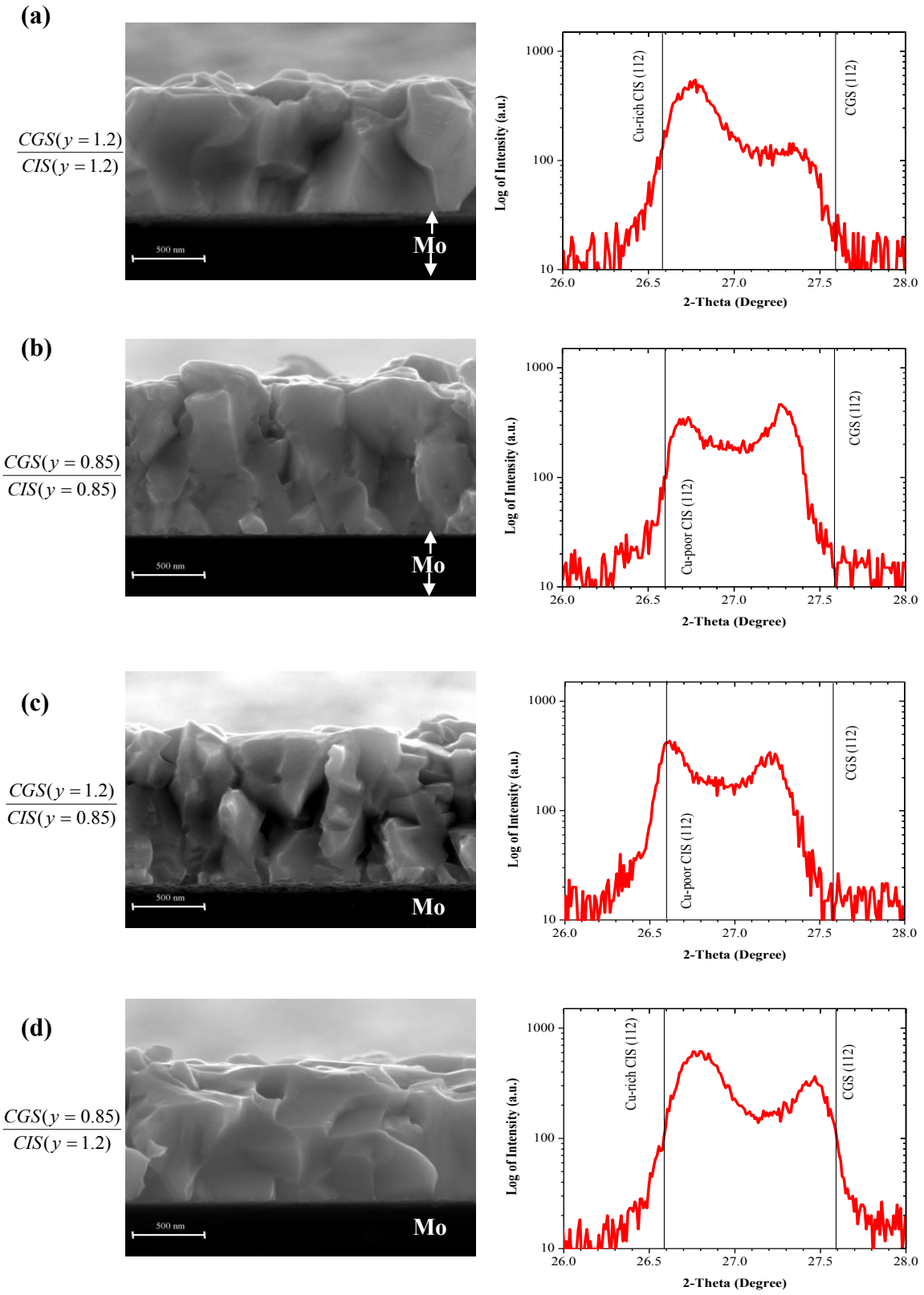

Figure 4.6: SEM cross-section images and XRD patterns of (112) CGS/CIS bilayers.

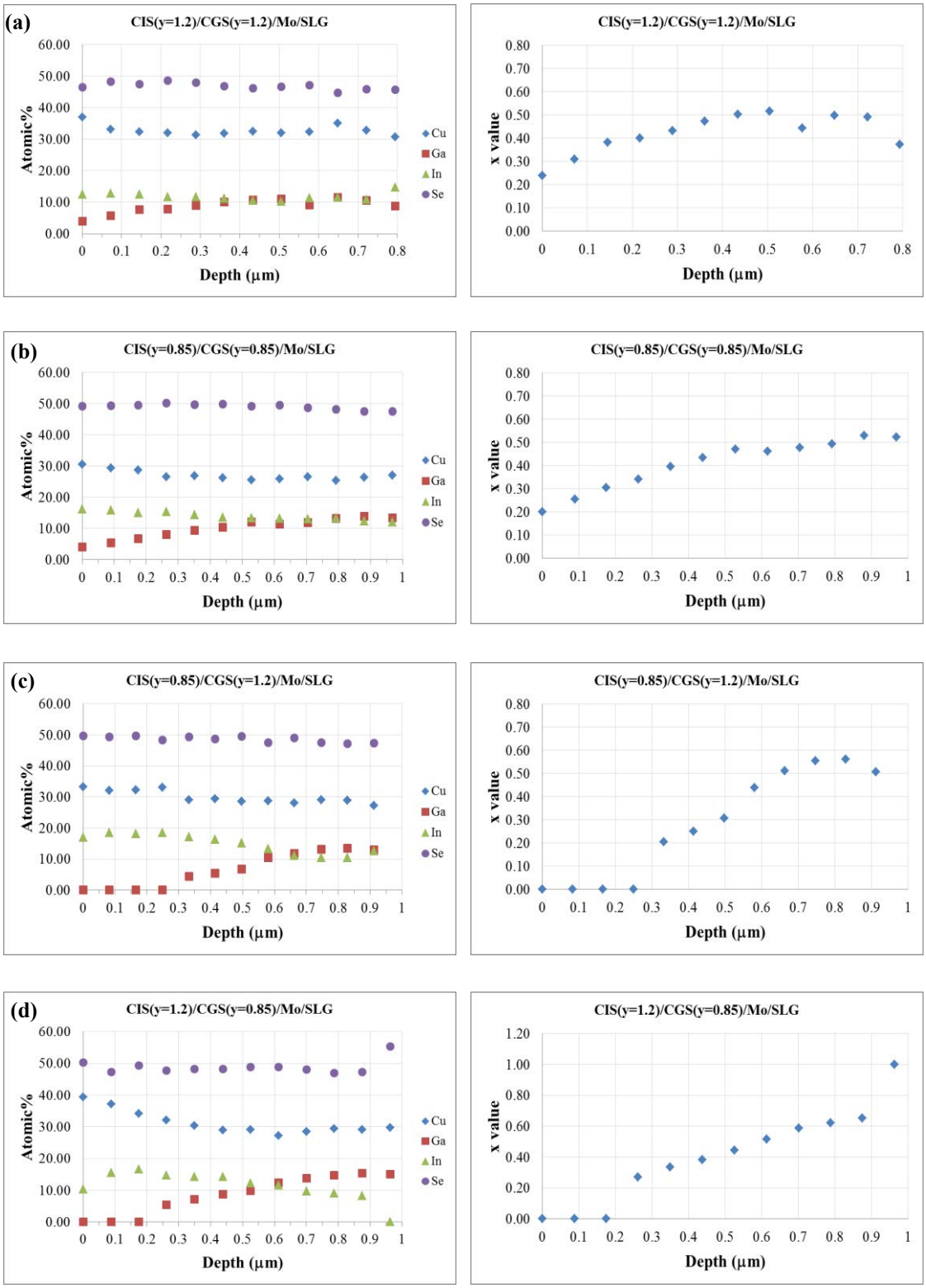

Figure 4.7: EDS trace depth profiles and x values ([Ga]/([Ga]+[In])) for CIS/CGS bilayers.

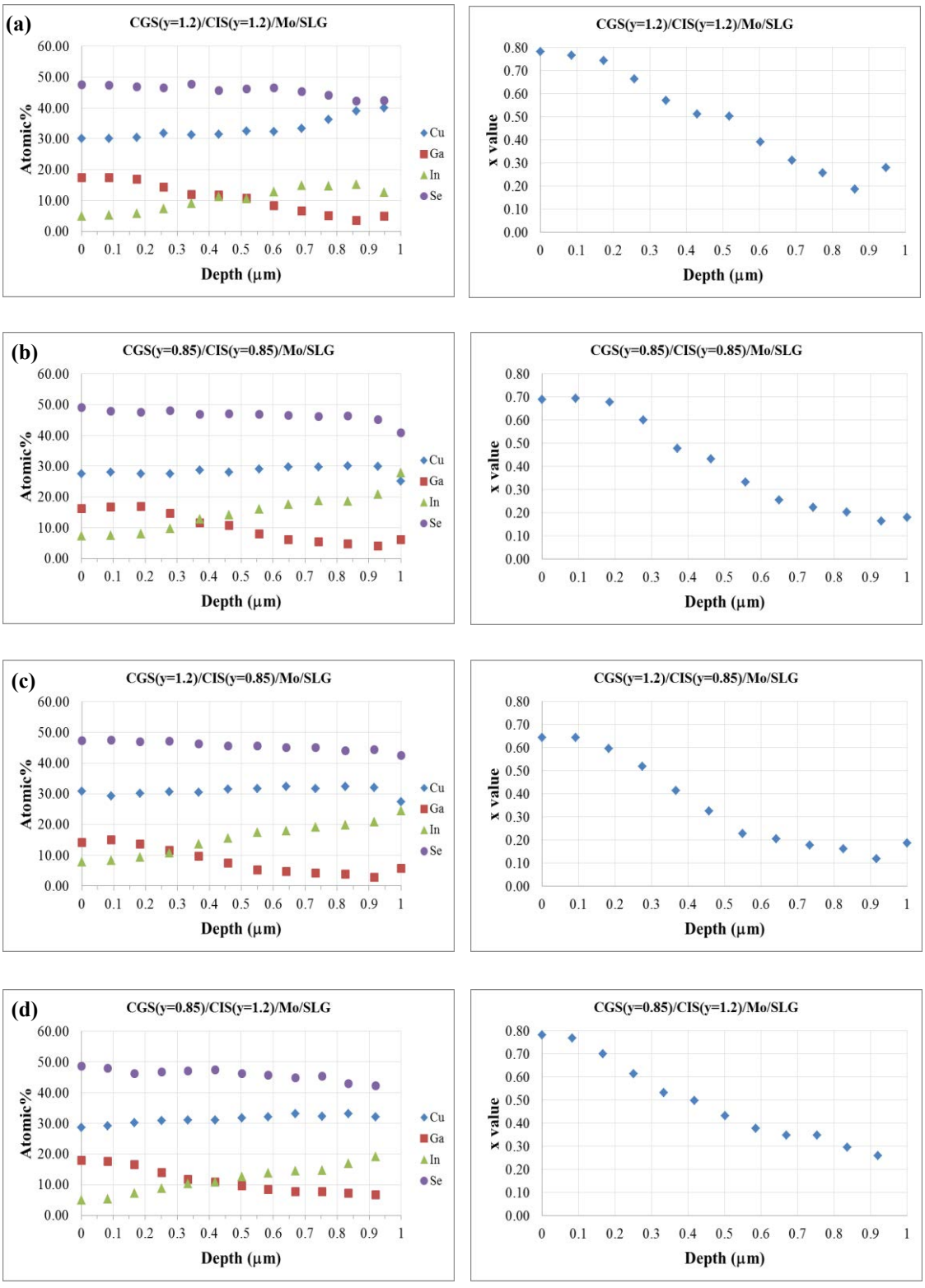

Figure 4.8: EDS trace depth profiles and x values ([Ga]/([Ga]+[In])) for CGS/CIS bilayers.

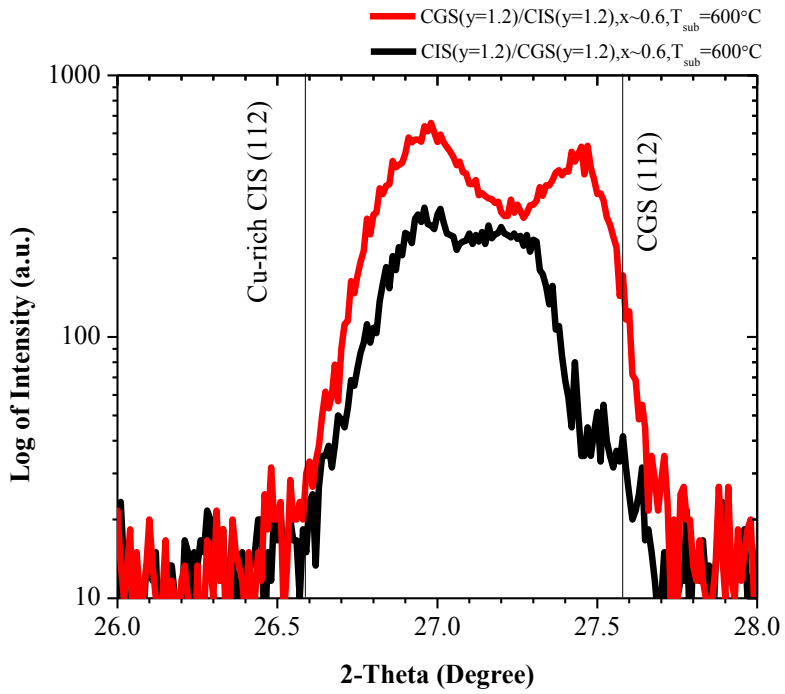

Figure 4.9: XRD patterns of (112) CGS/CIS (red line) and (112) CIS/CGS (black line) with x_{cal} ~ 0.6.

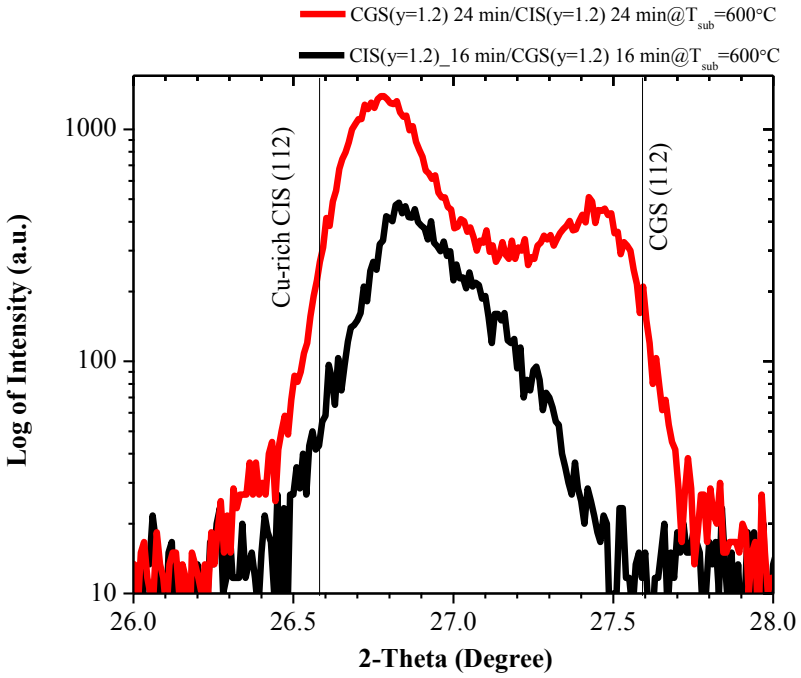

Figure 4.10: XRD patterns of (112) CGS/CIS (red line) with increasing the time for CGS layer and (112) CIS/CGS (black line) with reducing the time for CIS layer.

Table 4.4: XRD (112) peak position of CIS/CGS bilayers and shifting of lattice constants from their corresponding single layer.

Bilayer	(112) Peak position (2θ)	2θ Shifting
CIS(y=1.2)/CGS(y=1.2)		
Cu-rich CIS	Broadening peak	-
Cu-rich CGS	Broadening peak	-
CIS(y=0.85)/CGS(y=0.85)		
Cu-poor CIS	26.72	+0.12
Cu-poor CGS	27.21	-0.38
CIS(y=0.85)/CGS(y=1.2)		
Cu-poor CIS	26.60	+0.00
Cu-rich CGS	27.24	-0.35
CIS(y=1.2)/CGS(y=0.85)		
Cu-rich CIS	26.62	+0.04
Cu-poor CGS	27.34	-0.25

Table 4.5: XRD (112) peak position of CGS/CIS bilayers and shifting of lattice constants from their corresponding single layer.

Bilayer	(112) Peak position (2θ)	2θ Shifting
CGS(y=1.2)/CIS(y=1.2)		
Cu-rich CIS	26.71	+0.13
Cu-rich CGS	27.35	-0.24
CGS(y=0.85)/CIS(y=0.85)		
Cu-poor CIS	26.62	+0.02
Cu-poor CGS	27.24	-0.35
CGS(y=1.2)/CIS(y=0.85)		
Cu-poor CIS	26.60	+0.00
Cu-rich CGS	27.20	-0.39
CGS(y=0.85)/CIS(y=1.2)		
Cu-rich CIS	26.69	+0.11
Cu-poor CGS	27.41	-0.18

4.1.3.2 Cu-poor CIS/Cu-poor CGS & Cu-poor CGS/Cu-poor CIS

The experimental procedures were the same as the Cu-rich bilayer films. However, the layers of CIS and CGS were grown by setting y ~ 0.85 throughout the deposition process. The thermal radiations read by pyrometer and OP% for the substrate were recorded during growth process as shown in Fig. 4.11. For 40 minutes duration of the deposition, the number of interference fringes is greater than those in Cu-rich bilayers indicating that the thickness of the Cu-poor films is thicker than the Cu-rich films. It is worth to note that all the bilayers in this work were kept with the constant value of Cu thickness (d_{Cu}). The Cu-rich and Cu-poor compositions refer to the changing in rate of Ga and In atoms compared with the number of Cu atoms. Generally, the Cu-rich films always loss the Cu atoms to form the $Cu_{2-x}Se$, then the thickness of film will be reduced.

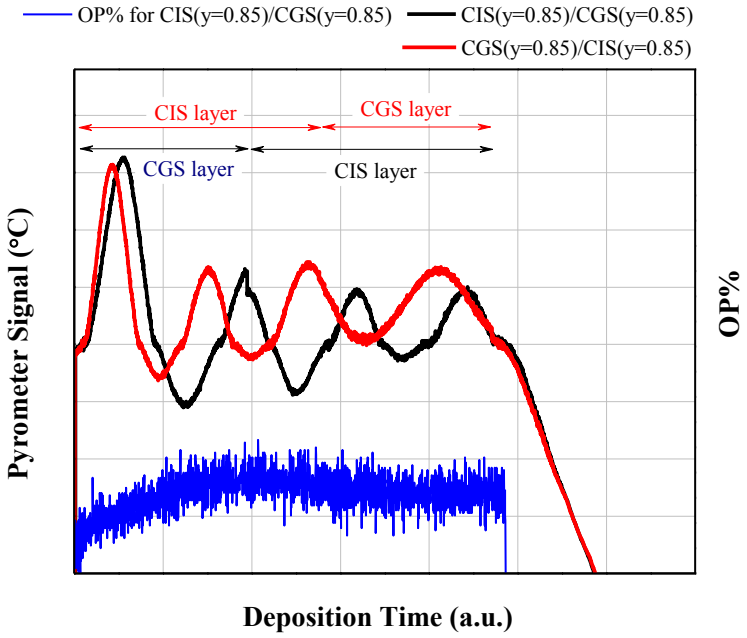

Figure 4.11: The temperature profiles T_{pyro} and substrate heater output power (OP%) of Cu-poor bilayers.

The SEM cross-section images of these bilayers (see Fig. 4.5(b) and 4.6(b)) show the two-layer structure of CIS and CGS layers, especially in CIS/CGS film because of the smaller grain size of CGS than CIS. The corresponding XRD patterns plotted in Fig. 4.5(b) and 4.6(b) show that the inter-diffusion behavior is almost similar in both bilayers. These results show less inter-diffusion when compared with the Cu-rich bilayers. From the EDS depth profiles in Fig. 4.7(b) and Fig. 4.8(b), the result of the CIS/CGS is quite similar to the Cu-rich bilayer, but the distribution of Ga and In in the CGS/CIS bilayer is less than the first one.

4.1.3.3 Cu-poor CIS/Cu-rich CGS & Cu-rich CGS/Cu-poor CIS

For the growth process of CIS(y=0.85)/CGS(y=1.2) bilayer, the composition of CGS as the bottom layer was set with y ~ 1.2 for 16 minutes of deposition, and followed by CIS as the upper layer with y ~ 0.85 for 24 minutes of deposition, and so was the deposition for CGS(y=1.2)/CIS(y=0.85) bilayer. The pyrometer signals and substrate heater output power recorded during the growth process as shown in Fig. 4.12. In the early stage of growing Cu-rich CGS layer, it can be observed that the output power is increasing until obtaining y ~ 1.2. When the Cu-poor CIS layer is grown on top of CGS, the OP% is decreased and then stabilized until the end of deposition of bilayer.

The grain size of CIS(y=0.85)/CGS(y=1.2) from SEM images, as shown in Fig. 4.5(c) is quite large, but totally different from CGS(y=1.2)/CIS(y=0.85), as shown in Fig. 4.6(c). As mentioned, the bottom layer strongly affects the growth of the top layer. In addition, the Cu-rich CGS has the $Cu_{2-x}Se$ that strongly supports the grain growth at high temperature. The XRD patterns are not significantly different between those bilayers despite the different in the grain size. The XRD patterns show the seperated peaks of CIS and CGS, and the diffusion of In is not as much as the Cu-rich and the Cu-poor bilayers. The distribution of Ga and In atoms from EDS measurement (see Fig. 4.7(c) and 4.8(c)) shows the combination of elements for few hundred nanometers.

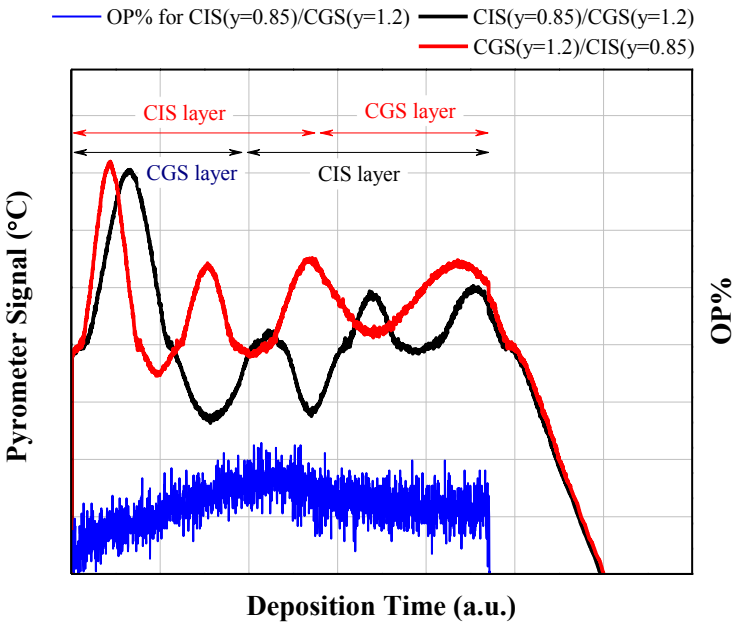

Figure 4.12: The temperature profiles T_{pyro} and substrate heater output power (OP%) of Cu-poor CIS/Cu-rich CGS and Cu-rich CGS/Cu-poor CIS bilayer.

4.1.3.4 Cu-rich CIS/Cu-poor CGS & Cu-poor CGS/Cu-rich CIS

For the growth process of CIS(y=1.2)/CGS(y=0.85), the CGS was deposited with y ~ 0.85 for 16 minutes, and followed by the CIS layer with y ~ 1.2 for 24 minutes, as shown in Fig. 4.13 (black line) while the red line is for the CGS (y=0.85)/CIS (y=1.2) bilayer.

The SEM cross-sectional images are distinguishable between the two samples (see Fig. 4.5(d) and Fig. 4.6(d)). The CIS(y=1.2)/CGS(y=0.85) shows separated CIS and CGS layers, whereas the CGS(y=0.85)/CIS(y=1.2) shows the homogeneous grain of the bilayer because of $Cu_{2-x}Se$ from the bottom layer. The XRD patterns are somewhat similar. However, the peak shift of CIS and CGS in both bilayers shows some differences. The inter-diffusion of group-III elements in these bilayers are less than from the other bilayer films (see Fig. 4.7(d) and 4.8(d)).

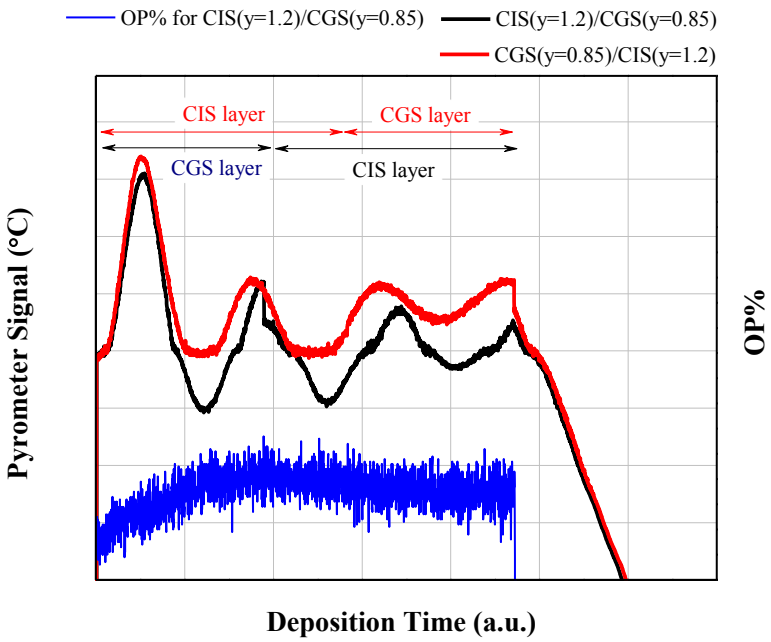

Figure 4.13: The temperature profiles T_{pyro} and substrate heater output power (OP%) of Cu-rich CIS/Cu-poor CGS and Cu-poor CGS/Cu-rich CIS bilayer.

4.1.4 Evidence of More Ga Diffusion

The simple experiment to show that Ga atoms diffuse easier than In atoms was performed; (i) the layer of Cu-rich CIS was fabricated, and followed only Ga and Se (GaSe/CIS) to convert the excess $Cu_{2-x}Se$ phase in the Cu-rich CIS to the stoichiometric CIGS, where the CGS layer was much thinner than the CIS layer. For comparison, (ii) the layer of Cu-rich CGS was fabricated, and followed only by In and Se (InSe/CGS) to convert the excess $Cu_{2-x}Se$ in the Cu-rich CGS to the stoichiometric CIGS film, where the CIS layer was thinner than the CGS layer. The XRD results are shown in Fig. 4.14(a) and 4.14(b). The XRD patterns show more shift of CGS peak than the CIS peak in the GaSe/CIS, indicating more Ga out-diffuse from the CGS crystalline structure and some In atoms can replace the Ga sites. The higher intensity peak of alloying CIGS is observed in the GaSe/CIS than in the InSe/CGS. The results suggest that Ga can diffuse into the CIS structure better than In can diffuse into the CGS structure. This is consistent with the diffusion coefficients of In (1.5×10^{-11} cm^2/sec) and Ga (4.0×10^{-11} cm^2/sec) found from the CIS/CGS grown by sputtering method at 650°C [39].

(a)

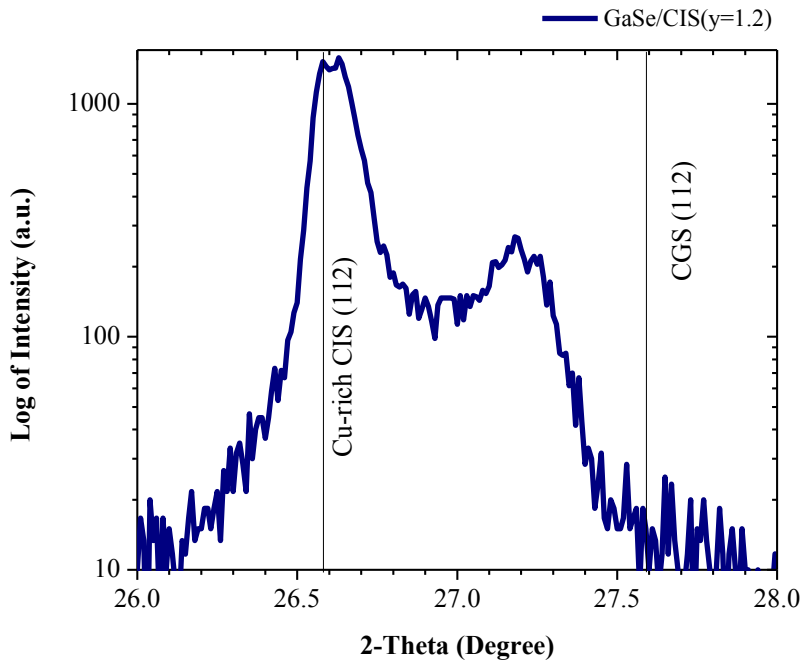

(b)

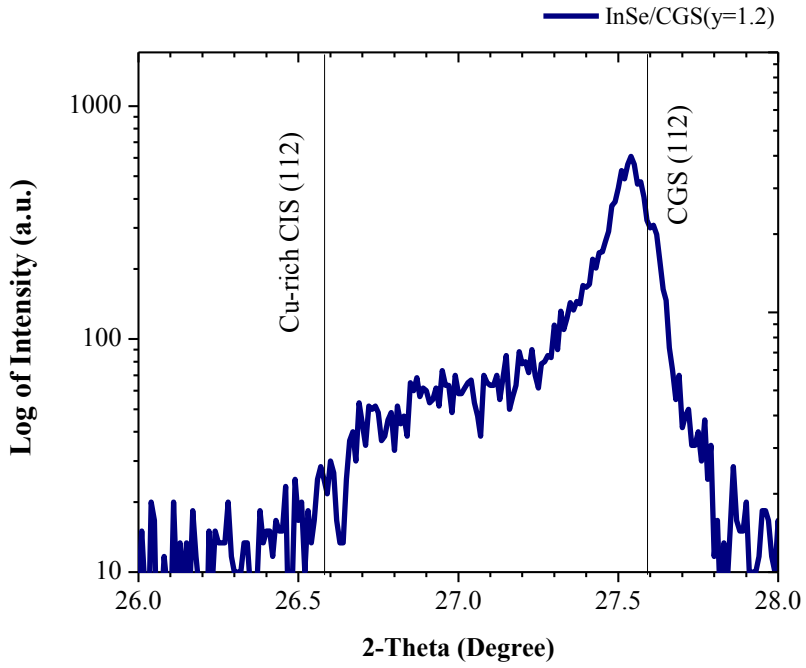

Figure 4.14: (a) The XRD (112) pattern for Ga-Se on CIS precursor (GaSe/CIS). (b) The XRD (112) pattern for In-Se on CGS precursor layer (InSe/CGS).

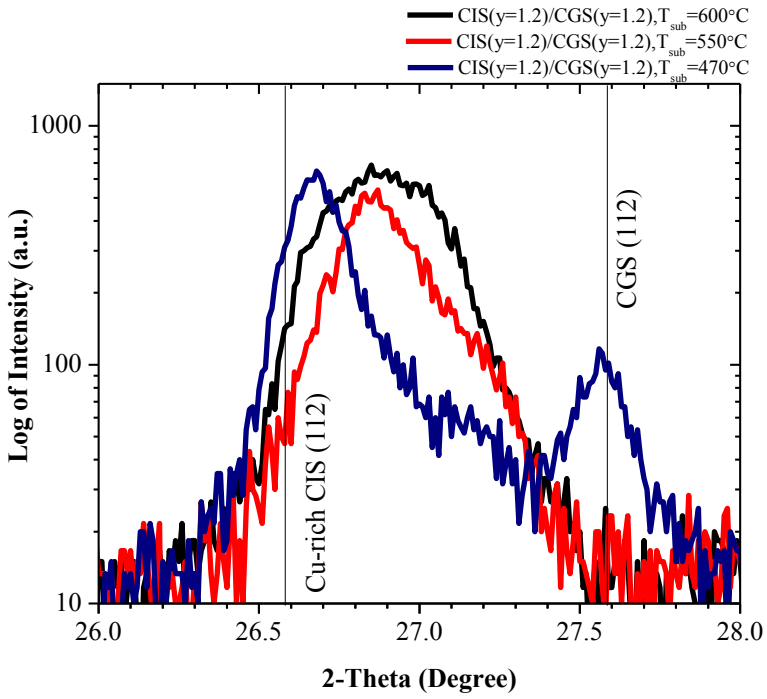

Figure 4.15: XRD (112) patterns of Cu-rich bilayers at substrate temperature 470℃, 550℃ and 600℃.

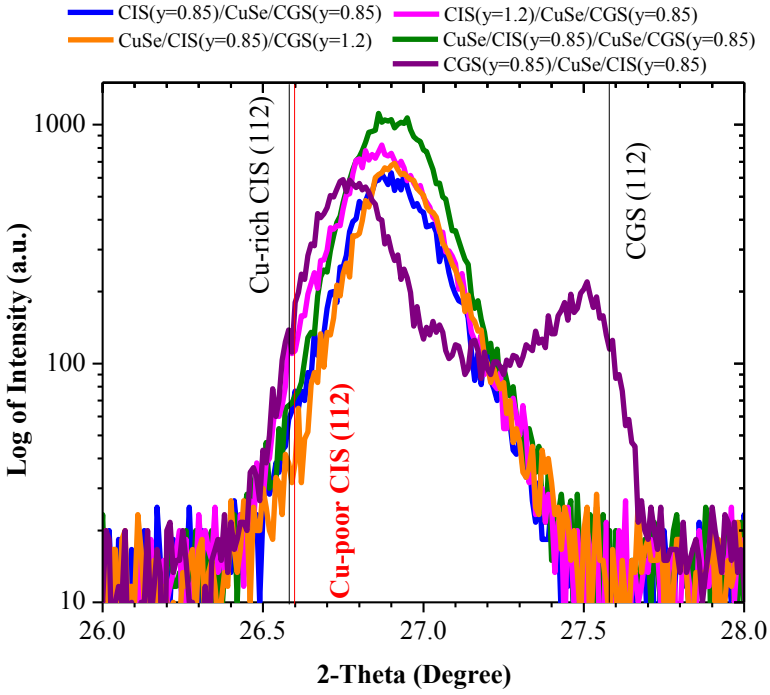

Figure 4.16: The XRD (112) patterns of CGS and CIS bilayers with Cu-Se sandwiched layer.

4.1.5 Roles of Cu-Se on Ga and In Inter-diffusion

In this part, the influence of the binary compound, Cu-Se, that enhances the Ga and In inter-diffusion of CIS/CGS bilayer thin films is studied. The effect of substrate temperature during growth on the working of Cu-Se for the elemental diffusion and the effect of Cu-Se inserting layer between CIS and CGS layers are considered.

4.1.5.1 The Effect of Substrate Temperature

Generally, the phase of Cu-Se is closely related to the growth temperature. Figure 4.15 shows the XRD patterns of Cu-rich CIS/CGS bilayers at different substrate temperatures; 470°C, 550°C and 600°C. The XRD patterns show the differences in the crystal structure. The bilayer grown at 470°C reveals the separated peaks of CIS and CGS. For higher growth substrate temperatures, the results show the broadening coalescence of the peaks. The bilayers grown below 600°C have a trend to have less Ga and In inter-diffusion, indicating by poorer quality of crystallographic structure. From the phase diagram of Cu-Se system, the phase of Cu-Se depends on the temperature and weight percent of Cu and Se atoms. The $Cu_{2-x}Se$ is present above 523°C that is believed to affect the elemental diffusion.

4.1.5.2 The Bilayers of CIS and CGS with Cu-Se Inserting Layer

From the results shown in Fig 4.5 (b), (c), (d), the question arises what would system happen when the Cu-Se is added between the Cu-poor bilayers? Instead of directly growing the Cu-rich layer, Cu and Se atoms were added in between the Cu-poor CIS or CGS layers to obtain the total Cu-atomic composition y ~ 1.2 with the substrate temperature at 600°C. The resulting XRD patterns are shown in Fig. 4.16 for CIS(y=0.85)/CuSe/CGS(y=0.85) (blue), CIS(y=1.2)/CuSe/CGS(y=0.85) (pink), CuSe/CIS(y=0.85)/CGS(y=1.2) (orange) and CuSe/CIS(y=0.85)/CuSe/CGS(y=0.85) (green). The results show the phase of alloying CIGS diffraction patterns at x ~ 0.4 without separation of peaks seen in bilayer structures. These experiments indicate that the inter-diffusion of Ga and In strongly depends on the presence of Cu-Se compound which enhances higher elemental mobility. For comparison, the alternated layers of CIS and CGS with the Cu-Se inserted between the Cu-poor CIS and CGS layers (CGS(y=0.85)/CuSe/CIS(0.85)) was fabricated. The result obviously shows the

bilayer structure pattern (purple). In this case, Cu-Se compound does not affect the Cu-poor CIS starting layer. It only filled the structure by reducing the defects such as Cu vacancies. As previously mentioned, the CIS crystalline formation is easier than the CGS formation within the temperature range of interest (600°C for this research). In atoms are difficult to diffuse out from the structure and also Ga atoms cannot diffuse into the sites of In atoms. The formation alloying of CIGS only occurred in some region at interface between layers.

4.2 CIS/CGS and CGS/CIS Bilayers on Al_2O_3/SLG Substrate

For the $CuIn_{1-x}Ga_xSe_2$ solar cells, Na in the SLG substrate about 0.1wt.% can enhance the cell performances, by reducing the donor type defects (In_{Cu} or Ga_{Cu}) [40]. The incorporation about 0.1 wt.% of Na into the CIGS material can induce Na on either copper sites (Na_{Cu}) or group-III sites (Na_{Ga}, Na_{In}) [41]. Because the diffusion of the elements can be proceeded by the vacant lattice sites, then the effect of Na from the SLG could be one of the key factors for the diffusion of Ga in bilayer systems. This section focuses on the effect of Na on the diffusion of Ga in both of CIS/CGS and CGS/CIS bilayers.

4.2.1 Experimental Details

The fabrication of CIS/CGS bilayers and CGS/CIS bilayers on Mo/Al_2O_3/SLG was the same as those on Mo/SLG. The growth substrate temperature was kept at 600°C throughout the process. The CIS and CGS layers were varied for Cu-rich and Cu-poor compositions. The output power (OP%) obtained from substrate heater and the pyrometer signals were recorded during the growth process. The signals are almost similar to those from the bilayers on Mo/SLG.

4.2.2 Comparison of Bilayers on SLG and Al_2O_3/SLG Substrates

4.2.2.1 CIS/CGS Bilayers

In the Cu-rich CIS/Cu-rich CGS bilayer, the SEM cross-sectional image without Na containing is shown in Fig. 4.17(a). By determining the grain boundary, the film without Na seems to have a relatively larger grain size. The XRD pattern of

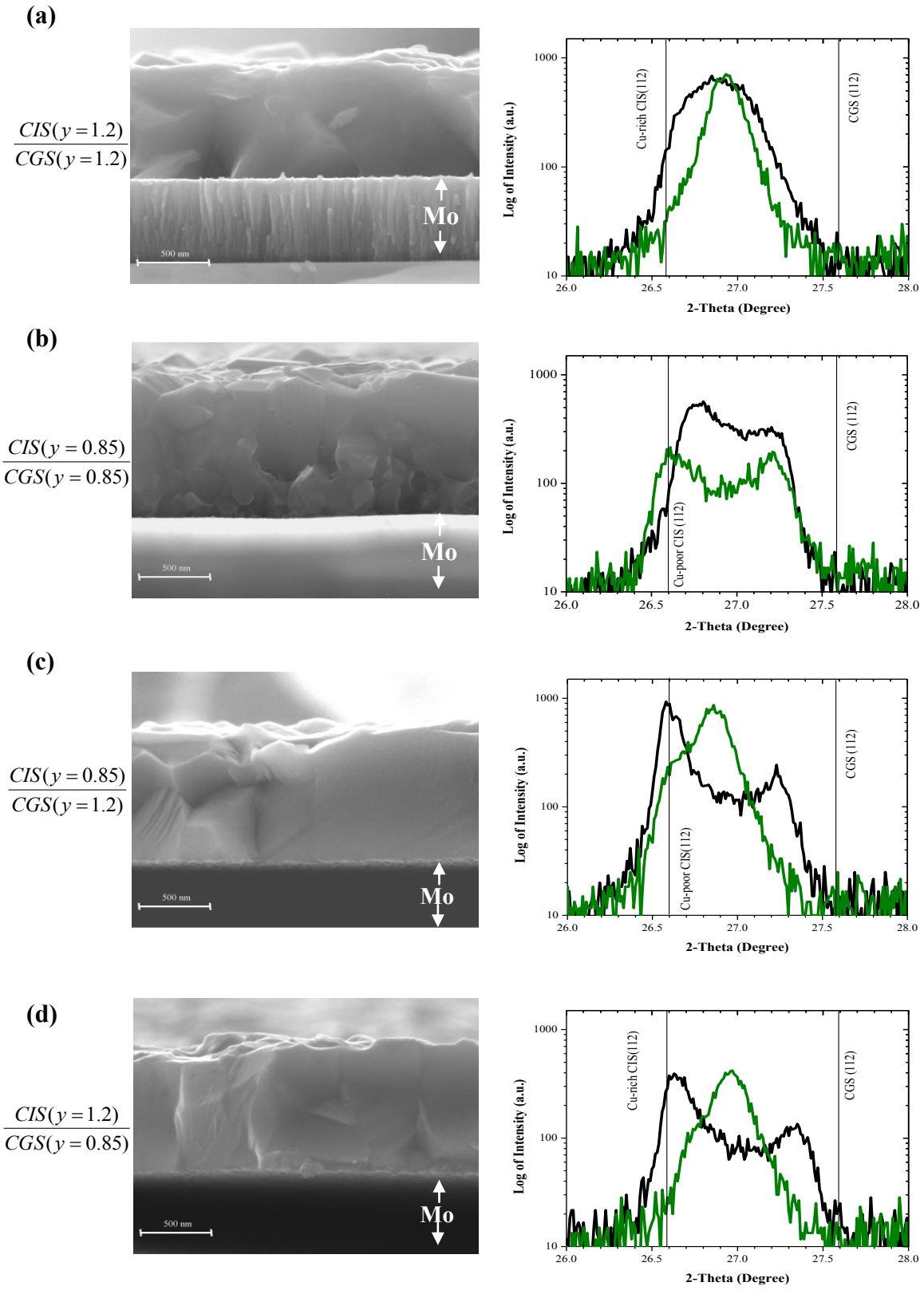

Figure 4.17: SEM cross-section images and XRD patterns of (112) CIS/CGS bilayers on Al_2O_3/SLG (green line) by comparison with bilayers on SLG (black line).

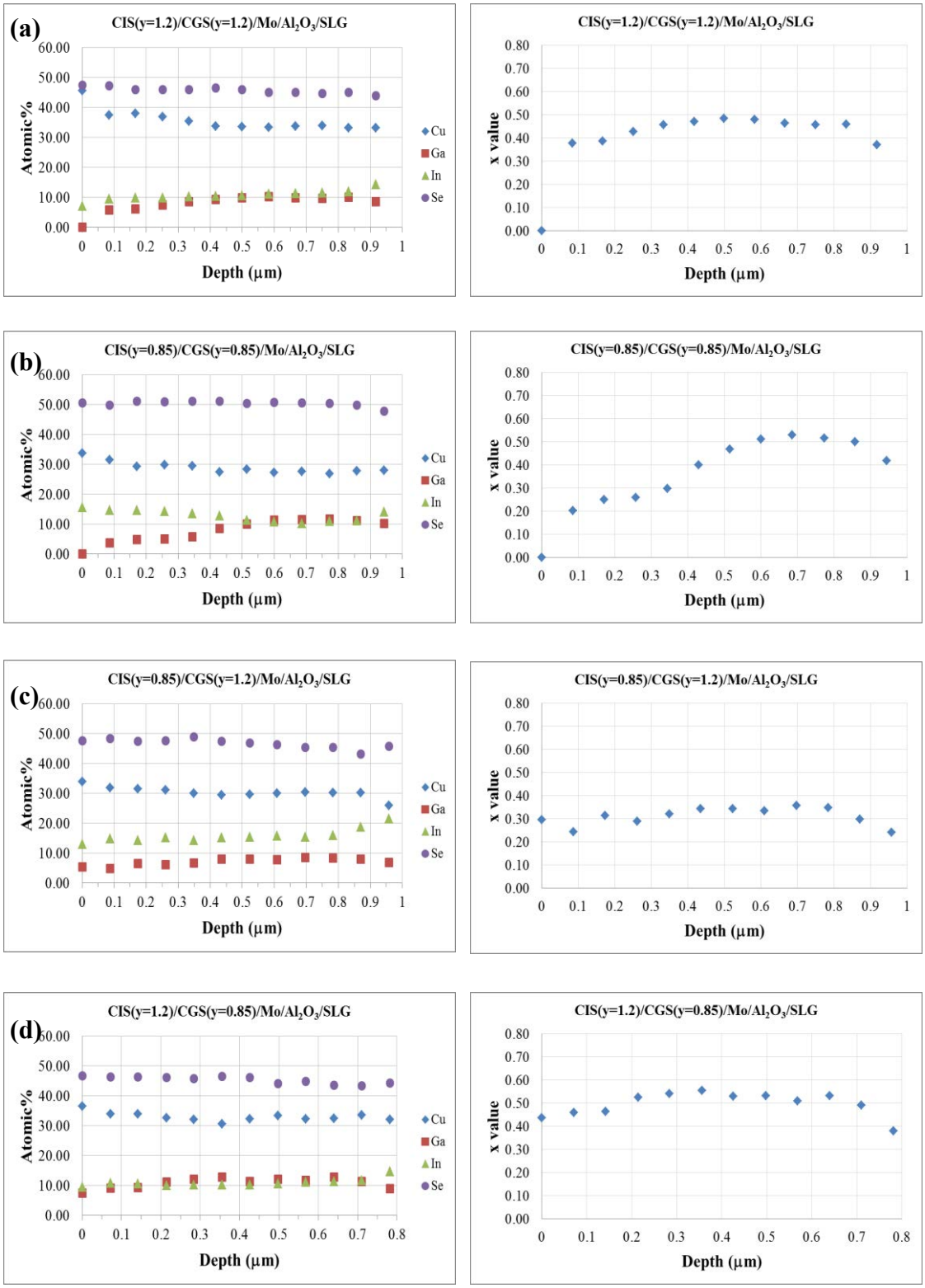

Figure 4.18: EDS trace depth profiles and x values ([Ga]/([Ga]+[In])) for CIS/CGS bilayers on Al_2O_3/SLG.

the Cu-rich bilayers without Na in Fig. 4.17(a) shows a well coalescence pattern of homogeneous CIGS film with x ~ 0.4 – 0.5, not the separated bilayer structure. The pattern does not show the broadening shape like that seen in the bilayer with Na (black line in Fig. 4.17(a)). This indicates that the inter-diffusion of Ga and In is quite uniform throughout the film. The EDS trace depth profiles of Na free film in Fig. 4.18(a) shows that the trend of atomic% distribution is qualitatively the same as the Cu-rich bilayer with Na film (see Fig. 4.7(a)).

For the Cu-poor CIS/CGS bilayer, the SEM image of the sample without Na (see Fig 4.17(b)) shows smaller grain in the region of bottom layer than the bilayer with Na seen in Fig. 4.5(b). The bilayers with Na also exhibit the shaper shapes and dense grains of the (112) direction of the crystal growth. This result is supported by the XRD pattern (Fig. 4.17(b) with black line) which the quality of film is higher in the bilayer with Na. K. Granath *et al.*'s work on the influence of Na on the CIGS films concluded that the internal Na from the SLG substrate and the incorporation of Na via NaF compound enhanced the smooth surface of the CIGS film and also the grain growth [42]. In Na free bilayer, the XRD pattern is almost similar to that of the bilayer with Na, however, the XRD intensity is lower than that with Na indicating lower quality of crystal growth for the Cu-poor bilayer without Na. The EDS data of the bilayers with Na (see Fig. 4.7(b)) is almost similar to the bilayer without Na (Fig. 4.18(b)) but the distribution of Ga and In is less in the region near the top layer, i.e. stronger Ga grading.

For the Cu-poor CIS/Cu-rich CGS bilayer, the SEM image of the Na free bilayer in Fig. 4.17(c) shows larger grains than the bilayer with Na. The XRD pattern demonstrates the better alloying CIGS pattern where some of CIS layer is still visible. The EDS trace depth profile in Fig. 4.18(c) shows a relatively uniform distribution of group-III elements throughout the bilayer.

For the Cu-rich CIS/Cu-poor CGS bilayer, the SEM cross-sectional image of the Na free bilayer shown in Fig. 4.17(d) also shows the larger grains than the bilayer with Na. The XRD pattern also indicates the alloying CIGS film where the Ga and In inter-diffusion is higher than the bilayer with Na. The trend of group-III elements in Fig. 4.18(d) has relatively uniform distribution.

4.2.2.2 CGS/CIS Bilayers

By comparison, the grains of CGS/CIS bilayers with and without Na shown in Fig. 4.6 and Fig. 4.19, respectively, are qualitatively similar. However, in the Cu-poor bilayer without Na, the grains become smaller, especially near the bottom region. By considering the XRD results all of the CGS/CIS bilayers without Na shown in Fig. 4.19 (orange lines), the patterns are similar to the bilayers of CGS/CIS with Na (red lines in Fig. 4.19). This suggest that the inter-diffusion of Ga and In in the CGS/CIS bilayers may not be from the influence of Na. For the Cu-poor CGS/CIS bilayers with and without Na, the inter-diffusion of Ga and In are similar, i.e. Ga and In can diffuse via Cu vacancy defects. Additionally, Na also has an effect on the grain growth as seen in the Cu-poor bilayers without Na by considering from the lower quality of (112) preferred-orientation from the XRD patterns that looks similar to the Na free CIS/CGS bilayer. The EDS trace depth profiles shown in Fig. 4.20 give the trend of atomic distribution like in the CGS/CIS bilayer with Na (Fig. 4.8).

4.3 Discussion

The results obtained from the bilayers on the SLG substrates suggest that the high diffusivity of Ga and also In is enhanced by the presence of copper selenide phase in CIS/CGS bilayer. Copper selenide phase is believed to help increasing the surface mobility of the elements because of its quasi-liquid phase at the higher temperature (exceeding 523°C by the phase diagram). Most of the bilayers deposited with Cu-rich composition at high substrate temperature show larger grains. However, the presence of copper selenide phase has less effect on the inter-diffusion of Ga and In in the Cu-rich CGS/Cu-rich CIS bilayer despite the large grain size obtained. The grain boundaries do not affect the elements diffusion in the bilayer structure as suggested by Lundberg *et al* [19]. Naturally, when the melting point of the material is high, so is the formation energy for the compound. The melting point of CGS is higher than the CIS, thus the stable structure of CGS is more difficult to form than the CIS. At 600°C, the structure of CIS is relatively stable, and thus difficult for the elements to out-diffusion. Only the defects inside the structure can be allowed. By this reason, the inter-diffusion of group-III elements is difficult when the CIS as the bottom layer has completed its structure. However, for the Cu-poor CGS/Cu-poor CIS

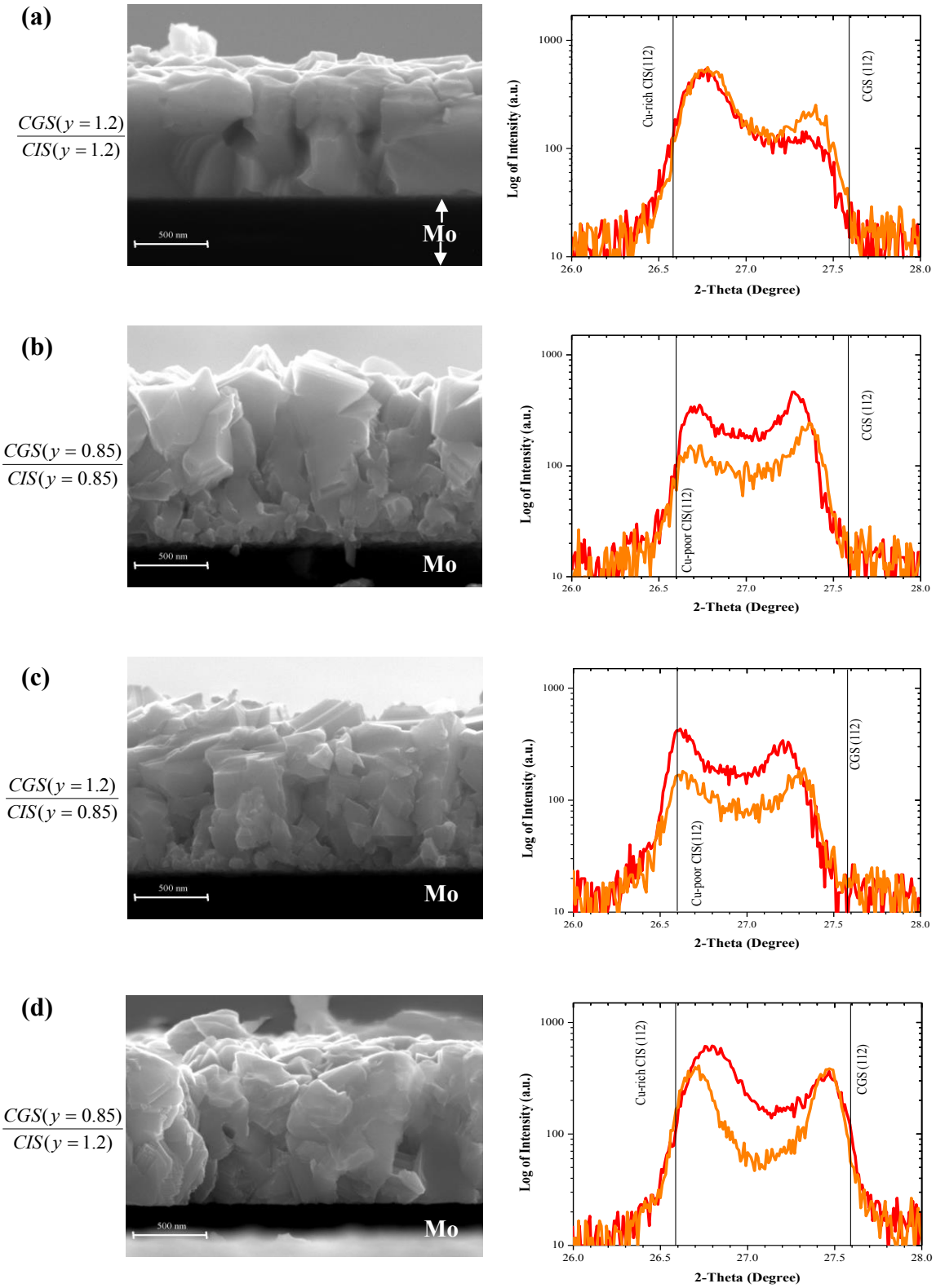

Figure 4.19: SEM cross-section images and XRD patterns of (112) CGS/CIS bilayers on Al_2O_3/SLG (orange line) by comparison with bilayers on SLG (red line).

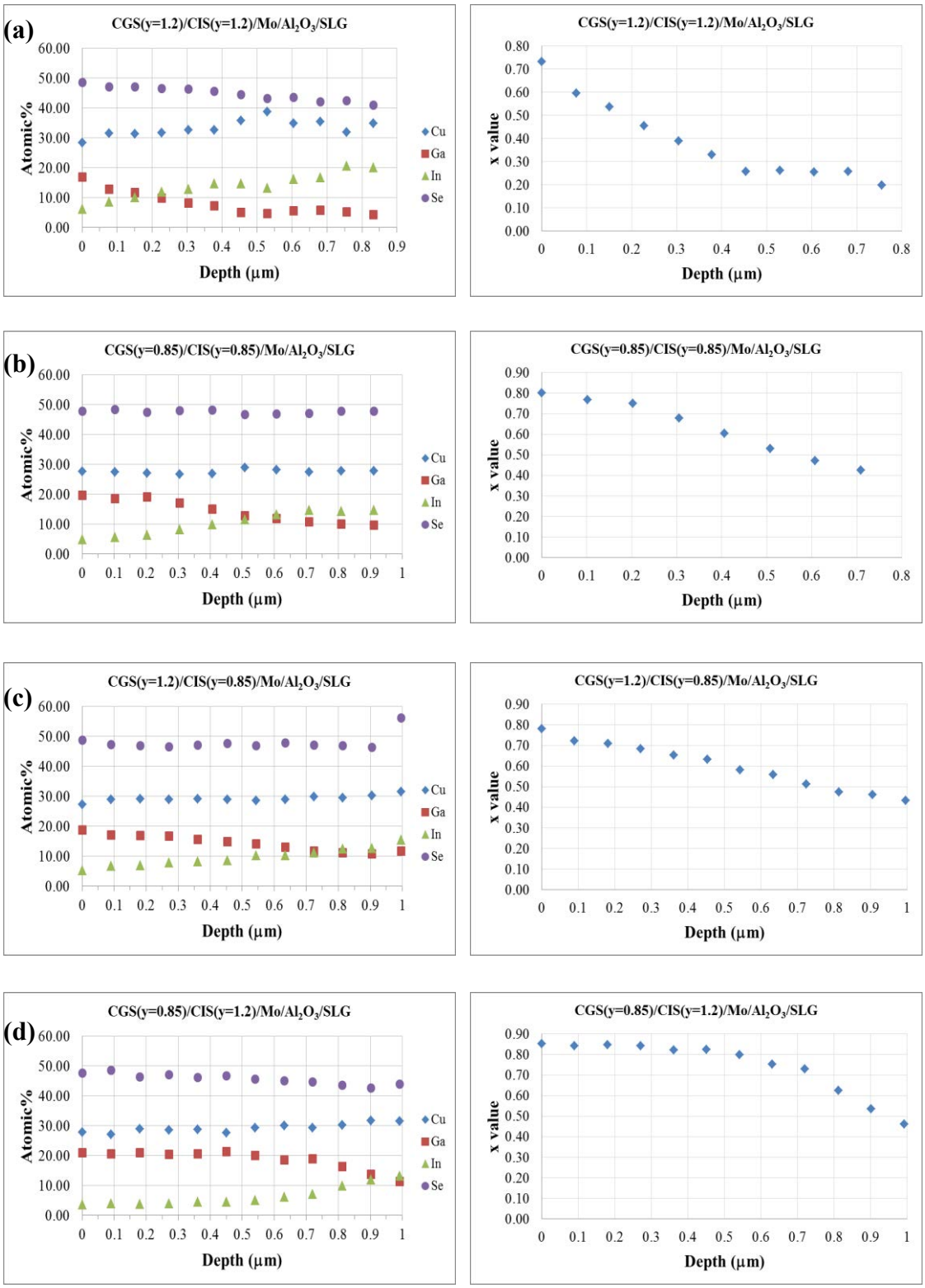

Figure 4.20: EDS trace depth profiles and x values ([Ga]/([Ga]+[In])) for CGS/CIS bilayers on Al_2O_3/SLG

Table 4.6: XRD (112) peak position and shifting of CIS/CGS bilayers on Al_2O_3/SLG.

Bilayer	(112) Peak position (2θ)	2θ Shifting
CIS(y=1.2)/CGS(y=1.2)	26.96	-
CIS(y=0.85)/CGS(y=0.85)		
Cu-poor CIS	26.60	+0.00
Cu-poor CGS	27.20	-0.39
CIS(y=0.85)/CGS(y=1.2)		
Cu-poor CIS	26.60	+0.00
Cu-rich CGS	26.88	-0.71
CIS(y=1.2)/CGS(y=0.85)		
Cu-rich CIS	26.80	+0.22
Cu-poor CGS	27.02	-0.57

Table 4.7: XRD (112) peak position and shifting of CGS/CIS bilayers on Al_2O_3/SLG.

Bilayer	(112) Peak position (2θ)	2θ Shifting
CIS(y=1.2)/CIS(y=1.2)		
Cu-rich CIS	26.72	+0.14
Cu-rich CGS	27.29	-0.30
CIS(y=0.85)/CIS(y=0.85)		
Cu-poor CIS	26.66	+0.06
Cu-poor CGS	27.36	-0.23
CGS(y=1.2)/CIS(y=0.85)		
Cu-poor CIS	26.61	+0.01
Cu-rich CGS	27.30	-0.29
CIS(y=0.85)/CIS(y=1.2)		
Cu-rich CIS	26.71	+0.13
Cu-poor CGS	27.45	-0.14

bilayer, the inter-diffusion is induced by vacancy defects inside the structure. For other CGS/CIS bilayers, a small number of In atoms may out-diffuse from the CIS structure into the CGS structure seen by the peak shift of CIS and CGS. By considering the SEM surface morphology of standard single layer CIS and CGS, it is possible that the large grain size and dense film of CIS as a bottom layer (CGS/CIS) is difficult for Ga atom diffuse into, opposite from the CIS/CGS where In atoms are easily to diffuse into the CGS bottom layer because of the smaller grain size and relatively looser grains of the CGS.

In section 4.1.4, Ga atoms are shown to be more favorable for the out-diffusion from the CGS structure, then In atoms can be drawn into the CGS structure forming the CIGS. As the result, the peak of CGS is shifted toward CIGS, whereas the Ga atoms are hardly diffuse into the CIS structure, thus the peak of CIS remains at its position.

Aside from the copper selenide phase and relatively less-stable structure of CGS that affect the inter-diffusion of Ga and In atoms, the elements diffusion is also achieved by the vacancy defects in the crystal structure describing the results of the Cu-poor bilayers. The Cu-poor composition induces the occurrence of Cu vacancy defects (V_{Cu}) and also the group-III antisite defects (In_{Cu} and Ga_{Cu}) [5] whereas the Cu-rich bilayer films have Ga and In vacancy defects, where Ga and In atoms can proceed in the diffusion in bilayers. This was verified by the experiment on the Ga diffusion in bilayers deposited on the Na blocking layer (Al_2O_3/SLG). It has been known that Na atoms could out-diffuse from the SLG substrate into the CIGS film during the growth process. Na could seize the sites of Cu, Ga and In. The inter-diffusion of group-III elements was then hindered by Na. From the XRD results, the bilayers of CIS/CGS deposited on the Na blocking substrates show the relatively better alloying of CIGS, especially in Cu-rich bilayers. The Ga and also In prefer the group-III sites than the Cu vacancy sites which agree with the work done by Shroeder *et al.* for the Ga diffusion in CIS epitaxial layer [18]. For the alternated bilayers, i.e. CGS/CIS without Na, the inter-diffusion is not significantly different from the CGS/CIS bilayers with Na even if the lower crystalline quality from XRD is observed. Moreover, the grains observed in the SEM cross-sectional image is smaller than that

of the Cu-poor films. It indicates that the diffusion occurs in the Cu-poor bilayer film via the Cu vacancies.

In addition to the XRD results, the EDS trace depth profiles confirm the inter-diffusion of Ga and In. The bilayers that have the uniformity of Ga and In distribution throughout the film, the EDS data show no variation for the value of x. Those can be seen in Na free bilayers CIS/CGS. For the bilayers that have less of Ga and In inter-diffusion, i.e. Cu-poor CIS/Cu-rich CGS and Cu-rich CIS/Cu-poor CGS show the near zero value of x in the CIS region as seen in Fig. 4.7(c) and Fig.4.7(d). This indicates the grading of Ga through the thickness of the bilayers.

4.4 Summary

The polycrystalline CIS/CGS and CGS/CIS bilayers were fabricated with varied Cu-atomic ratio, e.g. Cu-rich and Cu-poor compositions in each layer on the substrates with Na (SLG) and without Na (Al_2O_3/SLG). The XRD is the main tool used to observe the peak shift of CIS and CGS related to the diffusion of Ga and In in the bilayers. In this work, the substrate temperature was kept at 600°C. In the CIS/CGS bilayers with Na, Cu-rich and Cu-poor bilayer films have a higher Ga and In inter-diffusion, especially in Cu-rich bilayer film because of the existing Cu-Se compound. With the smaller atomic size of Ga than In and also the less-stability of CGS structure, Ga is then easier to diffuse than In. Ga and In atoms are able to diffuse to either Cu or group-III vacancies. In the CIS/CGS bilayers without Na, the inter-diffusion is better than that with Na because Ga and In atoms prefer the group-III vacancies than the Cu vacancies. In the case of Cu-poor CIS/Cu-poor CGS bilayers with and without Na, the group-III diffusion occurs similarly because of Cu vacancies in the structure. The XRD together with EDS depth profiles can be used to indicate the uniform diffusion and the grading of group-III elements in the CIS/CGS and CGS/CIS bilayer systems.

Chapter V

Diffusion of Ga and In in $CuInSe_2$/$CuGaSe_2$ Epitaxial Bilayer Thin Films on GaAs(001) Substrates

The type of crystal structure is one of the important factors for the elemental diffusion. The diffusivity of the elements in polycrystalline structure and single crystalline can be different. In this chapter, I try to point out similarity and dissimilarity of the diffusion of Ga and In in the epitaxial CIS/CGS bilayers on GaAs substrate from its polycrystalline counterparts. The chapter starts with the details of standard epitaxial layer of CIS, CGS and CIGS in order to indicate the peak positions of CIS, CGS and CIGS epitaxial thin films on GaAs (001) substrates. The XRD results of the CIS/CGS as well as CGS/CIS epitaxial bilayers with varying Cu-atomic composition are presented.

5.1 Standard Epitaxial CIS, CGS and CIGS Films

The epitaxial CIS, CGS and CIGS films were grown on GaAs(001) substrates where the compositions of CIS and CGS were both Cu-rich (y = 1.2) and Cu-poor (y = 0.85), whereas the CIGS was fabricated with slightly Cu-rich composition (y ~ 1.1) and x ~ 0.4. The thickness of CIS and CGS films was set at 600 nm for 60 minutes of deposition time and the CIGS film was grown for 1 μm thick during 100 minutes deposition period. The substrate temperature during the deposition process was kept at 600°C. During the growth process, the pyrometer signals and the output power of the temperature controller for substrate were recorded until the end of growth process as shown in Fig. 5.1 for Cu-rich CIS and CGS epitaxial films. RHEED was employed to verify the epitaxial growth. The RHEED patterns of the Cu-rich CIS and CGS films shown in Fig. 5.2 exhibit streaky patterns for the smooth surface of Cu-rich epitaxial films. The standard as-grown films were analyzed with SEM to observe surface morphology, and also with XRD for their crystallographic phase, as illustrate in Fig 5.3.

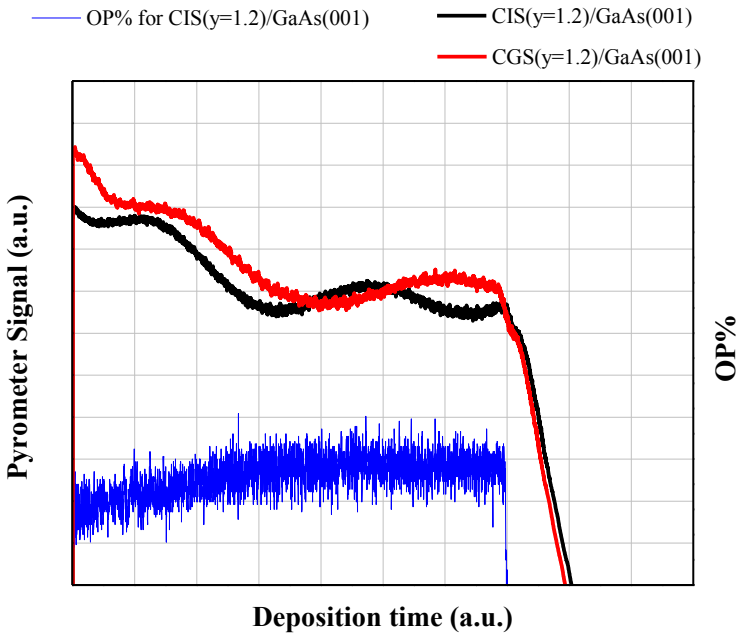

Figure 5.1: The temperature profiles T_{pyro} and substrate heater output power (OP%) of Cu-rich CIS and CGS epitaxial films.

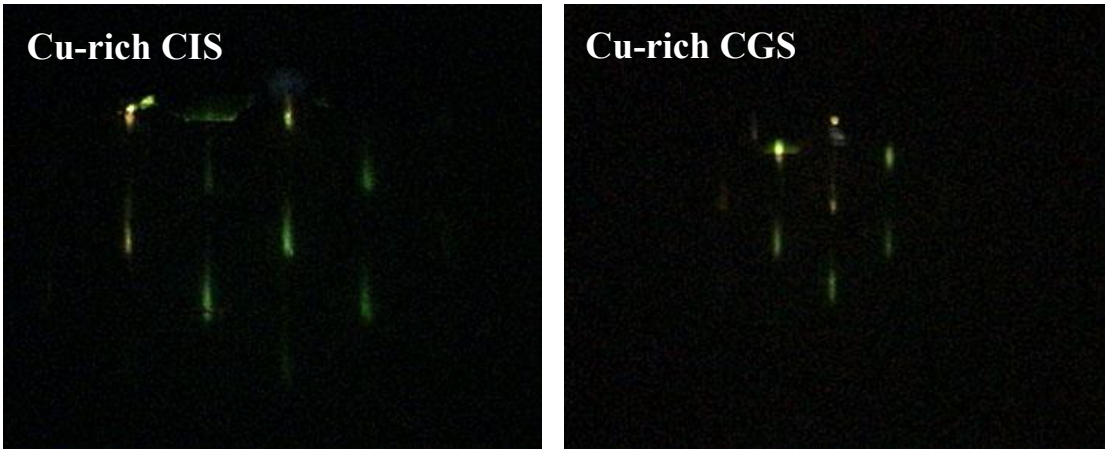

Figure 5.2: RHEED patterns of the Cu-rich CIS and CGS epitaxial films.

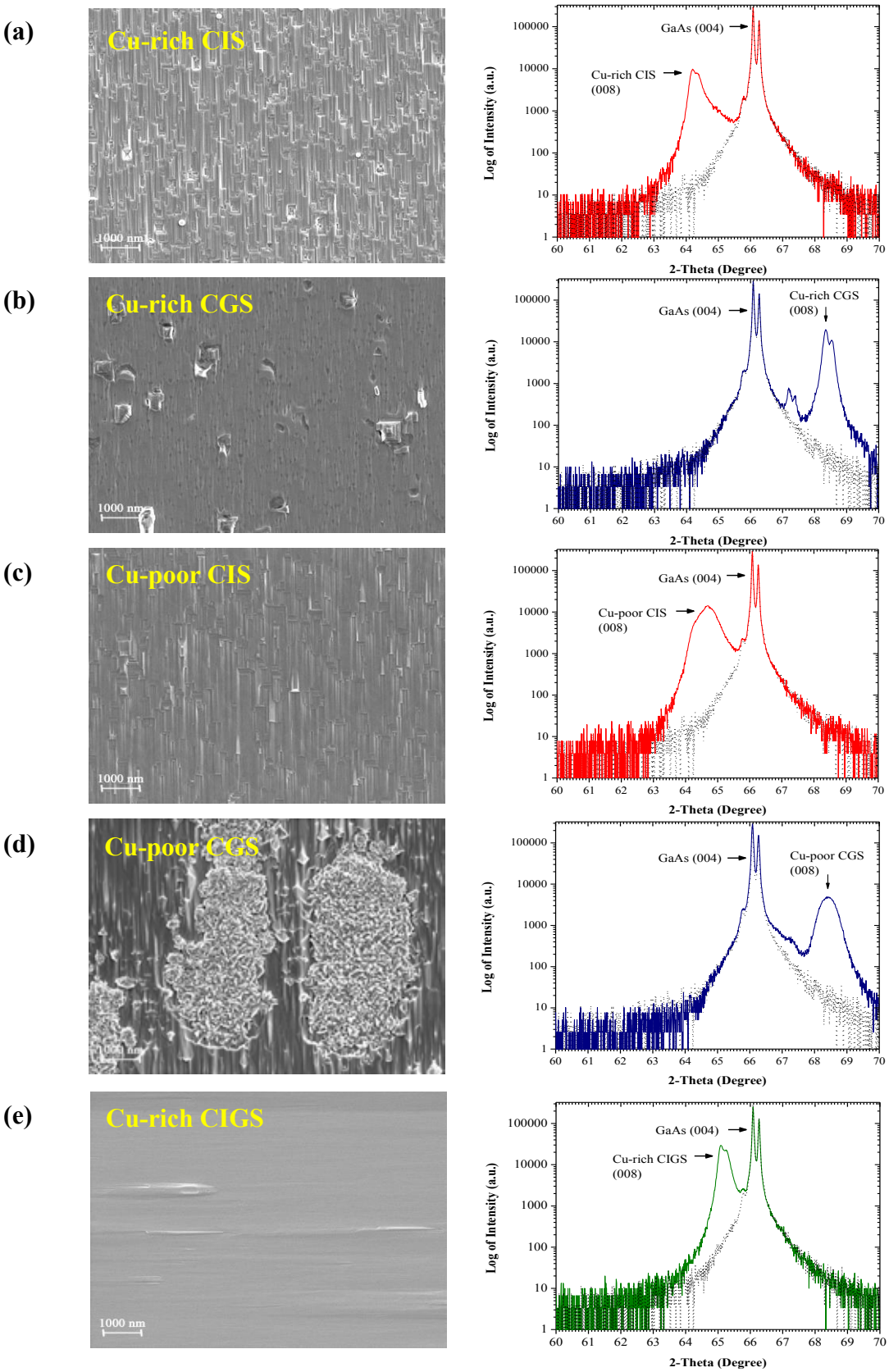

Figure 5.3: SEM images of surface and XRD patterns of standard epitaxial layer of CIS and CGS on GaAs(001) with varying Cu-atomic composition.

Table 5.1: (008) peak position of Cu-rich and Cu-poor compositions of CIS and CGS epitaxial films on GaAs(001) substrate and its calculated values of c-axis lattice constant.

Standard Single Layers	(008) Peak position (2θ)	c-axis (Å)
CIS (y=1.2)	64.20	11.60
CIS (y=0.85)	64.67	11.52
CGS (y=1.2)	68.35	10.97
CGS (y=0.85)	68.42	10.96
CIGS	65.09	11.46

The morphologies of the CIS and CGS epitaxial films obtained from SEM are obviously different. The Cu-rich and Cu-poor CGS epitaxial films reveal rougher morphology in random regions. Especially in the Cu-poor CGS, large areas of rough surface are scattered all over the smooth region. Yoon *et al.* has studied the effect of Cu-Se phase on the epitaxial growth of CIS on GaAs(100) and discovered the region on the Cu-poor CIS surface similar to this experiment. They explained that the rougher region was the film that grew in the Stranki-Krastanov (S-K) growth mode and Cu-Se phase could adapt this mode by increasing the mobility of adatoms to another mode. However, they also showed that these island regions were a single crystal and had the same orientation as the smooth regions [43]. In this work, the random rougher regions are hardly seen in the CIS epitaxial films, but found in the Cu-poor CGS epitaxial film instead. The XRD patterns displayed in Fig. 5.3 shows the CIS, CGS and CIGS patterns in both Cu-rich and Cu-poor compositions. The highest intensity at 2θ about 66.08° indicates the (004) peak of the GaAs substrate. It can be seen that the broadening of the CIS and CGS peaks are observed in the Cu-poor films. The peak positions including the calculation of a lattice parameter (c-axis) are listed in Table 5.1.

5.2 Epitaxial CIS/CGS and CGS/CIS Bilayers

The epitaxial CIS/CGS and CGS/CIS bilayers were fabricated in order to observe the inter-diffusion of Ga and In under the crystal orientation constraints and to compare with the polycrystalline bilayers. The epitaxial CIS/CGS and CGS/CIS bilayers were fabricated with the total thickness of 1 μm. The layer of CIS was thicker than the layer of CGS in order to obtain the ratio of group-III elements with x ~ 0.4 – 0.5. The process duration of the growth was 60 and 40 minutes for the CIS and the CGS, respectively. The deposition rate for the epitaxial films was lower than that of the polycrystalline films. The substrate temperature was set at 600°C. The CIS and CGS were varied both Cu-rich and Cu-poor compositions. The pyrometer signals for Cu-rich bilayers during the deposition process is shown in Fig. 5.4. The as-grown films were analyzed with SEM for their cross-section, EDS for trace depth profiles and XRD for their phases.

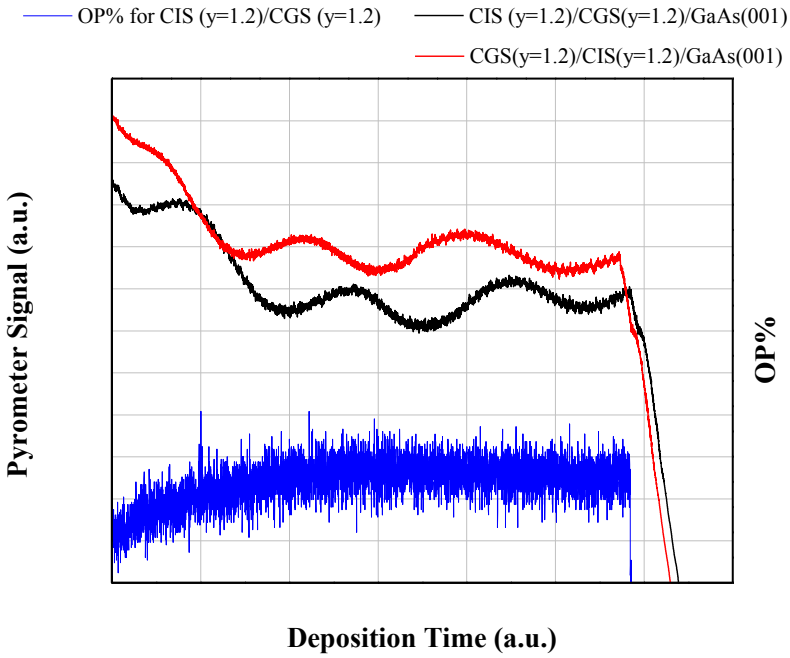

Figure 5.4: The temperature profiles T_{pyro} and substrate heater output power (OP%) of Cu-rich CIS/CGS and CGS/CIS epitaxial bilayers.

The cross-section SEM images are illustrated in Fig. 5.5(a) – (d) and Fig. 5.6(a) – (d) for CIS/CGS and CGS/CIS, respectively. For the CIS/CGS epitaxial bilayers, the Cu-poor CGS as a bottom layer seems to show the grain boundaries like those seen in the polycrystalline bilayers. The island growth in random regions for the Cu-poor CGS films can induce poor crystal growth in the bilayers. On the other hand, the films with the bottom layer being Cu-rich CIS or Cu-rich CGS show the dense and homogeneous epitaxial.

The XRD patterns in Fig. 5.5 and Fig. 5.6 show the crystal structure of CIS/CGS and CGS/CIS epitaxial bilayers on the GaAs(001) substrate, respectively, including the line indicating the peak positions of CIS, CGS and CIGS epitaxial films. The lattice parameters (a-axis) of GaAs, CIS and CGS are 5.651 Å, 5.782 Å and 5.608 Å, respectively [44, 45]. Thus, the lattice mismatch for CIS/CGS, CIS/GaAs and CGS/GaAs films is $\Delta a/a \sim 2.9$ %, ~ 2.2 % and ~ 0.6 %, respectively. As a result, the CIS/GaAs structure has more lattice misfit than the CGS/GaAs structure. When the CIS layer is grown either on the GaAs substrate or the CGS layer, the strain is generated in the CIS near the interface. Then, CIS peak is shifted to the smaller 2θ. In CIS(y=1.2)/CGS(y=1.2), CIS(y=0.85)/CGS(y=1.2), CIS(y=1.2)/CGS(y=0.85) and CGS(y=1.2)/CIS(y=1.2) bilayers, the XRD patterns show the separated peaks of CIS and CGS. It can be observed that the inter-diffusion of Ga and In is less or hardly occurs in a bottom layer with Cu-rich composition despite the CGS peak is shift from the reference line. It can be explained that the appearance of CGS around 2θ of 67°-69° is the combination of the CGS interface layer from the melt-back of the GaAs surface and the deposited CGS film on top. The CGS interface layer occurs by the excess Cu-Se phase mix with Ga atoms from the GaAs substrate. However, the dramatic disappearance of the CGS peak are found in the CIS (y=0.85)/CGS(y=0.85) and CGS(y=1.2)/CIS(y=0.85) bilayers. This situation implies that the thinner CGS intermixes with the thicker CIS forming the CIGS and left with lower intensity of the CIS. The work of Niki *et al.* on the CIS epitaxial films grown by molecular beam epitaxy technique indicated that a common acceptor-type defect such as Cu-vacancies (V_{Cu}) and donor-type defects tended to be heavily compensated in the Cu-poor films [46, 47]. This suggests that it is quite possible that the defects from the Cu-poor film as the carriers can enhance the inter-diffusion of Ga and In.

For the CIS(y=0.85)/CGS(y=0.85) and CIS(y=1.2)/CGS(y=0.85) bilayers, the Ga diffusion is more obvious in the first case despite the Cu-poor CGS as a bottom layer in both cases. It is proposed from the observations that the excess Cu and Se atoms from the Cu-rich CIS enhance the structure of Cu-poor CGS to a better quality. On the other hand, for the CGS(y=1.2)/CIS(y=0.85) bilayer that has the excess Cu and Se atoms from the Cu-rich CGS layer on the top, the peak of CGS can no longer be observed but the shift of CIS peak toward the broadening CIGS peak occurs instead which is opposite to that observed in the CIS(y=1.2)/CGS(y=0.85) bilayer. By considering the lattice constants between the CIS and the CGS, the CIS structure is larger than that of the CGS, then the diffusion of the elements such as Ga into the CIS structure is perhaps easier. Thus the peak of CGS disappears in the CGS(y=1.2)/CIS(y=0.85) condition. For the case of CGS(y=0.85)/CIS(y=1.2), the alloying of CIGS at $x \sim 0.4$ is observed even if the CGS peak still remains. The excess Cu-Se phase from CIS can draw and mix Ga from the GaAs substrate to form the CGS interface layer. At the same time, the Cu-Se phase enhances In out-diffuse from the structure to form the CIGS from the incoming flux of CGS with the fully disappearance of the CIS pattern. The EDS trace depth profiles of the epitaxial bilayers grown at 600°C are shown in Fig. 5.7 and Fig. 5.8. For the relative poorer Ga and In inter-diffusion in CIS(y=1.2)/CGS(y=1.2), CGS(y=1.2)/CIS(y=1.2), CIS(y=0.85)/CGS(y=1.2) and CIS(y=1.2)/CGS(y=0.85) bilayers, EDS calculation of x value show the trend of separated CIS and CGS layers. The distribution of In atoms in CIS/CGS bilayers decreases from the surface to the bottom as seen in Fig. 5.7. On the other hand, for the Cu-rich CGS/CIS bilayers, Ga atoms concentrate near the surface than other CGS/CIS bilayers as seen in Fig. 5.8(a) – (d). It is noted here that it was difficult to avoid the signals of Ga from the GaAs substrate due to the interaction volume of electron beams. Thus, for both epitaxial CIS/CGS and CGS/CIS bilayers, the large amount of Ga atoms were observed in the bottom layer. However, the XRD data show higher diffusion of Ga and In atoms in CIS(y=0.85)/CGS(y=0.85), CGS(y=0.85)/CIS(y=0.85), CGS(y=1.2)/CIS(y=0.85) and CGS(y=0.85)/CIS(y=1.2) conditions.

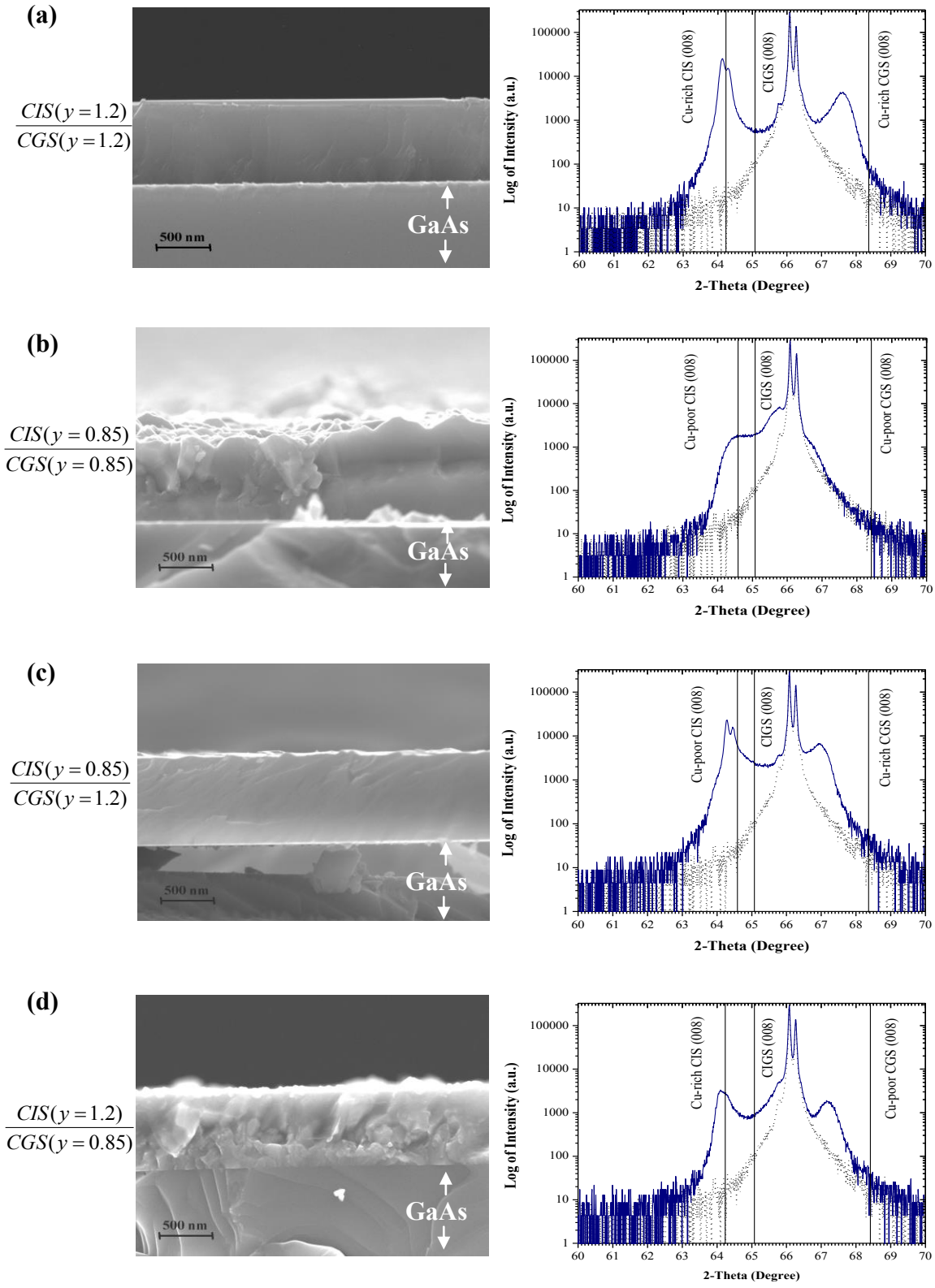

Figure 5.5: SEM cross-section images and XRD patterns of CIS/CGS bilayers on GaAs(001).

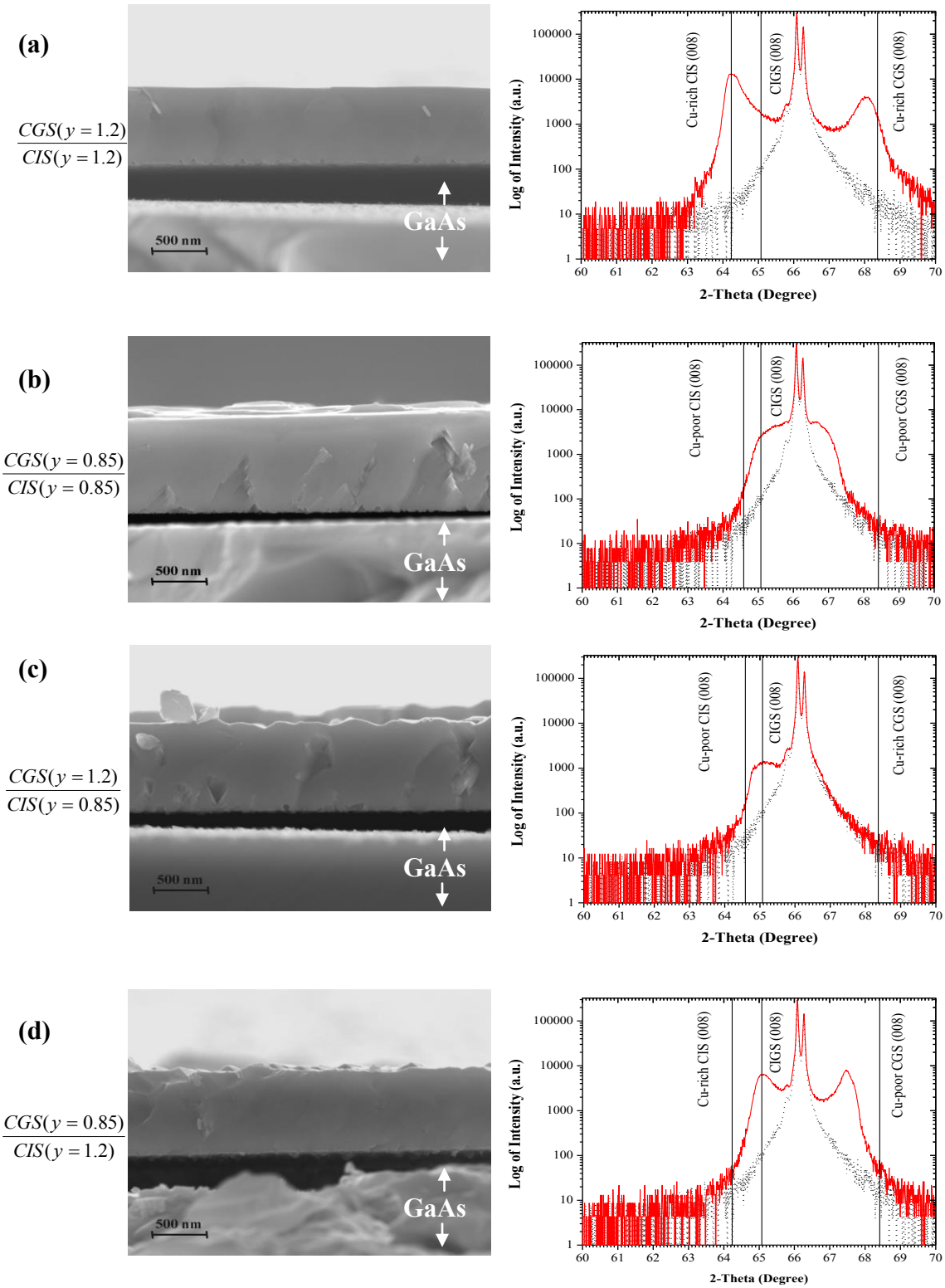

Figure 5.6: SEM cross-section images and XRD patterns of CGS/CIS bilayers on GaAs(001).

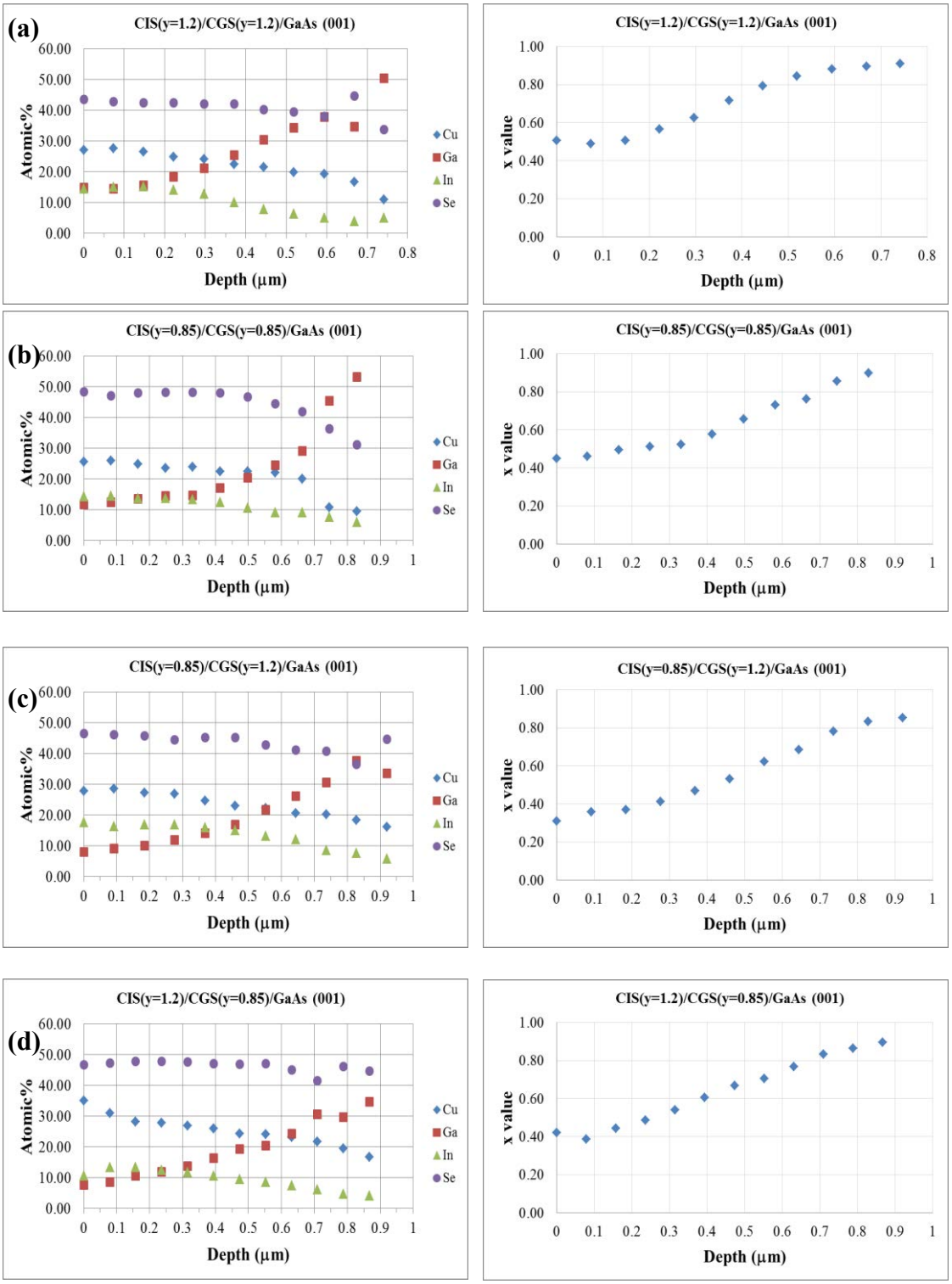

Figure 5.7: EDS trace depth profiles and x values ([Ga]/([Ga]+[In])) for CIS/CGS bilayers on GaAs(001).

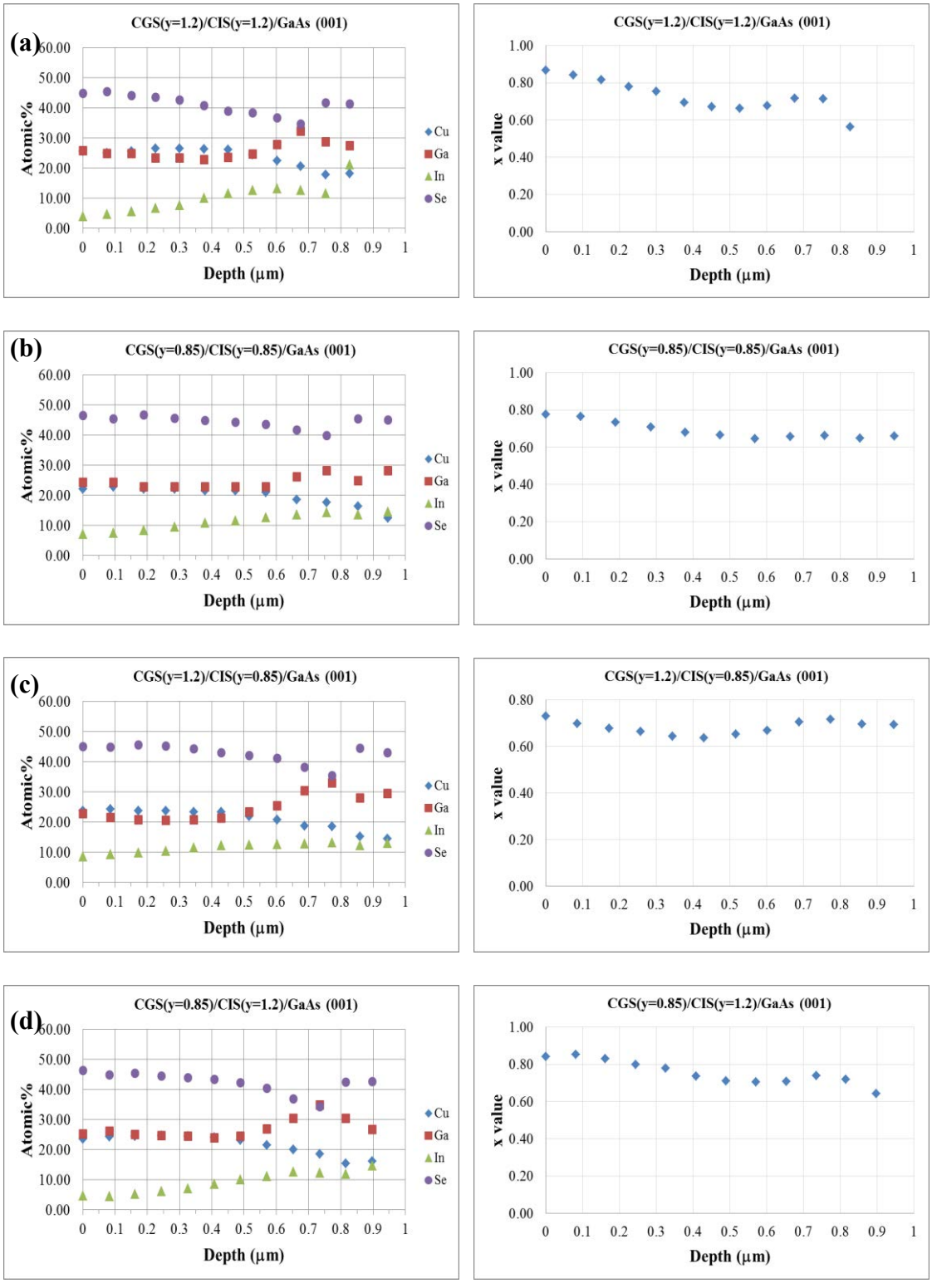

Figure 5.8: EDS trace depth profiles and x values ([Ga]/([Ga]+[In])) for CGS/CIS bilayers on GaAs(001).

5.3 Comparison of Ga and In Diffusion in Polycrystalline and Epitaxial Bilayers

It was previously known experimentally in Ch. IV that the diffusion of Ga and In in the bilayers grown on SLG substrates were better observed in Cu-rich CIS/Cu-rich CGS, Cu-poor CIS/Cu-poor CGS and also Cu-poor CGS/Cu-poor CIS bilayers. In contrast, for the CIS/CGS bilayers grown on Al_2O_3/SLG, the inter-diffusion was observed in all conditions. From these results, for the Cu-rich CIS/Cu-rich CGS bilayers, the diffusion of Ga and In is enhanced by the presence of Cu-Se phase and group-III vacancy defects while the diffusion of Ga and In is enhanced by the Cu vacancies in the Cu-poor CIS/CGS and Cu-poor CGS/CIS bilayers.

For the epitaxial bilayers, the inter-diffusion of Ga and In is less or hardly occurs in the Cu-rich CIS/CGS and the Cu-rich CGS/CIS bilayers seen by the separation of CIS and CGS diffraction peaks. The diffusion is strongly observed in the Cu-poor CIS/Cu-poor CGS, Cu-poor CGS/Cu-poor CIS, Cu-rich CGS/Cu-poor CIS and Cu-poor-CGS/Cu-rich CIS epitaxial bilayers. The diffusion of Ga is implied by the disappearance of the CGS diffraction peak and the appearance alloying CIGS. The result is opposite to that in the bilayers grown on SLG, where the best diffusion is observed in Cu-rich CIS/CGS grown on Na blocking (Al_2O_3/SLG). By direct observation of $Cu_{2-x}Se$ phase in the Cu-rich CIS grown on GaAs(001), Niki *et al.* found that the excess $Cu_{2-x}Se$ was present along the grain boundaries and surface of the CIS films. The $Cu_{2-x}Se$ has an important role for strain relief in the layer by surface undulation [14, 15]. It is possible that the role of $Cu_{2-x}Se$ phase on epitaxial layer is only for the strain relaxation and enhancing the crystal structure quality, and has less effect in the inter-diffusion of Ga and In in epitaxial bilayers. For the Cu-rich bottom layer, the diffusion seems to be relatively difficult in Cu-rich CIS/Cu-rich CGS, Cu-rich CGS/Cu-rich CIS epitaxial bilayers. Generally, Cu-rich film exhibit high crystalline quality where the vacancy defects that enhance the diffusion of Ga and In is barely observed [46, 47]. However, the inter-diffusion of Ga and In for forming CIGS can be observed in Cu-poor CGS/Cu-rich CIS condition. The excess Cu-Se phase on bottom layer still enhance Ga and In inter-diffusion that is different from the CGS/CIS bilayers with and without Na. The point of agreement between

polycrystalline and epitaxial bilayers for the inter-diffusion is the defects that contain in the Cu-poor bilayers. As mentioned above, the diffusion of the elements will take place through vacant lattice sites if the layer has the crystal imperfection, e.g. Cu vacancies for this work.

5.4 Summary

The epitaxial CIS/CGS bilayers and vice versa were fabricated on GaAs(001) substrates with varying Cu-atomic ratio, e.g. Cu-rich and Cu-poor compositions in each layer. The substrate temperature was kept at 600°C. The higher Ga and In inter-diffusion was observed in Cu-poor CIS/Cu-poor CGS, Cu-poor CGS/Cu-poor CIS, Cu-rich CGS/Cu-poor CIS and Cu-poor CGS/Cu-rich CIS epitaxial bilayers by the disappearance of CGS (008) XRD peak and also the appearance alloying CIGS peak pattern. The diffusion happened by the enhancing Cu vacancy defects induced in a Cu-poor bottom layer. The diffusion in the epitaxial bilayers does not involve the existence of Cu-Se secondary phase for the Cu-rich bilayers. The results correspond to the Cu-poor CIS/Cu-poor CGS and Cu-poor CGS/Cu-poor CIS bilayers grown on the SLG and Al_2O_3/SLG substrates such that Ga and In diffuse via the vacancy defects. Without these defects, the diffusion cannot take place. Moreover, the diffusion of the elements is also related to the size of unit cell of the bottom layer, where the size of the CGS is smaller than that of the CIS. Thus, it results in the poor inter-diffusion of Ga and In in Cu-rich CIS/Cu-poor CGS condition.

Chapter VI

Conclusions and Outlooks

One of the techniques to enhance the performance and simultaneously reduce the materials used in the CIGS thin film solar cells is the Ga-grading technique. The inter-diffusion mechanisms of Ga and In in the CIGS film are the key factor one has to understand its nature.

In this research, the fabrication of the CIS/CGS and also CGS/CIS bilayers with varied Cu-atomic ratio (y = [Cu]/([Ga]+[In])) was proposed to understand the diffusion mechanisms of In and Ga. The bilayers were fabricated by the molecular beam epitaxy system in order to minimize the contaminations during the growth process. The as-grown films were mainly characterized by the XRD technique in order to determine the inter-diffusion of Ga and In by observing the shift of diffraction peaks from the referenced positions of the CIS and the CGS films. The bilayers were grown on different types of substrate such as soda-lime glass (SLG), soda-lime glass coated with Al_2O_3 to prohibit the diffusion of Na into the bilayers and GaAs(001) wafer. Generally, the SLG is used because it can supply Na to the absorber layer during the growth process through the layer of Mo back-contact. The advantage of Na incorporation is the achievement of high-efficiency CIGS solar cells. Na can reduce the stability of ordered defect compounds (ODC) or $2V_{Cu}^{-} + In_{Cu}^{2+}$ by replacing itself in the Cu sites, and then it enhances the Cu vacancies that results in the increasing of diode current in the cells [21].

The important results of finding in this work is that the diffusion of Ga and In is mainly due to the vacancies available at high substrate temperature. In the Cu-rich CIS/CGS bilayer with the presence of Na, the inter-diffusion of Ga and In is reduced or hindered by group-III vacancies (V_{Ga} and V_{In}) when compared with the bilayers without Na. However, the diffusion can occur because of the existing Cu-Se that was shown on the work by adding the Cu-Se layer in the samples which has lower Ga and In inter-diffusion. The Cu-Se phase plays the important role on the mobility of group-III element.

In the Cu-poor CIS/CGS bilayer with and without Na, the diffusion is due to the Cu vacancies that enhanced Ga and In inter-diffusion. In this case, the lower quality of grain growth observed from the SEM images is consistent with lower intensity from the XRD results. This suggests that Na has the influence to grain growth as well as the diffusion of elements.

For the alternated order of deposition, e.g. the CGS/CIS bilayers with and without the presence of Na, the diffusion is not significantly different for the bilayers that has Cu-rich as a bottom layer, Cu-rich CGS/Cu-rich CIS and Cu-poor CGS/Cu-rich CIS. The stability of the Cu-rich CIS is hardly affected by Na resulting in a poor diffusion. This is also observed in the Cu-rich CGS/Cu-poor CIS bilayer where the excess Cu-Se phase from the CGS layer enhances the stability and the quality of the Cu-poor CIS layer. However, the diffusion in the Cu-poor CGS/Cu-poor CIS bilayer with and without Na are similar. This indicates that the inter-diffusion of Ga and In is enhanced by Cu vacancies inside the Cu-poor structure.

Apart from the SLG substrates, the epitaxial CIS/CGS and CGS/CIS bilayers were fabricated to compare the inter-diffusion of Ga and In with the polycrystalline counterparts. The epitaxial CIS/CGS and CGS/CIS bilayers with the Cu-rich composition show the separated peaks of CIS and CGS that are opposite to the polycrystalline Cu-rich CIS/CGS bilayer. However, the results of Cu-rich epitaxial bilayers are similar to the polycrystalline Cu-rich CGS/CIS bilayer. It can be pointed out that with the stability of the crystal structure and less defects, the inter-diffusion of the elements is difficult to occur. In parallel, the lower diffusion was also found in epitaxial bilayers that has Cu-rich as a bottom layer, e.g. CIS(y=0.85)/CGS(y=1.2). The Cu-Se phase does not contribute to the element inter-diffusion in epitaxial bilayers as much as in the polycrystalline bilayers. However, for the CGS(y=0.85)/CIS(y=1.2) epitaxial bilayer, Cu-Se phase still enhances the inter-diffusion of Ga and In by observing the alloying CIGS at $x \sim 0.4$. For the Cu-poor epitaxial CIS/CGS and CGS/CIS bilayers, the inter-diffusion significantly occurred by observing the disappearance of the CGS peak. The result can be related to the diffusion in the Cu-poor polycrystalline CIS/CGS and CGS/CIS bilayers where the main mechanism that enhances the inter-diffusion is the vacancy defects. In the Cu-poor epitaxial bilayer, it maintains an acceptor type defects such as Cu vacancies, then

the diffusion can take place in this way. However, the inter-diffusion of Ga and In is difficult for the epitaxial CIS(y=1.2)/CGS(y=0.85) bilayer even if the bottom layer is the Cu-poor CGS. This can be expressed in two points of view. (i) the excess Cu-Se phase stabilizes the CGS crystal structure by reducing the defect and strain between the layer growing on the substrate, and (ii) by comparing with the epitaxial CGS(y=1.2)/CIS(y=0.85) bilayer, the Cu-poor CIS as the bottom layer has higher Ga and In inter-diffusion than the bilayer that has the Cu-poor CGS as the bottom layer that is possible due to the smaller unit cell size of the CGS than that of the CIS. In atoms from the upper layer are difficult to diffuse into the CGS structure. Then, the separation of CIS and CGS peaks is observed.

Although, the true mechanism for the Cu-Se phase on the element diffusion and also a remedy of a poor crystal structure by Cu-Se phase are still unclear to date but its effect is the advantage key factor for studying the physics inside the CIGS structure in order to improve the performance of the CIGS solar cells.

The recommendations to obtain better results to understand the mechanisms of element diffusion in the CIS/CGS and the CGS/CIS bilayers are; (i) the bilayer should be characterized by secondary ion mass spectrometer (SIMS) for substantiating the distribution of the elements in depth profiles, (ii) the explanations given here are the implications from the observations of the experiment, thus better or suitable techniques or equipment to detect defects or vacancies may be required to guarantee that diffusion of elements agrees with theoretical calculation.

References

[1] Corfee-Morlot, J., and Höhne, N. Climate change: long-term targets and short-term commitments. Global Environ. Change 13 (2003): 277-293.

[2] NREL. World Record of Solar Cell Efficiency. A National laboratory of the U.S. Department of Energy Office of Energy Efficiency & Renewable Energy, 2012.

[3] Philip, J., Dimitrios, H., Erwin, L., Stefan, P., Roland, W., Richard, M., Wiltraud, W., and Michael, P. New world record efficiency for Cu(In,Ga)Se_2 thin-film solar cells beyond 20%. Prog. Photovoltaics 19 (2011): 894-897.

[4] Tokio Nakada. Invited Paper: CIGS-based Thin Film Solar Cells and Modules: Unique Material Properties. Elec. Mater. Lett. 8(2) (2012): 179-185.

[5] Schön, J. H., and Bucher, E. Comparison of point defects in $CuInSe_2$ and $CuGaSe_2$ single crystals. Sol. Energy Mater. Sol. Cells 57 (1999): 229-237.

[6] Dullweber, T., Hanna, G., Shams-Kolahi, W., Schwartzlander, A., Contreras, M. A., Noufi, R., and Schock, H. W. Study of the effect of gallium grading grading in Cu(In,Ga)Se_2. Thin Solid Films 361-362 (2000): 478-481.

[7] Rachsak Sakdanuphab. Influence of Sodium in Fabrication Process of High Efficiency Cu(In,Ga)Se_2 Thin Film Solar Cells. Doctoral dissertation, Department of Physics Faculty of Science Chulalongkorn University, 2010.

[8] Subba Ramaiah Kodigala. Thin Films and Nanostructures Cu(In_{1-x},Ga_x)Se_2 Based Thin Film Solar Cells. United States of America: Academic Press of Elsevier, 2010.

[9] Repins, I., Contreras, M., Romero, M., Yan, Y., Metzger W., Li, J., Johnston, S., Egaas, B., DeHart, C., and Scharf, J. Characterization of 19.9%-efficient CIGS absorbers. 33rd IEEE Photovoltaic Specialists Conference (2008).

[10] Schön, J. H., Kloc, Ch., and Bucher, E. Effect of the Ga content on the defect properties of $CuIn_{1-x}Ga_xSe_2$ single crystal. Thin Solid Films 361-362 (2000): 411-414.

[11] Lundberg, O., Bodegard M., Malmstrom J., and Stolt, L. Influence of the Cu(In,Ga)Se_2 Thickness and Ga Grading on Solar Cell Performance. Prog. Photovolt : Res. Appl. 11 (2003): 77-88.

[12] Lundberg, O., Edoff, M., Stolt, L. The effect of Ga-grading in CIGS thin film solar cells. Thin Solid Films. 480-481 (2005): 520-525.

[13] Walter, T., and Schock, H. W. Crystal growth and diffusion in Cu(In,Ga)Se_2 chalcopyrite thin films. Thin Solid Films. 224 (1993): 74-81.

[14] Fons, P., Niki, S., Yamada, A., and Oyanagi, H. Direct observation of the $Cu_{2-x}Se$ phase of Cu-rich epitaxial $CuInSe_2$ grown on GaAs(001). J. Appl. Phys. 84 (1998): 6925-6928.

[15] Niki, S., Fons, P. J., Yamada, A., Lacroix, Y., Shibata, H., and Oyanagi, H. Effects of the surface $Cu_{2-x}Se$ phase on the growth and properties of $CuInSe_2$ films. Appl. Phys. Lett. 74 (1999): 1630-1632.

[16] Fon, P. J., Niki, S., Yamada, A., Okada, Y., Tweet, D. J. Strain-Induced Diffusion in Heteroepitaxially Grown $CuInSe_2$ on GaAs Substrates. Bull. Electrochem. Lab. 60 (1996): 39-42.

[17] Uchino, M., Niki, S., Ai Y., Fons, P. J., Yamada, A., Sakai, N., Yokokawa, H., Oyanagi, H., Chichibu, S.F., Nakanishi, H. Disappearance of the surface Cu-Se second phase during post-growth annealing of $CuInSe_2$ epitaxial films grown under excess Cu-flux conditions. Jpn. J. Appl. Phys. 39 (2000): 205-207.

[18] Schroeder, D. J., Berry, G.D., and Rockett, A. Gallium diffusion and diffusivity in $CuInSe_2$ epitaxial layers. Appl. Phys. Lett. 69 (1996): 4068-4070.

[19] Lundberg, O., Lu, J., Rockett, A., Edoff, M., Stolt, L. Diffusion of indium and gallium in Cu(In,Ga)Se_2 thin film solar cells. J. Phys. Chem. Solids 64 (2003): 1499-1504.

[20] Bodegård, M., Lundberg, O., Lu, J., Stolt, L. Re-crystallisation and interdiffusion in CGS/CIS bilayers. Thin Solid Films 431-432 (2003): 46-52.

[21] Wei, S.H., Zhang, S. B., and Zunger, A. Effects of Na on the electrical and structural properties of $CuInSe_2$. J. Appl. Phys. 85 (1999): 7214-7218.

[22] Bancha Arthibenyakul. Growth and Characterization of High Quality $CuInSe_2$ Epitaxial Thin Films on GaAs Substrates. Doctoral dissertation, Department of Physics Faculty of Science Chulalongkorn University, 2010.

[23] William F. Smith, and Javad Hashemi. Foundation of Material Science and Engineering (SI unit). 5thEdition. Singapore: McGraw-Hill Interprise Inc., 2012.

[24] Milton Ohring. The Materials Science of Thin Films. United States of America: Academic Press, 1992.

[25] Charles Kittel. Introdution to Solid State Physics. 8thEdition. New York: Wiley, 1986.

[26] Yoshino, K., Yokoyama, H., Maeda, K., and Ikari, T. Crystal growth and photoluminescence of $CuIn_xGa_{1-x}Se_2$ alloys. J. Cryst. Growth 211 (2000): 476-479.

[27] Billy J. Stanbery. Copper Indium Selenides and Related Materials for Photovoltaic Devices. Crit. Rev. Solid State Mater. Sci. 27 (2002): 73-117.

[28] Rincón, C., Bellabarba, C., González, J., and Sánchez Pérez, G. Optical Properties and Characterization of $CuInSe_2$. Sol. Cells 16 (1986): 335-349.

[29] Noufi, R., Yan, Y., Jones, K., Al-Jassim, M., Keyes, B., Alleman, J., and Ramanathan K. Investigation of the Microstructure of $Cu(In,Ga)Se_2$Thin Films Used in High-Efficiency Devices. 29th IEEE Photovoltaic Specialists Conference (2002).

[30] Bernardioni, G. P., and Catani, A. The Cu-Se System. Mineral. Deposita (Berl.) 3 (1968): 375-380.

[31] Chityuttakan, C., Chinvetkitvanich, P., Yoodee, K., Chatraphorn, S., In situ monitoring of the growth of $Cu(In,Ga)Se_2$ thin films. Sol. Energy Mater. Sol. Cells 90 (2006): 3124-3129.

[32] Berycka, I., Zubel, I. Chemical etching of (100) GaAs in a sulphuric acid-hydrogen peroxide-water system. J. Mater. Sci. 4 (1987): 1299-1304.

[33] Dieter K. Schroder. Semiconductor Material and Device Characterization. 3rdEdition. United States of America: John Wiley & Sons, Inc., 2006.

[34] Yang, Y. R., Wanek, J., Shahidi, M. Representing the retinal line spread shape with mathematical functions. J. Zhejiang Univ. Sci. B 9 (2008): 996-1002.

[35] Tuttle, J. R., Albin, D. S., and Noufi, R. Characterization of Thin Film $CuInSe_2$ and $CuGaSe_2$: The Existence and Identification of Secondary Phases. Solar Cells 27 (1989): 231-236.

[36] Walker, B., and Agrawal, R. Grain Growth Enhancement of Selenide CIGSe Nanoparticals to Densified Using Copper Selenides. IEEE (2011): 2654-2657

[37] Hunger, R., Sakurai K., Yamada, A., Fons, P., Iwata, K., Matsubara, K., and Niki, S. In situ deposition rate monitoring during the three-stage-growth process of $Cu(In,Ga)Se_2$ absorber films. Thin Solid Films 431-432 (2003): 16-21.

[38] Panita Chinvetkitvanich. Molecular Beam Deposition and Characterization of Wide-Band-Gap $Cu(In,Ga)Se_2$ for Thin Film Solar Cells. Doctoral dissertation, Department of Physics Faculty of Science Chulalongkorn University, 2006.

[39] Marudachalam, M., Hichri, H., Birkmire, R. W., and Schultz, J. M. Diffusion of In and Ga in Selenized Cu-In and Cu-Ga Precursors. 25thPVSC (1996): 805-807.

[40] Braunger, D., Hariskos, D., Bilger, G., Rau, U., and Schock, H. W. Influence of sodium on the growth of polycrystalline $Cu(In,Ga)Se_2$ thin films. Thin Solid Films 361-362 (2000): 161-166.

[41] Matson, R. J., Granata, J. E., Asher, S. E., and Young, M. R. Effect of substrate and Na concentration on device properties, junction formation, and film microstructure in $CuInSe_2$ PV device. National Center for Photovoltaics Program Review Meeting, September 8-11 (1998).

[42] Granath, K., et al. The effect of NaF on Cu(In,Ga)Se2 thin film solar cells. Sol. Energy Mater. Sol. Cells 60 (2000): 279-293.

[43] Yoon, S., Kim, S., Craciun, V., Kim, W. K., Kaczynki, R., Acher, R., Anderson, T. J., Crisalle, O. D., and Li, S. S. Effect of a Cu-Se secondary phase on the epitaxial growth of $CuInSe_2$ on (100) GaAs. J. Crys. Growth 281 (2005): 209-219.

[44] Joint Committee on Powder Diffraction Standards (JCPDS), 40-1487.

[45] Joint Committee on Powder Diffraction Standards (JCPDS), 75-104.

[46] Niki, S., Yamada, A., Hunger, R., Fons, P. J., Iwata, K., Matsubara, K., Nishio, A., and Nakanishi, H. Molecular beam epitaxial growth and characterization of $CuInSe_2$ and $CuGaSe_2$ for device application. J. Crys. Growth 237-239 (2002): 1993-1999.

[47] Niki, S., Makita, Y., Yamada, A., Hellman, O., Fons, P. J., Obara, A., Okada, Y., Shioda, R., Oyanagi, H., Kurafuji, T., Chichibu, S., and Nakanishi, H. Heteroepitaxy and characterization of $CuInSe_2$ on GaAs (001). J. Crys. Growth 150 (1995): 1201-1205.

[48] Kessler, F., and Rudmann, D. Technological aspects of flexible CIGS solar cells and modules. Sol. Energy 77 (2004): 685-695.

APPENDICES

APPENDIX A

List of Symbols and Abbreviations

Symbols

a	Lattice parameter
a.u.	Arbitrary unit
b	Burger vector
c	Lattice parameter
Cu_i	Copper interstitial
Cu_{In}	Copper substitution to Indium site
Cu_{Se}	Copper substitution to Selenium site
D	Diffusivity (m^2/s)
d_{hkl}	Inter planar spacing of the crystal plane
E	Average energy
E^*	Activation energy or formation energy
eV	Energy unit: electron volt
E_v	Activation energy to form vacancy
G	Crystallite size
Ga_{Cu}	Gallium substitution to Copper site
In_{Cu}	Indium substitution to Copper site
In_i	Indium interstitial
In_{Se}	Indium substitution to Selenium site
J_{sc}	Short circuit current
k	Boltzmann's constant: 1.38×10^{-23} $m^2 \cdot kg/s^2$
K	Temperature unit: Kelvin
kV	Energy unit: kilovolt
M	Molecular mass
N_A	Avogrado's number
Na_{Cu}	Sodium substitution to Copper site
nm	length unit: nanometer (10^{-9} m)

N_{total}	Total number of atoms
n_v	Number of vacancies
Se_{Cu}	Selenium substitution to Copper site
Se_i	Selenium interstitial
Se_{In}	Selenium substitution to Indium site
T_m	Melting point temperature
Torr	Pressure unit
T_{Sub}	Substrate temperature
V_{Cu}	Copper vacancy
V_{Ga}	Gallium vacancy
V_{In}	Indium vacancy
V_{oc}	Open circuit voltage
V_{Se}	Selenium vacancy
W	Power unit: Watt
y	Copper atomic composition ([Cu]/([Ga]+[In]))
$y > 1$	Cu-rich composition
$y < 1$	Cu-poor composition
$y = 1$	Stoichiometric composition
Z	Atomic number
Å	Angstrom (10^{-10} m)
ρ	Density
α	Molar density: $\rho * M^{-1}$
λ	Wavelength
θ	Bragg angle
°C	Temperature unit: degree Celsius
Δm	Molecularity deviation
μm	Micron (10^{-6} m)
ΔS	Stoichiometry deviation

Abbreviations

Al_2O_3	Aluminum Oxide
AM	Air Mass
AMU	Atomic Mass Unit
at.%	Atomic percentage
CGS	Copper Gallium Diselenide: $CuGaSe_2$
CIGS	Copper Indium Gallium Diselenide: $Cu(In_{1-x}Ga_x)Se2$
CIS	Copper Indium Diselenide
Cu	Cu element
DI	De-ionized
EDS	Energy Dispersive X-ray Spectroscopy
FWHM	Full Width at Half Maximum
FV	Frank-Van der Merwe growth
Ga	Ga element
GaAs	Gallium Arsenide
H_2O	Water
H_2O_2	Hydrogen Peroxide
H_2SO_4	Sulfuric Acid
In	Indium element
MBD	Molecular Beam Deposition
Mo	Molybdenum
Na	Sodium
OP%	Output power
PBN	Pyrolytic Boron Nitride
PID	Proportion-integral-deviation
QCM	Quartz Crystal Thickness monitor
QMS	Quadrupole Mass Spectroscopy
Re	Rhenium
RGA	Residual Gas Analysis
RHEED	Reflection High Energy Electron Diffraction
Se	Se element
SEM	Scanning Electron Microscopy

SK	Stranki-Krastanov growth
SLG	Soda-lime glass
Ta	Tantalum
UHV	Ultra-High Vacuum
VW	Volmer-Weber growth
W	Tunsten
wt.%	Weight percentage
XRD	X-Ray Diffraction
$(CH_3)_2CO$	Acetone
CH_3OH	Methanol
C_2HCl_3	Trichloroethylene (TCE)

APPENDIX B

1. Soda lime glass composition

Composition	Typical container Glass (%)
SiO_2	74.42
Al_2O_3	0.75
MgO	0.30
CaO	11.27
Li_2O	0.00
Na_2O	12.90
K_2O	0.19
Fe_2O_3	0.01
TiO_2	0.01
SO_3	0.16

2. Thermal expansion coefficients of substrate materials*

Material	CTE (10^{-6} K^{-1})	$T_{Sub\ (max)}$ (°C)	Notes
SLG	9 (20-300°C)	≈ 600	Standard glass substrate
Corning 7059	4.6	> 600	Alkali-free glass
Mo	4.8-5.9 (20-600°C)	> 600	Adhesive layer
Al_2O_3	6-8	> 600	Insulating layer and/or blocking Na
$CuInSe_2$	11.2-11.4		c-axis
$CuGaSe_2$	13.1		c-axis

**Ref. [48]*

Biography

Boonyaluk Namnuan was born on September 8th, 1988 in Bangkok, Thailand. She received the Bachelor degree of Science (First Class Honors) in Physics from Thammasat University, Thailand in 2010. In parallel, she received the scholarship for studying in Master's degree of science program until the Philosophy's degree from Science Achievement Scholarship of Thailand.

Conference Presentation:

2012 7th Annual Conference of the Thai Physics Society (Siam Physics Congress SPC 2012), May 9-12, 2012, Phra Nakhon Si Ayutthaya, Thailand.

8th Mathematics and Physical Science Graduate Congress (MPSCG 2012), December 8-10, 2012, Faculty of Science, Chulalongkorn University, Thailand.

2013 8th Annual Conference of the Thai Physics Society (Siam Physics Congress SPC 2013), March 21-23, 2013, Chiang Mai, Thailand.